

Band gap engineering: *the role of anions*

vorgelegt von
Diplom Chemiker
Björn Anke
geb. in Neubrandenburg

von der Fakultät II - Mathematik und Naturwissenschaften
der Technischen Universität Berlin
zur Erlangung des akademischen Grades

Doktor der Naturwissenschaften
- Dr. rer. nat. -

genehmigte Dissertation

Promotionsausschuss:

Vorsitzender: Prof. Dr. Peter Strasser
1. Gutachter: Prof. Dr. Martin Lerch
2. Gutachter: Prof. Dr. Malte Behrens

Tag der wissenschaftlichen Aussprache: 05. Mai 2017

Berlin 2017

Abstract

The degradation of harmful organic pollutants with the help of semiconductors is regarded as one of the crucial solutions for waste water treatment. The main disadvantage of extensively used photocatalysts such as SnO₂, ZnO, and TiO₂ is their activity under UV illumination due to their wide band gap (~ 3.2 eV). Therefore they can only absorb 5 – 7 % of the solar spectrum. In order to overcome this barrier, processes for the selective influencing the optical band gap were developed: '*band gap engineering*'.

This dissertation is an exhaustive attempt for synthesis and characterization of new anion-doped semiconductors using hydrogen fluoride and ammonia as doping suppliers. The amorphous oxygen precursors were synthesized using a modified polymerisable complex method (Pechini route) and a standard wet-chemical precipitation. The experimental parameters were optimized and tuned for all materials to obtain pure phases. Additionally a new and clean synthesis variant for fluorine incorporation was developed. All products of this dissertation have been described using different characterization methods to clarify the structural (Rietveld refinement), chemical (nitrogen/oxygen content), and physical properties (spectral absorption range, density determination). Cooperation partners also carried out quantum chemical calculations (Prof. Dr. Bredow of the Universität Bonn) and measured photoelectrochemical efficiency (Prof. Dr. Michael Wark of the Carl von Ossietzky Universität Oldenburg and Prof. Dr. Anna Fischer of the Albert-Ludwigs-Universität Freiburg).

This thesis is divided into two parts: the tetragonal tungsten bronzes of the Ba_{3-x}La_xTa₅O_{14-x}N_{1+x} type and O/F substitution in monoclinic scheelite-type bismuth vanadate.

Light yellow Ba₃Ta₅O₁₄N and yellow LaBa₂Ta₅O₁₃N₂ were successfully synthesized as phase-pure materials crystallizing isostructurally to the well-known mixed-valence Ba₃Ta^V₄Ta^{IV}O₁₅. The electronic structure of both materials, Ba₃Ta₅O₁₄N and LaBa₂Ta₅O₁₃N₂, were studied theoretically with the range-separated hybrid method HSE06. The most stable structure was obtained when lanthanum was placed on 2*a* and nitrogen on 4*h* sites confirming Pauling's second rule. By incorporating nitrogen, the

measured optical band gap decreases from ~ 3.8 eV for the pure oxide via 2.74 eV for $\text{Ba}_3\text{Ta}_5\text{O}_{14}\text{N}$ to 2.63 eV for $\text{LaBa}_2\text{Ta}_5\text{O}_{13}\text{N}_2$, giving rise to an absorption band well in the visible-light region. Calculated fundamental band gaps confirm the experimental trend. The atom-projected density of states has large contributions from N2p orbitals close to the valence band edge. These are responsible for the observed band gap reduction. Photocatalytic hydrogen formation was investigated, revealing significantly higher activity for $\text{LaBa}_2\text{Ta}_5\text{O}_{13}\text{N}_2$ compared to $\text{Ba}_3\text{Ta}_5\text{O}_{14}\text{N}$ under UV-light.

Fluorine-containing bismuth vanadate powder was synthesized using a new, clean, and simple solid-vapor reaction. Incorporation of fluorine mainly leads to the formation of cation vacancies. Electrodes were fabricated from the pre-synthesized powder samples by electrophoretic deposition onto fluorine-doped tin oxide coated glass slides and subsequent calcination. The photoelectrochemical performance concerning the water oxidation reaction was investigated and compared to pristine BiVO_4 , revealing strongly enhanced photoelectrochemical behavior for the fluorine-containing bismuth vanadate.

Zusammenfassung

Der Abbau von schädlichen organischen Schadstoffen mit Hilfe von Halbleitern gilt als eine der entscheidenden Lösungen für die Abwasserbehandlung. Der Hauptnachteil weit verbreiteter Photokatalysatoren wie SnO_2 , ZnO und TiO_2 ist, dass sie aufgrund ihrer breiten optischen Bandlücke ($\sim 3,2$ eV) nur unter UV-Licht aktiv sind und daher nur 5 – 7 % des Sonnenspektrums absorbieren können. Um diese Hürde zu überwinden, wurden Methoden entwickelt, um die optische Bandlücke selektiv zu beeinflussen, sogenanntes „*Band Gap Engineering*“.

Diese Dissertation befasst sich mit der Synthese und Charakterisierung neuer Anion-dotierter Halbleiter unter Verwendung von Fluorwasserstoff und Ammoniak als Dotierungslieferanten. Die amorphen Sauerstoff-Präkursoren wurden über eine modifizierte Polymerkomplexmethode (Pechini-Methode) und eine übliche nass-chemische Ausfällung synthetisiert. Die experimentellen Parameter wurden optimiert und auf alle Materialien abgestimmt, um einphasige Produkte zu erhalten. Es wurde außerdem eine neue und saubere Synthesevariante für die Fluorierung entwickelt. Alle Produkte dieser Dissertation wurden mittels verschiedener Charakterisierungsmethoden untersucht, um die strukturellen (Rietveld Verfeinerung), chemischen (Sauerstoff/Stickstoff-Gehalt) und physikalischen (spektrale Absorptionsbereich, Dichtebestimmung) Eigenschaften zu bestimmen. Außerdem wurden von Kooperationspartnern quantenchemische Rechnungen getätigt (Prof. Dr. Thomas Bredow von der Universität Bonn) und auch die photoelektrochemische Effizienz gemessen (Prof. Dr. Michael Wark von der Carl von Ossietzky Universität Oldenburg und Prof. Dr. Anna Fischer von der Albert-Ludwigs-Universität Freiburg).

Diese Arbeit gliedert sich in zwei Teile: Die tetragonalen Wolframbronzen vom Typ $\text{Ba}_{3-x}\text{La}_x\text{Ta}_5\text{O}_{14-x}\text{N}_{1+x}$ und O/F-Substitution in monoklinen Bismutvanadat vom Scheelit-Typ.

Hellgelbes $\text{Ba}_3\text{Ta}_5\text{O}_{14}\text{N}$ und gelbes $\text{LaBa}_2\text{Ta}_5\text{O}_{13}\text{N}_2$ wurden erfolgreich phasenrein synthetisiert, die isostrukturell zu dem literaturbekannten, gemischtvalenten $\text{Ba}_3\text{Ta}^{\text{V}}_4\text{Ta}^{\text{IV}}\text{O}_{15}$ kristallisieren. Die elektronische Struktur beider Materialien, $\text{Ba}_3\text{Ta}_5\text{O}_{14}\text{N}$ und $\text{LaBa}_2\text{Ta}_5\text{O}_{13}\text{N}_2$, wurde mit dem Hybridverfahren HSE06 untersucht.

Die stabilste Struktur wurde erhalten, wenn Lanthan auf $2a$ und Stickstoff auf $4h$ Wyckoffpositionen gesetzt wurden, was gleichzeitig im Einklang mit Paulings zweiter Regel steht. Durch Einlagerung von Stickstoff sinkt die gemessene optische Bandlücke von $\sim 3,8$ eV für das reine Oxid über 2,74 eV für $\text{Ba}_3\text{Ta}_5\text{O}_{14}\text{N}$ auf 2,63 eV für $\text{LaBa}_2\text{Ta}_5\text{O}_{13}\text{N}_2$, was zu einer Absorption im Bereich des sichtbaren Lichts führt. Die berechneten Bandlücken bestätigen den experimentellen Trend. Die atom-projizierte Dichte von Zuständen hat große Beiträge von N2p-Orbitalen nahe der Valenzbandkante, diese sind für die beobachtete Bandlückenverringerng verantwortlich. Außerdem wurde die photokatalytische Wasserstoffbildung untersucht, welche eine deutlich höhere Aktivität für $\text{LaBa}_2\text{Ta}_5\text{O}_{13}\text{N}_2$ im Vergleich zu $\text{Ba}_3\text{Ta}_5\text{O}_{14}\text{N}$ im UV-Bereich zeigt.

Fluorhaltiges Bismutvanadatpulver wurde unter Verwendung einer neuartigen, sauberen und einfachen Festkörper-Gas-Reaktion synthetisiert. Der Einbau von Fluor führte hauptsächlich zur Bildung von Kationenleerstellen. Elektroden wurden aus den vorsynthetisierten Pulverproben durch elektrophoretische Abscheidung auf mit Fluor dotierte zinnoxidbeschichtete Glasplättchen und anschließender Kalzinierung hergestellt. Die photoelektrochemische Aktivität bezüglich der Wasseroxidationsreaktion wurde untersucht und mit der des reinen/unfluorierten Bismutvanadats verglichen. Die fluorhaltige Phase zeigte eine stark verbesserte photoelektrochemische Aktivität.

Acknowledgement

First and foremost I would like to express my heartfelt gratitude to my thesis advisor Prof. Dr. Martin Lerch of the Technische Universität Berlin for the opportunity to work on this interesting topic as well as for his direction and support.

Furthermore, I want to thank Prof. Dr. Malte Behrens of the University Duisburg-Essen for being the second reviewer of this doctoral work and Prof. Dr. Peter Strasser of the Technische Universität Berlin for taking over the chair of the doctoral committee.

Many others have contributed to the successful realization of this scientific work, whom I want to thank very much:

Prof. Dr. Thomas Bredow of the Universität Bonn for the quantum chemical calculations,

Dr. Julia Soldat, M. Sc. Martin Pilarski, and Prof. Dr. Michael Wark of the Carl von Ossietzky Universität Oldenburg for the photocatalytic hydrogen formation measurements,

M. Sc. Maika Stöbe, Astrid Müller-Klauke, and Dipl. Ing. (FH) Ulrich Gernert of the Technische Universität Berlin for performing XRF analyses, ICP-OES investigations, and for access to and support with SEM measurements.

A special thank goes to Dipl. Chem. Martin Rohloff (Group of Prof. Anna Fischer) of the Technische Universität Berlin for the photocatalytic oxygen formation measurements and the numerous meetings with fruitful discussions.

I also thank all the Lerch group members, Anna, Claudia, Dennis, Elisabeth, Eva, Stefan, Steven, Suliman, and Tobi; the Grohmann group, Anika, Jana for all the cakes, beers, and ice-cream.

Moreover, thanks go to my lovely friends, who have always been there for me. Many thanks for the moral and emotional support during this work, for enriching my life, and for all our exciting and unforgettable memories. A special big thank goes to Nadine and Niklas for proofreading the thesis.

All of this could not happen without my family, I am very thankful to my parents for their continuous encouragement, love, and full support in all matters. Last, but definitely not least: my warmest thank goes to Eva. Thanks for being here with me, accompanying me in my every steps. Thanks for always being supportive, for sharing every moments of happiness and sadness, and for keeping up with me.

Preface

The here-presented dissertation is written in a cumulative way. The overall research question of the doctoral project is presented by a comprehensive introductory chapter including theoretical background and methodology, describing the used scientific methods (Part I – Introduction). This introduction completes with a corresponding bibliography. The results (Part II – Results and Discussion) of the work are based on following, already published journal articles.

1. B. Anke, T. Bredow, J. Soldat, M. Wark, M. Lerch; **Synthesis, crystal structure, and photocatalytical properties of $\text{Ba}_3\text{Ta}_5\text{O}_{14}\text{N}$** , *J. Solid State Chem.*, 2016, 233, 282–288.
2. B. Anke, T. Bredow, M. Pilarski, M. Wark, M. Lerch; **From $\text{Ba}_3\text{Ta}_5\text{O}_{14}\text{N}$ to $\text{LaBa}_2\text{Ta}_5\text{O}_{13}\text{N}_2$: Decreasing the Optical Band Gap of a Photocatalysts**, *J. Solid State Chem.*, 2017, 246, 75–80.
3. B. Anke, M. Rohloff, M.G. Willinger, W. Hetaba, A. Fischer, M. Lerch; **Improved photoelectrochemical performance of bismuth vanadate by partial O/F-substitution**; *Solid State Sci.*, 2017, 63, 1–8.

To have a consistent layout and good readability the formatting is kept identical for the entire work. Thus, the display format of the papers incorporated in the thesis is not like the published versions. Each publication has an independent introductory section; consequently some information might be repeated within the work. Every publication concludes with its related list of references. The subsequent section (Chapter 7 – Conclusion and Outlook) collects the major results and relevant information discussed in the individual publications and closes with a short outlook to possible prospective experiments in the research area. The thesis was accomplished in the period from March 2014 to January 2017 under the supervision of Prof. Dr. Martin Lerch at the Institut für Chemie at the Technische Universität Berlin.

Contents

Abstract	I
Zusammenfassung	III
Acknowledgement.....	V
Preface	VIII
Contents.....	IX

I. Introduction

1. Motivation	1
2. Theoretical Background	5
2.1. Optical band gap engineering	5
2.2. Tetragonal tungsten bronze structure	6
2.3. Bismuth vanadate	8
2.4. The Rietveld analysis	13
3. Methodology	16
3.1. Preparation	16
3.2. Furnaces	18
3.3. X-ray diffraction	21
3.4. Hot gas extraction	23
3.5. UV-Vis spectroscopy	24
3.6. Gas pycnometry	24
3.7. Photocatalysis	25
Bibliography.....	28

II. Results and Discussion

4. Publication 1	32
4.1. Abstract	34
4.2. Introduction	34
4.3. Experimental Section	35
4.4. Results and discussion	37
4.5. Conclusion	48
References	49

5. Publication 2	52
5.1. Abstract	54
5.2. Introduction	54
5.3. Experimental Section	55
5.4. Results and discussion	58
5.5. Conclusion	65
References	66
6. Publication 3	68
6.1. Abstract	70
6.2. Introduction	70
6.3. Experimental Section	71
6.4. Results and discussion	74
6.5. Conclusion	85
References	86
7. Conclusion and Outlook	89
7.1. Conclusion	89
7.2. Outlook	91
Appendices	93
A Additional information, Supplementary material	93
B List of publications	94
C List of conference contributions	96
D Awards	96
List of Tables	98
List of Figures	99

Part I.

Introduction

1. Motivation

The CO₂ content in the earth's atmosphere has reached its highest average level of over 400 ppm, as compared to 310 ppm at the beginning of the 1950s (Figure 1.1).^[1,2] This value is believed to be responsible for the increase of climate change and for other environmental issues (for example: the decrease of snow and ice deposits, the rise in sea level or the rise in acid rain). The tremendous increment of CO₂ as a consequence of our dependence on fossil fuels (i.e. coal, oil, and natural gases) demands for a strategy to reduce the need for energy from these resources. Therefore, reducing the energy demand from fossil fuels and promoting the use of renewable energy resources could potentially slow down the increase of CO₂ in the atmosphere. In other words, there is an urgent need to develop a clean, alternative, and renewable energy resource to replace current fossil energy resources.

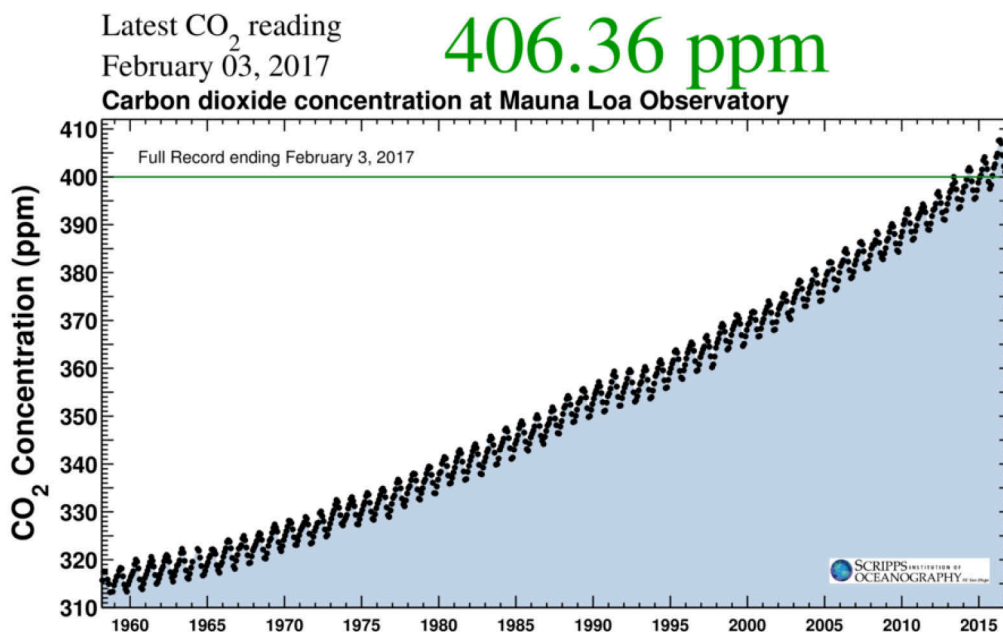


Figure 1.1: For the first time, the atmospheric CO₂ concentration at Mauna Loa stayed above the symbolic milestone of 400 ppm for the full year in 2016, including September's seasonal low. Source: UC San Diego (<https://scripps.ucsd.edu/programs/keelingcurve/>).

Besides wind power, biomass, geothermal, and hydropower, solar energy is a promising candidate for renewable energy. The power of annual incident solar radiation on the earth's surface is approximately 120,000 terawatts of electromagnetic radiation, a quantity that far exceeds the total need for energy consumption.^[3] The most developed

technology is the transformation of photons from the sun into electricity by solar cells. The electrical energy gained by those cells, however, has to be stored for use during the night. For the direct conversion of sunlight into energy the use of chemical fuels is a promising method to overcome this problem. Solar water splitting into hydrogen and oxygen using semiconducting materials is of particular interest to the scientific community as it is a carbon-free process, resulting in zero net emission of CO₂. Materials used for water splitting need to be earth-abundant and highly stable in a wide range of pH. Furthermore, a suitable band gap to efficiently use solar energy and low costs in fabrication, easy maintenance, and operation are required.

The first photoelectrochemical (PEC) water splitting device was developed by Fujishima and Honda in 1972 using semiconducting TiO₂ photo electrodes.^[4] Nowadays the highest efficiency in a solar to-fuel device has reached over 12 % using GaAs photoelectrochemical/ photovoltaic cells^[5,6] or perovskite photovoltaics^[7] to produce solar hydrogen. However, such highly efficient techniques are based upon rare materials (Ga) or toxic chemicals (lead in perovskite) with poor stability.

From this time forward, the search for semiconductors with improved properties has been a challenging task for research. There are three very different approaches to this topic:

- Production of new compounds but with the abovementioned properties (i.e. favorable, non-toxic, and abundant on the earth)
- Improvement of the catalyst properties by restructuring the material surface (i.e., nanostructured surfaces, construction of heterojunctions)
- Optimization of existing catalysts by means of targeted changes in the chemical-physical properties (i.e. doping and substitution of the cat- and anions)

Especially the doping and substitution in a semiconductor material has been given the attention recently to change its electronic structure. Molybdenum and tungsten were found to be suitable cationic dopants increasing the photocatalytic water splitting performance due to enhancement of the amount of free charge carriers within the material.^[8-14] Besides cationic doping, also anion substitution, especially with nitrogen or fluorine, seems to lead to a decrease of the optical band gap resulting in an increase

of photocatalytic performance.^[15,16] However, such materials have not been studied in detail so far.

2. Theoretical Background

2.1. Optical band gap engineering

The band gap is an energy range in a solid where no electron states can exist. In graphs of the electronic band structure of solids, the band gap generally refers to the energy difference (in electron volts) between the top of the valence band (HOMO) and the bottom of the conduction band (LUMO) in insulators and semiconductors.

The width of the band gap is determined by the extent of overlap of the valence orbitals, and by the difference between the electronegativities of the cations and anions involved. Van Vechten *et al.*^[17] established a concept derived from these factors (that is, valence-orbital overlap and electronegativity difference) that allows a design of band gaps in semiconductors, this concept is nowadays called “*band gap engineering*”. The optical band gap of a material can be controlled or altered by adjusting the composition of certain semiconductor alloys, such as in $\text{Ca}_{(1-x)}\text{La}_x\text{TaO}_{(2-x)}\text{N}_{(1+x)}$.^[18] Jansen *et al.* reported that the variation of x between 0 and 1 enables a fine-tuning of colors through the desired range, from yellow through orange to deep red. In their theoretical work from 2016, Modak and Gosh show the effect of the incorporation of nitrogen, fluorine, and other halides into pure KTaO_3 .^[19] The incorporation of nitrogen lowers the optical band gap drastically by increasing the valence band (see Figure 2.1).

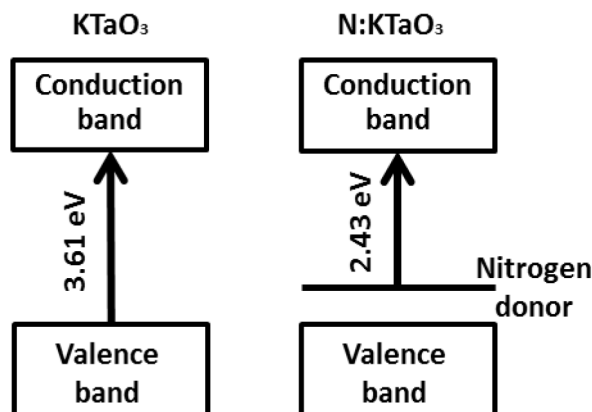


Figure 2.1: Band edge alignment of undoped and N-doped KTaO_3 .

2.2. Tetragonal tungsten bronze structure

The tetragonal tungsten bronze (TTB) structure was described in 1949 by Magneli^[20] for $K_{0.57}WO_3$ ($K_{2.85}W_5O_{15}$). In 1953, ferroelectric properties of $PbNb_2O_6$ ($Pb_{2.5}Nb_5O_{15}$)^[21] were demonstrated. In 1967, non-linear optics properties were studied on TTB crystals in IBM and Bell Telephone Laboratories.^[22] Since 1970, dielectric studies were carried out simultaneously in the USA, the USSR, Japan, Great Britain, and France. This shows the incredibly large span of this structure. The crystal structure is described in more detail below.

In the TTB structure (Figure 2.2) with a general formula $A_2BC_2M_5X_{15}$ are 4 cation sites: from largest to smallest are a large tricapped trigonal prism (A), a slightly distorted cuboctahedron (B), a small tricapped trigonal prism (C), and small and highly charged cations are in the octahedral M sites.^[23] Occupation of sites A, B, and C is primarily a function of the number of cations and their size. The smallest site (C) is typically occupied only by very small cations such as lithium. Table 2.1 gives a short overview of the localization of various ions in the different crystallographic sites.

Table 2.1: Localization of various ions in the different crystallographic sites.^[24]

Site	C.N.	Ions
A	15	K^+ , Rb^+ , Cs^+ , Tl^+ Ca^{2+} , Sr^{2+} , Ba^{2+} , Pb^{2+}
B	12	Na^+ , K^+ , Ag^+ , Ca^{2+} , Sr^{2+} , Ba^{2+} , Cd^{2+} , Eu^{2+} , Pb^{2+} Ln^{3+} , Bi^{3+} , Ce^{4+} , Th^{3+} , U^{4+}
C	9	Li^+ , Na^+ , Mg^{2+} , Ni^{2+} , Cu^{2+} ...
M	6	Mg^{2+} , $V^{2+/3+/5+}$, $Fe^{2+/3+}$, Co^{2+} Ti^{4+} , Zr^{4+} , Sn^{4+} , $Nb^{4+/5+}$, Ta^{5+} , $W^{5+/6+}$, M^{6+}
X		F^- , O^{2-} , N^{3-}

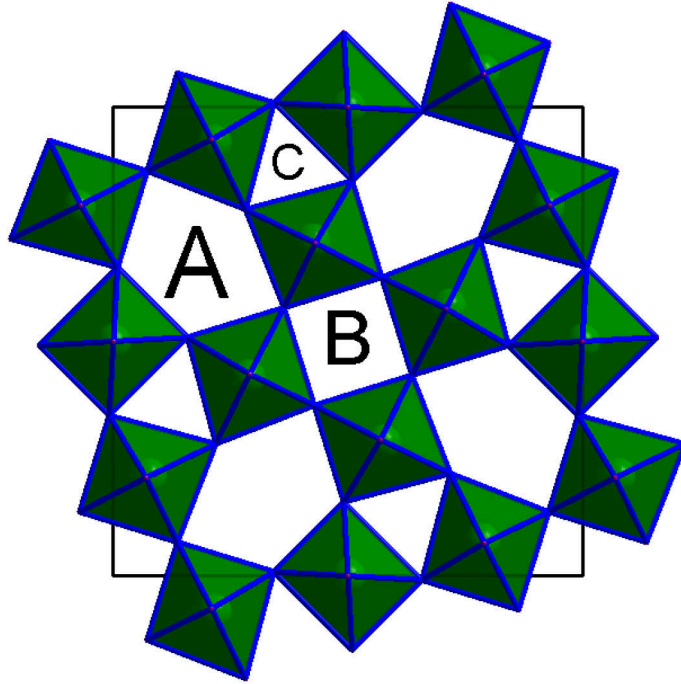


Figure 2.2: Schematic projection of the TTB crystalline network ($A_2BC_2M_5X_{15}$) along the c axis (A, B, and C correspond to cationic sites with 15, 12, and 9 coordination numbers, respectively).

The chemical stability is high when big cations (Ba^{2+} , Sr^{2+}) occupy the A site, small, and low charged ions (Li^+) are on the C-site and small but highly charged cations (Ta^{5+} , Nb^{5+}) are on the M-site. The various types of stoichiometry depend on the existence of vacancies (\square) in either one or another site, as shown by the examples below:

- all sites are fully occupied: $K_3Li_2Nb_5O_{15}$ ^[25] ($A_2BC_2M_5X_{15}$)
- half of the C-site is empty: $K_3NiNb_5O_{15}$ ^[26] ($A_2BC\square M_5X_{15}$)
- C-site is empty: $Ba_3Ta_5O_{14}N$ ^[27] ($A_2BM_5X_{15}$)
- B and C-sites are empty: $BaBiNb_5O_{15}$ ^[28] ($A_2\square\square_2M_5X_{15}$)

All conceivable solid solutions can also be obtained between each kind of non-stoichiometric compositions e.g. $K_{5-x}Li_xTa_{5-y}Nb_yO_{15}$.^[29] The possibility to change the material composition as desired makes it interesting for research. Many different fields of application have been tested, from ferroelectricity to multiferroics^[30] or the photocatalytic properties^[27,31] of these materials.

2.3. Bismuth vanadate

In nature BiVO_4 is available as the mineral pucherite with an orthorhombic crystal structure.^[32] However, BiVO_4 prepared in the laboratory does not assume the pucherite structure but crystallizes either in a scheelite- or a zircon-type structure.^[33,34] The scheelite structure can crystallize in the monoclinic crystal system ($I2/b$ $a = 5.1787(5) \text{ \AA}$, $b = 5.1042(5) \text{ \AA}$, $c = 11.6953(11) \text{ \AA}$, $\gamma = 90.260(2)^\circ$)^[35] or the tetragonal crystal system ($I4_1/a$, $a = b = 5.147 \text{ \AA}$, $c = 11.721 \text{ \AA}$) while the zircon-type structure is tetragonal ($I4_1/a$; $a = b = 7.303 \text{ \AA}$ and $c = 6.584 \text{ \AA}$).^[36]

In both scheelite-type structures, each vanadium ion is tetrahedrally coordinated by four oxygen ions and each bismuth ion is surrounded by eight oxygen ions from eight different VO_4 tetrahedral units (Figure 2.3). Each O atom in this structure is coordinated to one V center and two Bi centers. The difference between the tetragonal and monoclinic scheelite structure is the following: the polyhedra around V and Bi ions are more significantly distorted in the monoclinic structure, which removes the four-fold symmetry necessary for a tetragonal symmetry. For example, in tetragonal scheelite all four V–O bond lengths are equal, but in a monoclinic scheelite structure two different V–O bond lengths exist ($1.631(7) \text{ \AA}$ and $1.689(8) \text{ \AA}$). In the same way, while only two nearly similar Bi–O distances exist in the tetragonal scheelite structure (2.453 \AA and 2.499 \AA), the Bi–O distances in the monoclinic scheelite structure differ significantly ($2.408(8) \text{ \AA}$, $2.425(8) \text{ \AA}$, $2.538(7) \text{ \AA}$ and $2.672(7) \text{ \AA}$).^[35]

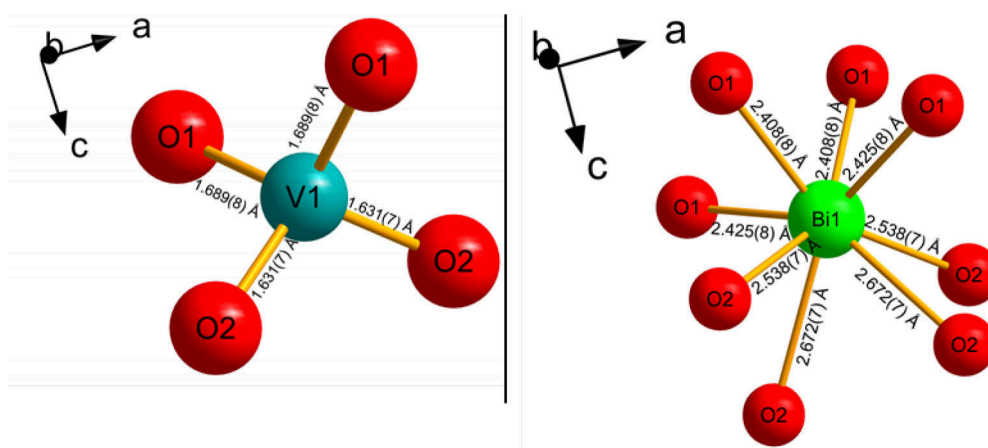


Figure 2.3: V-O_4 tetrahedra and Bi-O_8 polyhedra in monoclinic scheelite BiVO_4 with the determined bond lengths (\AA).

It should be mentioned that the space group $I2/b$, which was originally reported for the monoclinic scheelite structure of BiVO_4 , is a non-standard setting.^[37] It can be transformed to $C2/c$, which is used in some new studies of BiVO_4 . After this transformation, the new cell parameters are $a' = 7.254 \text{ \AA}$, $b' = 11.6987 \text{ \AA}$, $c' = 5.0999 \text{ \AA}$, and $\beta' = 134.367^\circ$. The choice of the body-centered monoclinic cell, $I2/b$, has the advantage of easily showing its structural relationship to the tetragonal scheelite structure using an identical unit cell choice and crystallographic axes.^[38]

In the zircon-type structure, vanadium is still surrounded by four oxygen atoms and bismuth is coordinated by eight oxygen atoms. However, each bismuth ion is only surrounded by six VO_4 units because two VO_4 units provide two oxygen atoms to bismuth. All oxygen atoms are connected to two bismuth centers and one vanadium center.

A synthesis at room temperature, for example a precipitation, results in a zircon-type structure. A phase transition from tetragonal zircon to monoclinic scheelite was found to be irreversible at 670–770 K (Figure 2.4).^[33] Among scheelite structures, the tetragonal phase is a high temperature phase and the phase transition between monoclinic scheelite BiVO_4 and tetragonal scheelite BiVO_4 is reversible at 537 K. The critical temperature of this transition was determined by a Landau fit (Figure 2.5).

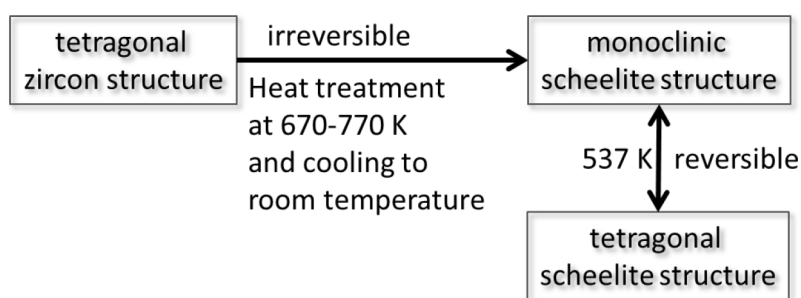


Figure 2.4: Phase transition in BiVO_4 .

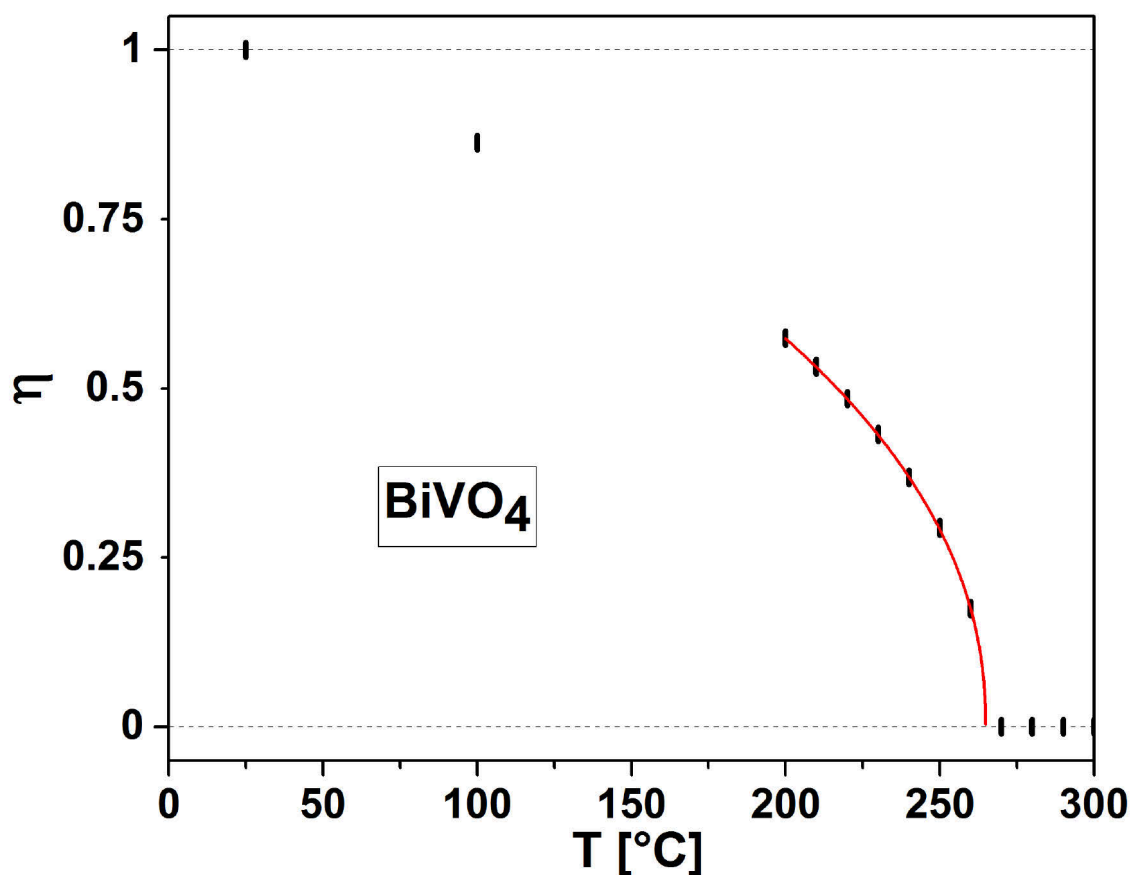


Figure 2.5: Temperature dependence of a normalized order parameter for BiVO_4 .

The photocatalytic activity of BiVO_4 depends to its crystal structures. Kudo *et al.* reported that BiVO_4 with a monoclinic scheelite structure showed the highest photocatalytic activity for water oxidation to O_2 with Ag^+ ions as the electron scavengers.^[33] The enhanced photoactivity of scheelite-type over zircon-type BiVO_4 appears to be mainly due to the enhanced photon absorption of the scheelite phase because the band gap energies for scheelite- and zircon-type BiVO_4 are 2.4 eV and 2.9 eV, respectively.^[39] The schematic band structures of tetragonal zircon-type BiVO_4 and monoclinic scheelite BiVO_4 proposed by Kudo *et al.* are shown in Figure 2.6.^[39]

Among scheelite-type BiVO_4 phases, Tokunaga *et al.* reported that a sample having a monoclinic scheelite structure shows much higher activity for the photocatalytic water oxidation than a sample having a tetragonal scheelite structure.^[33] The band gap energies of the tetragonal and monoclinic scheelite BiVO_4 are comparable and the observed difference in photocatalytic activity was attributed to the more severe distortion of the metal polyhedra present in the monoclinic scheelite BiVO_4 .^[33] As discussed earlier, the surroundings of bismuth in the monoclinic scheelite structure is more distorted than in the tetragonal scheelite structure. Tokunaga *et al.* stated that this

distortion pronounces the local polarization, which favorably affects the electron–hole separation and, therefore, the photocatalytic properties.

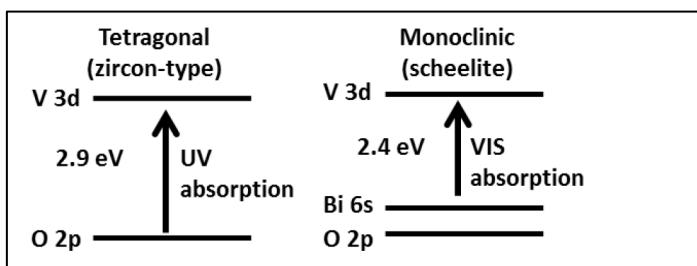


Figure 2.6: Schematic band structures of tetragonal zircon-type BiVO_4 and monoclinic scheelite BiVO_4 proposed by Kudo *et al.*^[39]

Doped BiVO_4 systems

Doping, the intentional introduction of impurity atoms into a material, is a fundamental method for regulating the properties of a bulk semiconductor. Even a very small amount of impurities can change the electrical and optical properties extremely. Depending on the particular kind of the dopant, changes in the optical band gap energy or band edge positions can be expected.^[40] However, the effect of doping may not always be favorable because it can impede charge transport by providing scattering centers and enhance electron–hole recombination. Therefore, identifying suitable dopants and their concentrations is important to increase the overall performance of the material. In order to identify effective dopants for BiVO_4 , Ye *et al.* performed rapid screening of BiVO_4 photocatalysts doped with a variety of metals (Ti, W, Ir, Cu, Sr, Zn, Fe, B, Nb, Co, Rb, Ru, Ga, Ag, Pb, and Sn) using a scanning electrochemical microscopy technique.^[41] The photocatalyst arrays were prepared by a computer-controlled sprayer that dispenses varying ratios of bismuth, vanadium, and dopant-containing solutions (with a concentration of 5–10 at%) on each spot, which were annealed at 500 °C in air to produce the photocatalysts. The photoelectrochemical performances of these arrays were evaluated and showed that only samples doped with tungsten led to a remarkable enhancement in photocurrent. Sn, Co, Pd, Rh, Ru, Ag, Ga, Sr, and Ir caused a negative effect, while the rest showed no noticeable effect.

Luo *et al.* prepared BiVO₄ electrodes doped with various metal ions (W, Mo, Ti, La, Fe, Ta, Zr, Si, Sr, Zn, and Ag) by a modified metal-organic decomposition method and observed that only Mo⁶⁺ or W⁶⁺ doping enhanced the photocurrent.^[42] Especially, molybdenum-doped BiVO₄ samples prepared from a 3 at% molybdenum solution showed the best increase in photocurrent. The observed enhancement was attributed to a possible increase in the hole diffusion length and the enhanced conductivity. A Raman study validated that Mo⁶⁺ ions were located at the V⁵⁺ sites. The increase in carrier density by Mo-doping was confirmed by the slope change in the Mott–Schottky plots but the change in the flat band potential was insignificant. The performance of Mo-doped BiVO₄ was further improved by surface electrochemical pretreatment, in order to remove Mo-rich accumulations (for example MoO_x) on the surface which could act as recombination centers.^[43]

A non-metal element, P, was also incorporated into BiVO₄ by the urea-precipitation method where PO₄³⁻ anions were added as a phosphor precursor to substitute a small fraction of VO₄³⁻ ions in the precursor solution.^[40] Samples of Bi(VO₄)_{1-x}(PO₄)_x with $x = 0.019, 0.006, \text{ and } 0.002$ were produced. The incorporation of phosphor into the host structure causes shifts of the XRD reflections to smaller 2θ values, indicating an increase in cell volume. Even a negligible increase in the band gap energy was observed in the UV-vis absorption spectra. When the BiVO₄ and Bi(VO₄)_{1-x}(PO₄)_x powder samples were prepared as electrodes using electrophoretic deposition, Bi(VO₄)_{0.998}(PO₄)_{0.002} showed the best performance by generating a significantly higher photocurrent than the pristine BiVO₄ electrode. DFT calculations by the same authors confirmed that the reduced charge transfer resistance could be the result of phosphor doping which increases the charge carrier density.

In this work a simple route to phase-pure fluorine-modified BiVO₄ is reported. Incorporation of fluorine into BiVO₄ generates cation vacancies leading to the formation of Bi_{0.94}V_{0.94}O_{3.54}F_{0.46}. Investigations of the photoelectrochemical behavior show that F-incorporation significantly improves the performance of BiVO₄ photoanodes for photo(electro-)catalytic water oxidation.

2.4. The Rietveld analysis

The Rietveld analysis or Rietveld refinement is a mathematical technique, devised by Hugo Rietveld, for the analysis and evaluation of powder diffraction data.^[44-47] Using a theoretical line profile with the similar structure as the measured sample, which serves as a reference, a theoretical powder diffraction diagram is created and iteratively compared to the measured data. The comparison is based on the least square method. The Rietveld analysis consists of two segments, i) the profile and ii) structure fitting combined with the background adjustment. Certain functions are available for the reflection shape fitting, a linear combination of a Gauß and Lorentz function is commonly used, the Pseudo-Voigt function. The Gauß part is describing the sample specific influences on the form of the reflection and the Lorentz part the effects resulting from the measurement setup.^[44] Simultaneously, it is possible to determine changes of the unit cell parameters, such as lattice parameters, atomic position, thermal displacement or occupation. The Rietveld analysis makes it also possible to determine the composition of multi-phased materials due to the use of integral intensities. Important for the profile functions are the integral intensities of the k reflection I_k , the reflex position $2\theta_k$ and the full width at half maximum H (FWHM).

The FWHM is described through the parameters U , V , and W as such

$$H = (U \tan^2 \theta + V \tan \theta + W)^{\frac{1}{2}} \quad (1)$$

During the refinement, the parameters U , V , and W are used to fit the profile. The quality of a Rietveld refinement is evaluated according to the agreement of the observed values $y_i(\text{obs})$ with the calculated values $y_i(\text{calc})$, and is given by residual values (R-values). The value R_{wp} (weighted R-value) indicates the mean deviation of the calculated data to the observed diffraction pattern and is minimized during the refinement.

$$R_{wp} = \sqrt{\frac{\sum w_i (y_i(\text{obs}) - y_i(\text{calc}))^2}{\sum w_i (y_i(\text{obs}))^2}} \quad (2)$$

w_i - weighting factor at point i

$y_i(\text{obs})$ - measured intensity at point i

$y_i(\text{calc})$ - calculated intensity at point i

Ideally this value is zero, which can never be achieved due to the signal to noise ratio, thus the R_{exp} value is calculated, indicating the best possible value and the accuracy of the measurement.

$$R_{exp} = \sqrt{\frac{N-P+C}{\sum w_i(y_i(obs))^2}} \quad (3)$$

N - Number of measured points

P - Number of parameters

C - Number of parameter linkings

In contrast, the value R_{Bragg} is calculated from the intensities of the n reflections that are present in the pattern.

$$R_{Bragg} = \sqrt{\frac{\sum |I_n(obs) - I_n(calc)|}{\sum I_n(obs)}} \quad (4)$$

$I_n(obs)$ - measured integral intensity of the n reflection

$I_n(calc)$ - calculated integral intensity of the n reflection

The goodness of fit S is formed by the ratio of the two former R-values R_{wp} and R_{exp} . In the ideal case S should approach a value of 1.

$$S = \frac{R_{wp}}{R_{exp}} \quad (5)$$

In this work the program package Fullprof Suite^[46] was used for the Rietveld analysis.

3. Methodology

3.1. Preparation

The precursors used for this work were produced in two different ways, by a modified polymerizable complex method (Pechini route) and a standard wet-chemical precipitation.

3.1.1. Pechini

The new compounds were synthesized using the modified Pechini route (Figure 3.1).^[48,49] For this, a Ba-Ta (3:5) and a La-Ba-Ta (1:2:5) precursor had to be prepared first. For these precursors, a lanthanum, barium, and a tantalum citrate solution were prepared. For the tantalum citrate solution, 25 g of TaCl_5 were added to a three-necked flask in the Ar-Glovebox. Thereafter, TaCl_5 was dissolved under Schlenk conditions with a citric acid solution dissolved in ethanol. For the lanthanum citrate solution, lanthanum chloride powder (Sigma Aldrich, 99.9 %) was dissolved in an ethanol/water

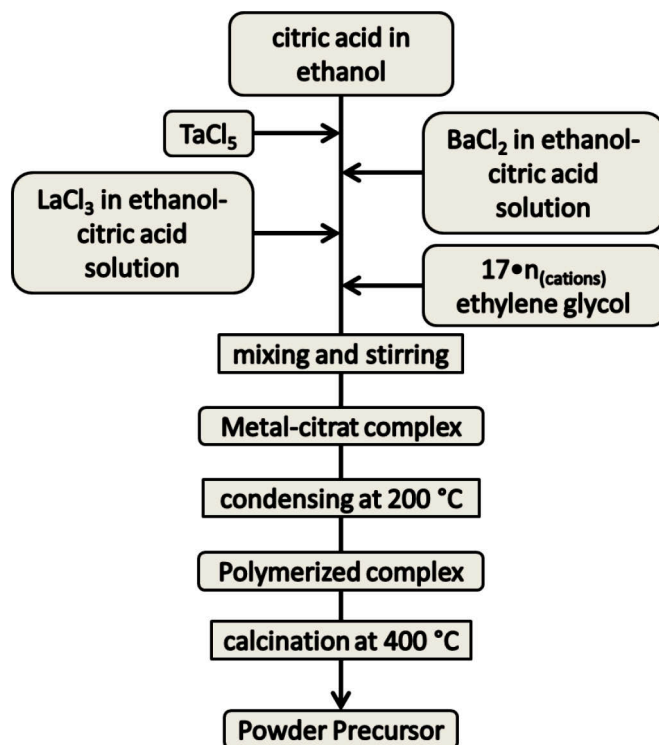


Figure 3.1: Flow chart for preparing amorphous powder precursors by the Pechini method.

mixture containing citric acid (Sigma Aldrich 99.5 %). The latter was used in a molar excess of 12 times the LaCl_3 . Barium chloride (Sigma Aldrich, 99.9 %) was dissolved in ethanol, containing citric acid, to prepare the citrate solution. The cation concentration of the respective citrate solutions was determined gravimetrically. For the sol-gel process, the citrate solutions were added to a beaker in the desired stoichiometric ratio. In the next step, ethylene glycol ($n(\text{EG}) = 17n(\text{cations})$) was added to this

solution. The mixture was then gradually heated to 200 °C under ambient conditions until a gel was formed. In the last step, the resin-like mass was transferred from the beaker to a corundum crucible and placed in a chamber furnace for 16 hours at a temperature of 400 °C. The resulting precursor was colorless and amorphous.

For the nitration of the precursor, the ammonolysis step was carried out with an ammonia-oxygen mixture. Numerous tests using different variations of temperature, holding time, gas mixing ratio, and calcination temperature were performed. The temperature was varied between 700 °C and 900 °C. Additionally, holding times between 1 h and 48 h as well as heating rates between 200 K/h and 600 K/h were carried out. The ammonia and oxygen gas volume flows (5 L/h – 15 L/h NH₃, 0.01 L/h – 0.3 L/h O₂) were also changed. Ultimately, the conditions listed in Table 3.1 with the highest phase purity led to the new compounds crystallizing in the tetragonal tungsten bronze type.

Table 3.1: Synthesis conditions for the new compounds Ba₃Ta₅O₁₄N and LaBa₂Ta₅O₁₃N₂.

Compound	T [°C]	Holding Time [h]	Heat rate [K/h]	NH₃ [L/h]	O₂ [L/h]
Ba ₃ Ta ₅ O ₁₄ N	850	24	400	10	0.03
LaBa ₂ Ta ₅ O ₁₃ N ₂	875	20	400	10	0.03

3.1.2. Wet-chemical precipitation

Pristine bismuth vanadate was synthesized in an aqueous medium at room temperature under ambient pressure. Bi₂O₃ and NaVO₃ were dissolved in concentrated nitric acid and mixed in a molar ratio 1:2. After stirring this solution for 4 hours, sodium hydroxide was added until the pH value reached basic conditions (pH = 12). The solution was stirred again for 4 hours. The resultant yellow precipitation was filtered and then washed with distilled water several times to remove impurities and residual materials, and dried at 60 °C for 12 hours. After that, the bright yellow powder was treated in the fluorination furnace.

3.2. Furnaces

Two different types of ovens were used for the syntheses of the samples, for the oxide nitrides an ammonolysis furnace with direct gasification was selected and for the O/F substitution in the BiVO_4 -samples a fluorination apparatus with an inner corundum tube was used.

The ammonolysis furnace

For the preparation of the tantalum oxide nitride-based compounds occurring in this work, a tube furnace SR-A 60-300 / 12 type from Gero (Neuhausen) was used. The Gero tube furnace (Figure 3.2 center) is equipped with a reaction tube made of amorphous silicon dioxide. This has a length of 500 mm and a diameter of 55 mm. However, ammonia decomposes upon heating into its elements nitrogen and hydrogen; especially in the case of long reaction tubes ammonia is dissociated before the sample is reached. Therefore, the pipes used herein have a so-called rapid gas supply. An additional tube with a considerably smaller diameter is integrated into the reaction tube, which serves to treat the sample directly with the reaction gas (Figure 3.2 right). The temperature control takes place via a Ni-Cr / Ni thermocouple, the maximum working temperature is 1150 °C. The synthesis parameters such as temperature, heating rate, and holding time are controlled by an external temperature controller. The adjustment of the reaction gases and the flow rates are carried out via upstream mass flow controllers (Figure 3.2 left) of the DeltaSmart MassFlow / SLA5850 type from Brooks Instrument (Pennsylvania). The tube furnace of the company Gero is hinged. The sample can be cooled more quickly by opening the oven after the heating program has been completed. As a result of this influence on the cooling rate, an undesired connection can be prevented during cooling.

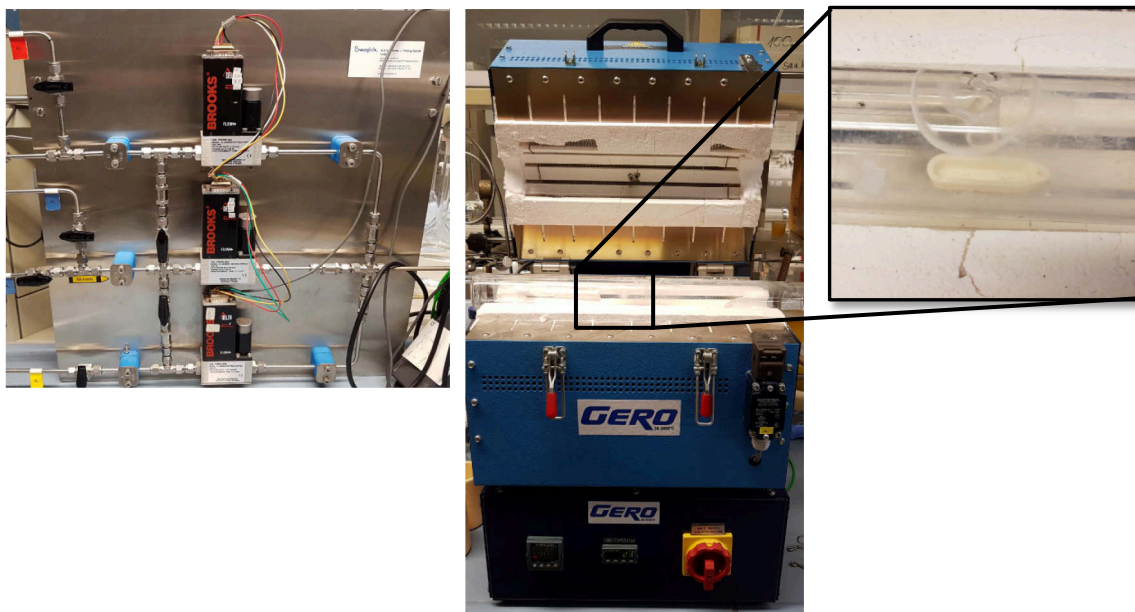


Figure 3.2: left: gas flow controller for NH_3 , O_2 and N_2 ; mid: tube furnace from Gero Typ SR-A 60-300/12; right: reaction space under the rapid gas supply.

The fluorination furnace

Fluorine-containing samples were prepared by a solid-vapor reaction using an indirect gas flow apparatus (see Figure 3.3). Loose powder of the sample was loaded in a small corundum boat, which in turn was placed inside a larger corundum boat containing varying amounts of polyvinylidene fluoride (PVDF). This arrangement advantageously prevents contact between the reagents in either solid or liquid form. It is very important to prevent the photocatalysts from any carbon pollution in order to achieve good results; the final product is without any of the several contaminations. The nested boats were then placed inside a corundum tube with one closed end and then placed in a horizontal tube furnace with a low nitrogen gas flow of ~ 5 L/h. With this configuration an overpressure could be avoided. The temperature was set to 380 °C for 24 hours. Thermogravimetric and mass spectroscopy studies revealed that the PVDF decomposition only emits HF under inert gas.

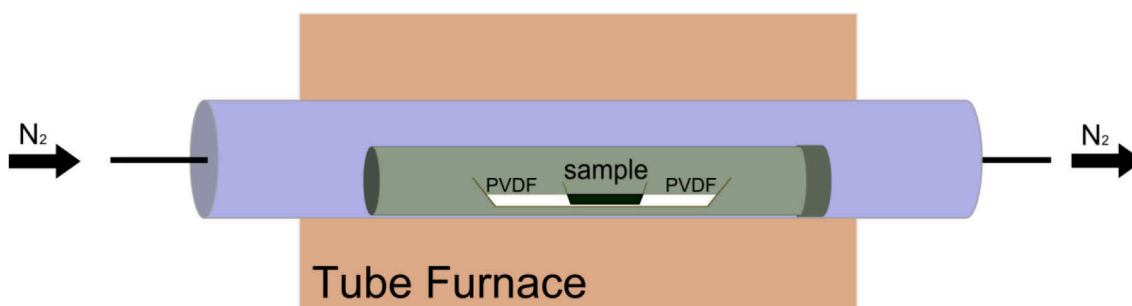


Figure 3.3: Sketch of fluorination apparatus. The inner corundum boat contains the sample to be fluorinated and the outer boat is filled with PVDF.

3.3. X-ray diffraction

In solid state chemistry diffraction methods are among the most important analytical characterization techniques.^[50,51] They are employed for structure determination in crystalline materials and can be used to identify structural properties such as phase composition, lattice parameters, grain size, or preferred orientation. The technique is based on the diffraction of X-rays at the atoms of the crystal. The crystal lattice consists of parallel planes with distance d that are identified by Miller indices (h, k, l). Because of the interatomic distances in the order of magnitude of $\sim 10^{-10}$ m, especially X-rays are suitable for scattering experiments. The fundamental principle is based on the interaction between X-ray photons and the electron shell, respectively. The theoretical principle of the diffraction is described by Bragg's law (Equation 6)^[52]:

$$n\lambda = 2d_{hkl} * \sin\theta \quad (6)$$

λ - wavelength of incident beam

d - distance between the lattice planes (hkl)

θ - diffraction angle

n - describes the order of diffraction and is always an integer

The equation describes the interaction of the incident beam (i.e. 1.54 Å for Cu K α 1) with the sample and defines the general condition for constructive interference. It is assumed that the crystal consists of layers, on which the radiation is reflected, and constructive interference occurs when the path length difference is an integer number of the wavelength. The diffracted waves of different lattice planes cause a certain diffraction pattern, which contains information about the atomic arrangement in the crystalline material.

As mentioned above, X-rays are scattered at the electrons of the shell, the scattering power of an atom is described by the atomic form factor f_i , which depends linearly on the number of electrons in the atom. Hence, it is easy to distinguish between elements with a large difference in electron number. Furthermore, the atomic form factor is a

function of the wavelength and the diffraction angle, resulting in decreasing intensities with increasing angles. A disadvantage in X-ray diffraction is that the distinction between elements with similar atomic number, such as nitrogen and oxygen is not possible, neutron scattering is used in these cases.

The X-ray powder diffraction experiments were conducted with the X'Pert Pro system from PANalytical (PANalytical B.V, Almelo, Netherlands). It consists of a θ/θ setup in Bragg-Brentano geometry.^[52,53] The X-ray source consists of copper. The Bremsstrahlung and the radiation below the $K\alpha$ wavelength are filtered through a Ni-filter. The setup uses no monochromatic light, which results in the presence of $\text{Cu } K_{\alpha 1}$ and $\text{Cu } K_{\alpha 2}$ radiation (with a ratio of 2 to 1). An automatic divergence aperture is used to keep the irradiated sample area constant with varying angles. This must be taken to account for the following Rietveld analysis. As a detector, a Si(Li)-semiconducting detector was used. The supplied software X'Pert Highscore Plus v.2.2.1 was used for a first quick evaluation of the measurement through the Inorganic Structure Database (ICSD, FIZ Karlsruhe, Germany and US Department of Commerce, USA).

3.4. Hot gas extraction

The elemental analysis for the determination of the nitrogen and oxygen content of a substance is carried out by hot gas extraction (LECO TC-300/EF-300). For this purpose 3 to 4 mg of the sample are heated in the helium stream at 2700 °C for 50 seconds. Thus elementary nitrogen and oxygen are released from the sample. The oxygen from the sample reacts with the graphite to form carbon monoxide, which is then catalytically converted to carbon dioxide by copper oxide. The amount of CO₂ is detected by absorption spectroscopy in an infrared measuring cell, whereby ultimately the oxygen content can be determined.^[54] The nitrogen content is determined in a thermal conductivity measuring cell. The helium–nitrogen–gas mixture has a lower thermal conductivity than pure helium, an integrated “*Wheatstone bridge*” measures the electrical resistance in the cell, and the change of the electrical resistance is proportional to the nitrogen content.^[54] For calibration, ZrO₂, and steel (LECO calibration sample, N: 5000 ppm) were used as standard materials. The accuracy is ~ 2 % of the N/O content.

3.5. UV-Vis spectroscopy

Diffuse reflectance spectra were collected with a Jasco V670 spectrometer. Absorbance spectra in the wavelength range from 200 nm to 1000 nm were calculated from the measured diffuse reflectance with the Kubelka-Munk function (Equation 7).

$$(R) = \frac{(1-R)^2}{2R} = \varepsilon c \frac{1}{s} \quad (7)$$

where R is the reflectance, ε is the absorption coefficient, c the concentration of absorbing species, and s the scattering coefficient. The optical band gap was determined using the modified Tauc equation, $[F(R)h\nu]^{\frac{1}{n}} = A(h\nu - E_g)$, with $F(R)$ the Kubelka-Munk function, $h\nu$ the photon energy, E_g the optical band gap, and A a proportionality constant. The value of the exponent n denotes the nature of the transition ($2 =$ indirect; $\frac{1}{2} =$ direct).

With the phenomenological Kubelka-Munk theory,^[55] it is possible to establish a relationship between scattered and absorbed light. However, it applies only to low-absorbing and optically infinitely thick samples. The non-absorbing material was magnesium oxide (ABCR, 99.95%) added to all samples in a 1: 1 ratio.

3.6. Gas pycnometry

Experimental density values of the samples were measured using a Quantachrome helium multipycnometer, where the pressure change of helium in a calibrated volume is measured to calculate the sample volume. Helium penetrates into smallest pores and crevices and permits to approach the real volume of the sample.

3.7. Photocatalysis

Photocatalytic hydrogen generation

Photocatalytic hydrogen generation was measured in the working group of Michael Wark using a home-made air-free closed gas system and a double-walled inner irradiation-type quartz reactor. As a light source, a 700 W Hg mid-pressure immersion lamp (Peschl UV-Consulting, set to a power of 500 W) was used for irradiation and cooled with a double-walled quartz mantle using a thermostat (LAUDA). Gas evolution was detected online using a multi-channel analyzer (Emerson) equipped with a detector for the determination of the concentration of hydrogen (thermal conductivity detector), oxygen (paramagnetism), and carbon dioxide (IR). Argon was used as carrier gas, the continuous gas flow was controlled by a Brockhorst mass flow controller. The gas flow was set to 50 NmL/min (normal flow throughput: gas flow at ambient temperature and pressure per minute).

All reactions were performed at 13 °C. 300 mg of photocatalyst is suspended in 550 mL water and 50 mL methanol (aqueous methanol photo reforming). For a homogeneous suspension a subsequent pre-treatment in the ultrasonication bath for 10 minutes at 30 °C was performed. Before any photocatalytic reaction was initiated, the whole system including the photocatalyst was flushed with argon at 100 NmL/min for 30 minutes to remove any trace of air. In previous measurements Rh was obtained as the most effective co-catalyst for barium tantalates with an optimum loading of only 0.0125 wt.-%. Rh^[56] nanoparticles were deposited onto the photocatalyst materials via reductive photo deposition with a specific amount of Na₃RhCl₆ (99.999%, Aldrich) precursor solution using the setup described below. For measurements under visible light an aqueous 2 M NaNO₂ solution was used as filter.

Photocatalytic oxygen generation

Electrochemical measurements were carried out in the working group of Anna Fischer. A home-built 3-electrode-setup consisting of the working electrode (Photoanode), a Pt-wire counter electrode, and a reversible hydrogen reference electrode (RHE) provided by Gaskatel were used for the electrochemical measurement. The potential of the working electrode with respect to the reference electrode was controlled by a potentiostat (Biologic SP-150). The Photoanode was illuminated by a 150 W Xe-lamp (Lumatec Superlite equipped with UV cut-off filter, illuminating spectral range = 400-

700 nm), mounted at a reproducible and constant distant of 5 cm from the photoanode surface. The light intensity at the electrode surface was adjusted to 100 mW/cm² using a Si-diode light meter (Extech). J-V-measurements were conducted in 0.1 M potassium phosphate buffer at pH 7.3 using a scan rate of 20 mV/s.

Electrode preparation

Electrode preparations were accomplished in the working group of Anna Fischer. A photo-assisted electrodeposition method based on the procedure reported by Durrant *et al.* was used to deposit a cobalt phosphate-based water oxidation catalyst (CoPi) onto the working-electrode surface.^[57] The working electrode was immersed in 0.1 M potassium phosphate buffer at pH 7.3 containing 0.5 mM cobalt nitrate and a constant potential of 1.2 V vs. RHE was applied under illumination. To ensure a comparable amount of deposited CoPi for all samples, the deposition was stopped after a charge of 130 mC was flown.

Bibliography

- [1] J. Rogelj, W. Hare, J. Lowe, D. P. van Vuuren, K. Riahi, B. Matthews, T. Hanaoka, K. Jiang, M. Meinshausen, *Nature Climate change* **2011**, *1*, 413.
- [2] State of the Climate: Global Analysis for Annual 2016, *NOAA National Centers for Environmental Information* **2017**, <http://www.ncdc.noaa.gov/sotc/global/201613>.
- [3] N. Armaroli, V. Balzani, *Angew. Chem. Int. Ed. Engl.* **2007**, *46*, 52.
- [4] A. Fujishima, K. Honda, *Nature* **1972**, *238*, 37.
- [5] O. Khaselev, *Science* **1998**, *280*, 425.
- [6] J. Y. Kim, G. Magesh, D. H. Youn, J.-W. Jang, J. Kubota, K. Domen, J. S. Lee, *Scientific reports* **2013**, *3*, 2681.
- [7] M. Higashi, K. Domen, R. Abe, *J. Am. Chem. Soc.* **2013**, *135*, 10238.
- [8] F. F. Abdi, N. Firet, R. van de Krol, *ChemCatChem* **2013**, *5*, 490.
- [9] S. P. Berglund, A. J. E. Rettie, S. Hoang, C. B. Mullins, *Phys. Chem. Chem. Phys.* **2012**, *14*, 7065.
- [10] H. W. Jeong, T. H. Jeon, J. S. Jang, W. Choi, H. Park, *J. Phys. Chem. C* **2013**, *117*, 9104.
- [11] Y. Park, K. J. McDonald, K.-S. Choi, *Chem. Soc. Rev.* **2013**, *42*, 2321.
- [12] K. P. S. Parmar, H. J. Kang, A. Bist, P. Dua, J. S. Jang, J. S. Lee, *ChemSusChem* **2012**, *5*, 1926.
- [13] S. K. Pilli, T. E. Furtak, L. D. Brown, T. G. Deutsch, J. A. Turner, A. M. Herring, *Energy Environ. Sci.* **2011**, *4*, 5028.
- [14] W. Yao, H. Iwai, J. Ye, *Dalton Trans.* **2008**.
- [15] Y. Park, K. J. McDonald, K.-S. Choi, *Chem. Soc. Rev.* **2013**, *42*, 2321.
- [16] H. Jiang, H. Dai, J. Deng, Y. Liu, L. Zhang, K. Ji, *Solid State Sci.* **2013**, *17*, 21.
- [17] J. A. van Vechten, J. C. Phillips, *Phys. Rev. B* **1970**, *2*, 2160.
- [18] M. Jansen, H. P. Letschert, *Nature* **2000**, *404*, 980.
- [19] B. Modak, S. K. Ghosh, *J. Phys. Chem. C* **2016**, *120*, 6920.
- [20] A. Magneli, *Arkiv for Kemi* **1949**, *1*, 213.
- [21] M. H. Francombe, B. Lewis, *Acta Cryst.* **1958**, *11*, 696.
- [22] J. E. Geusic, H. J. Levinstein, J. J. Rubin, S. Singh, L. G. van Uitert, *Appl. Phys. Lett.* **1967**, *11*, 269.
- [23] C. R. Feger, R. P. Ziebarth, *Chem. Mater.* **1995**, *7*, 373.
- [24] A. Simon, J. Ravez, *Comptes Rendus Chimie* **2006**, *9*, 1268.
- [25] A. J. Paula, R. Parra, M. A. Zaghete, J. A. Varela, *Solid State Com.* **2009**, *149*, 1587.
- [26] A. Perron-Simon, G. Demazeau, J. Ravez, P. Hagenmuller, *Sciences Chimiques* **1975**.
- [27] B. Anke, T. Bredow, J. Soldat, M. Wark, M. Lerch, *J. Solid State Chem.* **2016**, *233*, 282.
- [28] H. Ma, K. Lin, L. Fan, Y. Rong, J. Chen, J. Deng, L. Liu, S. Kawaguchi, K. Kato, X. Xing, *RSC Adv* **2015**, *5*, 71890.
- [29] V. S. Vikhnin, S. E. Kapphahn, V. V. Lemanov, *Ferroelectrics Lett.* **2006**, *28*, 123.
- [30] T. Hajlaoui, M. Josse, C. Harnagea, A. Pignolet, *Mat. Res. Bull.* **2017**, *86*, 30.
- [31] B. Anke, T. Bredow, M. Pilarski, M. Wark, M. Lerch, *J. Solid State Chem.* **2017**, *246*, 75.
- [32] J. D. Bierlein, A. W. Sleight, *Solid State Com.* **1975**, *16*, 69.
- [33] S. Tokunaga, H. Kato, A. Kudo, *Chem. Mater.* **2001**, *13*, 4624.
- [34] Y. Park, K. J. McDonald, K.-S. Choi, *Chem. Soc. Rev.* **2013**, *42*, 2321.

- [35] B. Anke, M. Rohloff, M. G. Willinger, W. Hetaba, A. Fischer, M. Lerch, *Solid State Sci.* **2017**, *63*, 1.
- [36] M. Long, W. Cai, J. Cai, B. Zhou, X. Chai, Y. Wu, *J. Phys. Chem. B* **2006**, *110*, 20211.
- [37] A. W. Sleight, H.-y. Chen, A. Ferretti, D. E. Cox, *Mat. Res. Bull.* **1979**, *14*, 1571.
- [38] W. J. Jo, H. J. Kang, K.-J. Kong, Y. S. Lee, H. Park, Y. Lee, T. Buonassisi, K. K. Gleason, J. S. Lee, *Proc. Natl. Acad. Sci. U.S.A.* **2015**, *112*, 13774.
- [39] A. Kudo, K. Omori, H. Kato, *J. Am. Chem. Soc.* **1999**, *121*, 11459.
- [40] W. J. Jo, J.-W. Jang, K.-J. Kong, H. J. Kang, J. Y. Kim, H. Jun, K. P. S. Parmar, J. S. Lee, *Angew. Chem. Int. Ed. Engl.* **2012**, *51*, 3147.
- [41] H. Ye, J. Lee, J. S. Jang, A. J. Bard, *J. Phys. Chem. C* **2010**, *114*, 13322.
- [42] W. Luo, J. Wang, X. Zhao, Z. Zhao, Z. Li, Z. Zou, *Phys. Chem. Chem. Phys.* **2013**, *15*, 1006.
- [43] W. Luo, Z. Li, T. Yu, Z. Zou, *J. Phys. Chem. C* **2012**, *116*, 5076.
- [44] R. Allmann, *Röntgen-Pulverdiffraktometrie: Rechnergestützte Auswertung, Phasenanalyse und Strukturbestimmung*, Springer Berlin Heidelberg, Berlin, Heidelberg **2003**.
- [45] E. Prince, H. Fuess, T. Hahn, H. Wondratschek, U. Müller, U. Shmueli, A. Authier, V. Kopský, D. B. Litvin, M. G. Rossmann, E. Arnold, S. Hall, B. McMahon, *International Tables for Crystallography*, International Union of Crystallography, Chester, England **2006**.
- [46] J. Rodríguez-Carvajal, *Phys. B: Cond. Mat.* **1993**, *192*, 55.
- [47] G. Will, *Powder diffraction: The Rietveld method and the two-stage method to determine and refine crystal structures from powder diffraction data*, Springer, Berlin, New York **2006**.
- [48] A. M. Huizar-Félix, T. Hernández, S. de La Parra, J. Ibarra, B. Kharisov, *Powder Tec.* **2012**, *229*, 290.
- [49] L. Smart, E. Moore, *Einführung in die Festkörperchemie*, Vieweg, Braunschweig, Wiesbaden **1997**.
- [50] W. Massa, *Kristallstrukturbestimmung*, B.G. Teubner Verlag / GWV Fachverlage GmbH, Wiesbaden, Wiesbaden **2007**.
- [51] P. Paufler, *Cryst. Res. Technol.* **1994**, *29*, 808.
- [52] W. H. Bragg, W. L. Bragg, *Proc. Camb. Phil. Soc.* **1913**, *88*, 428.
- [53] J. C. M. Brentano, *Proc. Phys. Soc.* **1937**, *49*, 61.
- [54] *Instruction Manual, TC-300* **1998**.
- [55] P. Kubelka, F. Munk, *Z. Tech. Phys* **1931**, *12*, 593.
- [56] R. Marschall, J. Soldat, G. W. Busser, M. Wark, *Photochem. Photobiol. Sci.* **2013**, *12*, 671.
- [57] Y. Ma, F. Le Formal, A. Kafizas, S. R. Pendlebury, J. R. Durrant, *J. Mater. Chem. A Mater. Energy Sustain.* **2015**, *3*, 20649.

Part II.

Results and Discussion

4. Publication 1

Synthesis, crystal structure, and photocatalytical properties of $\text{Ba}_3\text{Ta}_5\text{O}_{14}\text{N}$

B. Anke, T. Bredow, J. Soldat, M. Wark, M. Lerch

published

Journal of Solid State Chemistry 233 (2016) 282–288

doi: 10.1016/j.jssc.2015.10.042

<https://doi.org/10.1016/j.jssc.2015.10.042>

Contribution to publication:

B. Anke: Sample preparation, chemical analysis and crystal structure analysis, UV-Vis interpretation, and writing.

T. Bredow: Quantum-chemical calculations.

J. Soldat: Measurements (photocatalysis), evaluation.

M. Wark: General discussion, proofreading.

M. Lerch: General advice and helpful comments, proofreading

Authors: *B. Anke*,¹ *T. Bredow*,² *J. Soldat*,^{3,4} *M. Wark*,⁴ *M. Lerch**¹

¹Institut für Chemie, Technische Universität Berlin,
Straße des 17. Juni 135, 10623 Berlin

² Mulliken Center for Theoretical Chemistry, Institut für Physikalische und
Theoretische Chemie, Universität Bonn, Beringstr. 4, 53115 Bonn

³ Lehrstuhl für Technische Chemie, Ruhr-Universität Bochum, Universitätsstr. 150,
44801 Bochum

⁴ Institut für Chemie, Carl von Ossietzky Universität Oldenburg,
Carl-von-Ossietzky-Str. 9-11, 26129 Oldenburg

*corresponding author

Keywords: barium tantalum oxide, oxide nitrides, synthesis, crystal structure, quantum-chemical calculations, photocatalysis

4.1. Abstract

Light yellow $\text{Ba}_3\text{Ta}^{\text{V}}\text{O}_{14}\text{N}$ was successfully synthesized as phase-pure material crystallizing isostructurally to well-known mixed-valence $\text{Ba}_3\text{Ta}^{\text{V}}_4\text{Ta}^{\text{IV}}\text{O}_{15}$. The electronic structure of $\text{Ba}_3\text{Ta}_5\text{O}_{14}\text{N}$ was studied theoretically with a hybrid Hartree–Fock-DFT method. The most stable structure was obtained when nitrogen atoms were placed at $4h$ sites having fourfold coordination. By incorporating nitrogen, the band gap decreases from ~ 3.8 eV commonly known for barium tantalum(V) oxides to 2.8 eV for the oxide nitride, giving rise to an absorption band well in the visible-light region. $\text{Ba}_3\text{Ta}_5\text{O}_{14}\text{N}$ was also tested for photocatalytic hydrogen formation.

4.2. Introduction

Taking a look on ternary barium tantalum oxides reported in literature, a variety of phases with different compositions is reported: BaTa_2O_6 , [1] $\text{Ba}_2\text{Ta}_5\text{O}_{32}$, [2] $\text{Ba}_5\text{Ta}_4\text{O}_{15}$, [3] and $\text{Ba}_4\text{Ta}_2\text{O}_9$ [4] have been already described. It is worth mentioning that also two mixed-valent compounds, $\text{Ba}_{1.88}\text{Ta}_{15}\text{O}_{32}$ [5] and $\text{Ba}_3\text{Ta}_5\text{O}_{15}$, [6] are known. Interestingly, remarkable photocatalytic activity (water splitting, H_2 -evolution) is observed for $\text{Ba}_3\text{Ta}^{\text{V}}_4\text{Ta}^{\text{IV}}\text{O}_{15}$ -containing composites. [7] $\text{Ba}_3\text{Ta}_5\text{O}_{15}$ exhibits the well-known tetragonal tungsten bronze structure (space group $P4/mbm$ [6]) and can be described as vertex-sharing framework of TaO_6 -octahedra forming huge sites where larger metal cations are located.

Photocatalytic activity under visible light ($420 \text{ nm} < \lambda < 800 \text{ nm}$) requires optical band gaps of $E_g < 2.9$ eV. Barium tantalum oxides typically have values above 3.5 eV. A common strategy to narrow the optical band gap in oxides is the partial substitution of oxygen by aliovalent anions. In 2001, Asahi *et al.* predicted a reduction of the band gap of titania maintaining the conduction band (CB) minimum level and shifting the valence band (VB) maximum to a position with more negative potential. [8] Their studies initiated a lot of efforts in investigating anion substitution in photocatalysts using a number of ‘dopant elements’ such as B [9–11], C [12–16], F [17–21], N [22–26], P [12], or S [27–30] to narrow optical band gaps to the visible-light region for various semiconductor materials. Among these, nitrogen has been reported to be the most

effective dopant so far. Also several visible light-driven semiconductors containing photocatalysts including tantalum oxide nitrides are known to perform photocatalytic water splitting.[31–33] In the present contribution, we report on synthesis, crystal structure incl. N/O distribution, optical properties, and photocatalytic activity of the new compound $\text{Ba}_3\text{Ta}^{\text{V}}_5\text{O}_{14}\text{N}$ formally derived from $\text{Ba}_3\text{Ta}^{\text{V}}_4\text{Ta}^{\text{IV}}\text{O}_{15}$ by substituting one oxygen by nitrogen combined with an oxidation of Ta^{IV} to Ta^{V} . It should be mentioned that first attempts preparing such an oxide nitride phase have been carried out by Assabaa-Boultif [34] but never been published in a regular journal.

4.3. Experimental Section

4.3.1. Synthesis

An amorphous ternary Ba-Ta-O phase was synthesized via the sol-gel based Pechini route.[35] Citrate complexes of tantalum and barium were prepared. For the barium citrate solution barium chloride powder (Sigma Aldrich, 99.9 %) was dissolved in an ethanol/water mixture containing citric acid (Sigma Aldrich 99.5 %). Citric acid was used in a molar excess of 12 times the BaCl_2 . Tantalum citrate solution was prepared using tantalum(V) chloride powder (Sigma Aldrich, 99.999 %) by dissolving it in ethanol containing citric acid as well. Both solutions were mixed in a molar ratio of 3:5 with ethylene glycol and polymerized at 200 °C in a batch furnace. After calcination at 400 °C, an amorphous oxide was obtained. This precursor was treated with a mixture of NH_3 and O_2 at 850 °C for 24 h in a tube furnace with flow rates of $10 \text{ L} \cdot \text{h}^{-1}$ and $0.03 \text{ L} \cdot \text{h}^{-1}$ for ammonia and oxygen, respectively.

4.3.2. Chemical and structural characterization

The products were characterized by X-ray powder diffraction using a PANalytical X'Pert PRO diffractometer (Bragg-Brentano geometry, Cu-K α radiation). All structural refinements were performed with the program *FullProf Suite* Version 2009, by applying a pseudo-Voigt function for the microstructural analysis.[36] Nitrogen and oxygen contents were determined by hot gas extraction method (LECO TC-300/EF-300), for calibration ZrO_2 and steel (LECO calibration sample, N: 5000 ppm) were used as standard materials. The accuracy is $\sim 2 \%$ of the presented N/O content. X-ray

fluorescence spectrometry (XRF) was performed using a PANalytical Axios spectrometer with an Rh-tube.

4.3.3. UV-vis spectroscopy

UV-Vis diffuse reflectance spectra were measured using a Perkin Elmer Lambda 650 UV-Vis spectrometer equipped with a Praying-Mantis mirror construction. The obtained spectra were converted by the Kubelka-Munk function $F(R)$ into absorption spectra, using MgO nanopowder as a white standard. Optical band gaps (E_g) were obtained via the Tauc plot method [30,37–41] using the calculation $\alpha = A(h\nu - E_g)^n/h\nu$, where α is the absorption coefficient, A is a constant, $h\nu$ is the energy of light, and $n = 2$ is valid for materials with indirect band gap transition, respectively. Assuming the absorption coefficient α being proportional to the Kubelka-Munk function $F(R)$, E_g can be obtained from the plot of $[F(R)h\nu]^{1/n}$ versus $h\nu$, by extrapolation of the linear part near the onset of the absorption edge to intersect the energy axis.

4.3.4. Quantum-chemical methods

The effect of O/N distribution on the stability and electronic structure of $Ba_3Ta_5O_{14}N$ was calculated from first principles employing hybrid density functional theory (DFT) methods implemented in the crystalline-orbital program CRYSTAL14.[42] Similar to our previous studies on TaON[43] the method PW1PW[44] was employed for the structure optimizations. For the structure optimizations standard basis sets (std) from the CRYSTAL homepage were used.[45] For the calculation of the electronic structure we employed the recently developed hybrid method HSE06 with screened exchange[46] which was demonstrated to provide improved band gaps of oxides. Since also the atomic basis set affects the band positions, we switched from standard to extended basis sets of triple-zeta valence plus polarization (tzvp) quality. For O and N, we employed the pob basis sets,[47] and for Ta and Ba Stuttgart/Dresden effective core potentials plus modified triple-zeta basis sets[48,49] where diffuse functions were removed.

4.3.5. Photocatalysis

Photocatalytic hydrogen generation was measured in a home-made air-free closed gas system using a double-walled inner irradiation-type quartz reactor. As a light source, a 700 W Hg mid-pressure immersion lamp (Peschl UV-Consulting, set to a power of 500 W) was used for irradiation and cooled with a double-walled quartz mantle using a thermostat (LAUDA). Gas evolution was detected online using a multi-channel analyzer (Emerson) equipped with a detector for the determination of the concentration of hydrogen (thermal conductivity detector), oxygen (paramagnetism) and carbon dioxide (IR). Argon was used as carrier gas, the continuous gas flow was controlled by a Brockhorst mass flow controller. The gas flow was set to 50 NmL/min (normal flow throughput: gas flow at ambient temperature and pressure per minute).

All reactions were performed at 13 °C. 300 mg of photocatalyst is suspended in 550 mL water and 50 mL methanol (aqueous methanol photoreforming). For a homogeneous suspension a subsequent pre-treatment in the ultrasonication bath for 10 minutes at 30 °C was performed. Before any photocatalytic reaction was initiated, the whole system including the photocatalyst was flushed with argon at 100 NmL/min for 30 minutes to remove any trace of air. In previous measurements Rh was obtained as the most effective co-catalyst for barium tantalates with an optimum loading of only 0.0125 wt.-%. Rh [7,50] nanoparticles were deposited onto the photocatalyst materials via reductive photodeposition with a specific amount of Na₃RhCl₆ (99.999%, Aldrich) precursor solution using the setup described below. For measurements under visible light an aqueous 2 M NaNO₂ solution was used as filter.

4.4. Results and discussion

4.4.1. Chemical analysis and crystal structure

We successfully synthesized light yellow Ba₃Ta₅O₁₄N as phase-pure material: XRF analysis proved the Ba/Ta content of 26 wt% Ba and 58 wt% Ta (expected: 26.5 wt% Ba, 58.1 wt% Ta). Quantitative chemical analysis by hot gas extraction delivered the following values: 15.0 wt% O, 0.9 wt% N (expected: 14.4 wt% O, 0.9 wt% N).

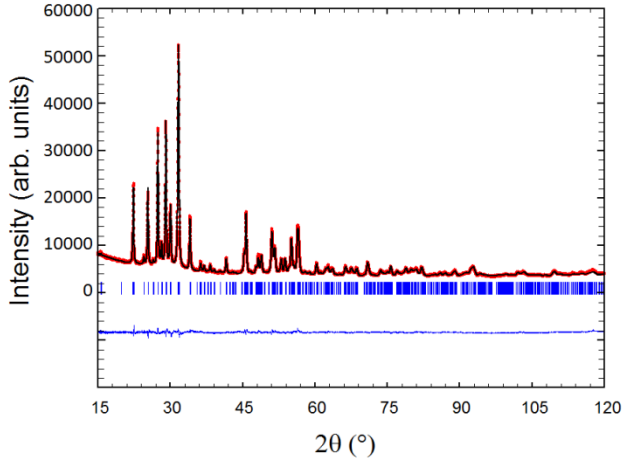


Figure 4.1: X-ray powder diffraction pattern of $\text{Ba}_3\text{Ta}_5\text{O}_{14}\text{N}$ with the results of the Rietveld refinement.

The structural refinement of $\text{Ba}_3\text{Ta}_5\text{O}_{14}\text{N}$ was started from the coordinates reported for $\text{Ba}_3\text{Ta}_5\text{O}_{15}$. [6] Figure 4.1 depicts the X-ray powder diffractogram of the new phase $\text{Ba}_3\text{Ta}_5\text{O}_{14}\text{N}$ with the results of the Rietveld refinement. Further structural parameters are listed in Table 4.1 with a comparison to $\text{Ba}_3\text{Ta}_5\text{O}_{15}$. Atomic coordinates and isotropic Debye-Waller factors are presented in Table 4.2. For comparison, we also prepared $\text{Ba}_3\text{Ta}_5\text{O}_{15}$, following the work of Feger and Ziebarth. [6] The refined structural parameters are in good agreement. Finally, we decided to use the parameters from literature for discussion because of the higher quality of the single crystal data.

Table 4.1: Refined structural parameters of $\text{Ba}_3\text{Ta}_5\text{O}_{14}\text{N}$ in comparison to $\text{Ba}_3\text{Ta}_5\text{O}_{15}$

Composition	$\text{Ba}_3\text{Ta}_5\text{O}_{14}\text{N}$	$\text{Ba}_3\text{Ta}_5\text{O}_{15}$ [6]
Measure	powder diffraction	single crystal
Crystal system	tetragonal	
Space group	$P4/mbm$	
Formular units	$Z=2$	
Lattice parameters	$a = 12.6461(9) \text{ \AA}$ $c = 3.9667(5) \text{ \AA}$	$a = 12.590(1) \text{ \AA}$ $c = 3.967(2) \text{ \AA}$
Unit cell volume	$V = 634.38(9) \text{ \AA}^3$	$V = 628.8(4) \text{ \AA}^3$
Calc. density	8.1387 g/cm^3	8.2214 g/cm^3
R_{wp}	0.0175	
R_{Bragg}	0.0288	
R_{exp}	0.0076	
S	2.3	

Table 4.2: Atomic positional parameters and isotropic Debye-Waller factors for Ba₃Ta₅O₁₄N.

	Wyckoff	<i>x</i>	<i>y</i>	<i>z</i>	<i>B</i> _{iso}
Ba(1)	2 <i>a</i>	0	0	0	2.1(2)
Ba(2)	4 <i>g</i>	0.1720(4)	0.6719(4)	0	2.7(2)
Ta(1)	2 <i>c</i>	0	½	½	1.9(2)
Ta(2)	8 <i>j</i>	0.0755(3)	0.2141(3)	½	1.84(14)
O/N(1)	2 <i>d</i>	0	½	0	1
O/N(2)	4 <i>h</i>	0.281(3)	0.781(3)	½	1
O/N(3)	8 <i>i</i>	0.069(4)	0.209(3)	0	1
O/N(4)	8 <i>j</i>	0.491(2)	0.157(4)	½	1
O/N(5)	8 <i>j</i>	0.136(3)	0.071(4)	½	1

Ba₃Ta₅O₁₄N crystallizes in the tetragonal tungsten bronze-type structure in space group *P4/mbm*; the unit cell dimensions are $a = 12.6461(9) \text{ \AA}$, $c = 3.9667(5) \text{ \AA}$. Figure 4.2 shows a schematic representation of the unit cell. All tantalum atoms are octahedrally coordinated by oxygen and/or nitrogen. These octahedra share all corners with neighboring octahedra resulting in 3-, 4- and 5-fold cavities in a ratio of 2:1:2 (see Figure 4.2). Only the 4- and 5-fold cavities offer the huge Ba-cations sufficient space. Details about the determined bond lengths are given in Figure 4.3. Ba(1) in the 4-fold cavities is cubeoctahedrally coordinated by twelve anions, Ba(2) in the 5-fold cavities is, in the most simple view (see Fig. 4.3), surrounded by six anions forming a trigonal prisma. It should be mentioned that there is an anion O/N1 3.08 Å away from Ba(2), leading to a monocapped trigonal prisma if respected. Eight additional anions are located between 3.3 and 3.4 Å around Ba(2) which are not discussed here. For a detailed presentation of this detail see the work of Feger and Ziebarth.[6]

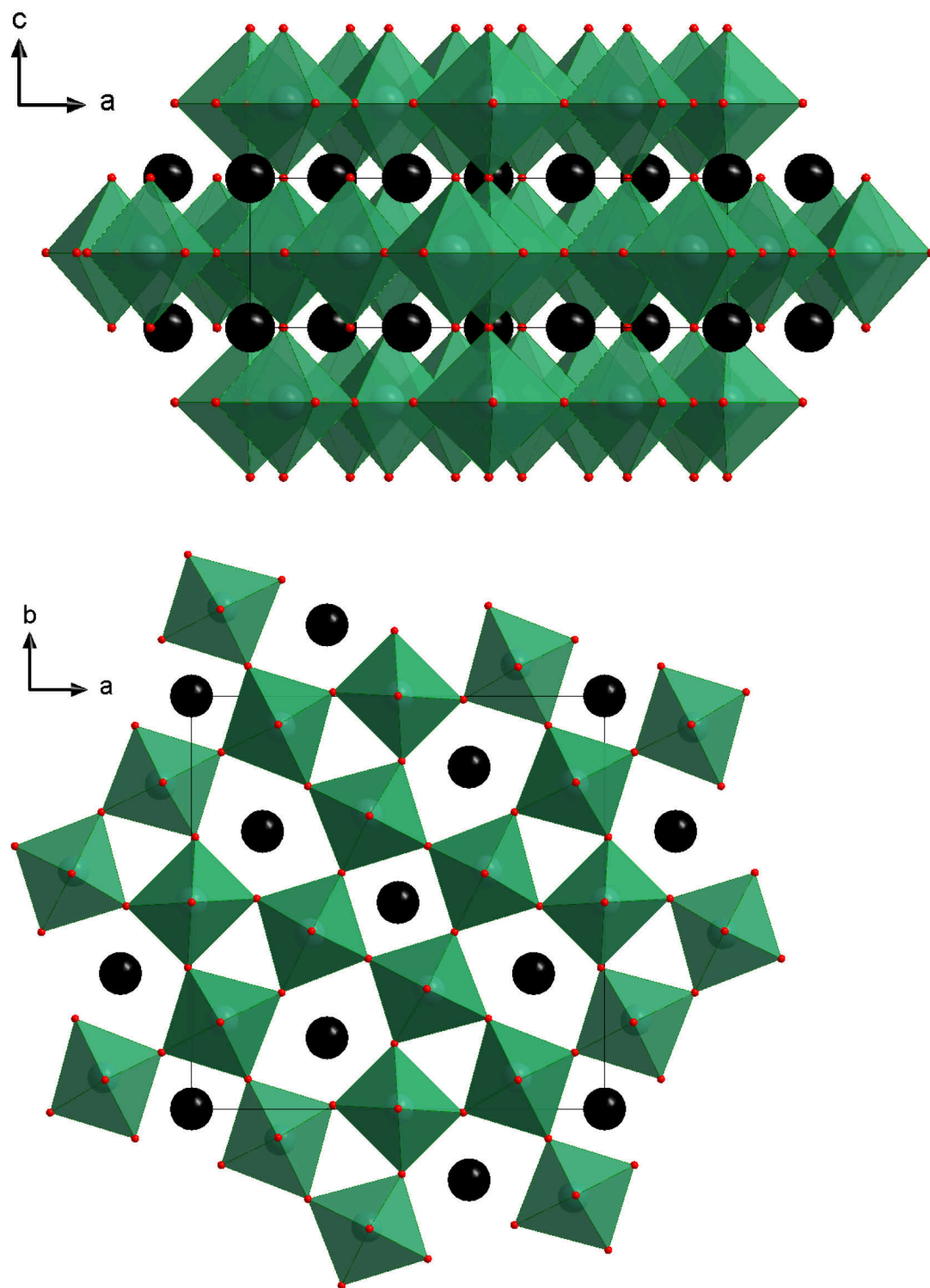


Figure 4.2: Unit cell of $\text{Ba}_3\text{Ta}_5\text{O}_{14}\text{N}$ and polyhedral representation of the crystal structure. $\text{Ta}(\text{O}/\text{N})_6$ octahedra are drawn in green; Ba atoms are represented by black balls.

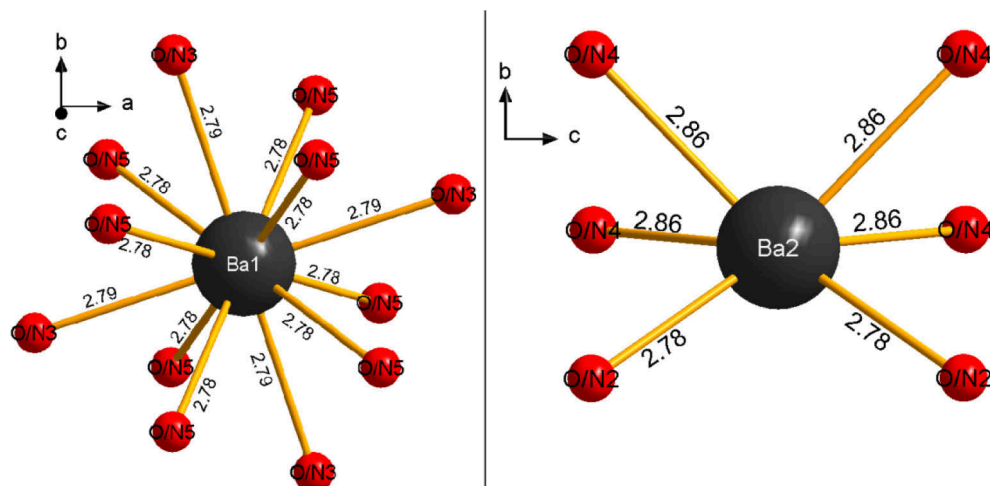


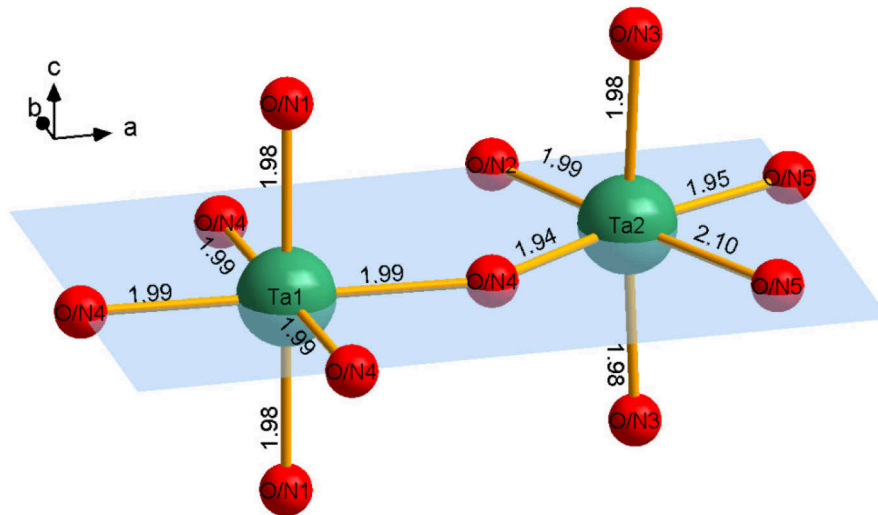
Figure 4.3: Ba-O/N polyhedra in $\text{Ba}_3\text{Ta}_5\text{O}_{14}\text{N}$ with the determined bond lengths (Å).

One of the two crystallographically independent $\text{Ta}(\text{O}/\text{N})_6$ polyhedra ($\text{Ta}(2)$) is more distorted, with Ta-O/N distances varying from 1.941 Å to 2.108 Å, compared to 1.983 Å and 1.999 Å for $\text{Ta}(1)$ (Figure 4.4). The average bond lengths are 1.995 Å for $\text{Ta}1$ -(O/N) and 1.996 Å for $\text{Ta}2$ -(O/N) being increased by about 0.017 Å ($\text{Ta}1$ -(O/N)) and 0.009 Å ($\text{Ta}2$ -(O/N)) compared to pure oxide $\text{Ba}_3\text{Ta}_5\text{O}_{15}$. [6]

In comparison to $\text{Ba}_3\text{Ta}_5\text{O}_{15}$ the oxide nitride $\text{Ba}_3\text{Ta}_5\text{O}_{14}\text{N}$ exhibits a slightly larger cell volume. This could be due to the 8 pm larger radius of nitrogen (4-fold coordination) compared to oxygen (difference between Ta^{5+} and Ta^{4+} (C.N. = 6) = 4 pm [51]). It should be mentioned that only the bond lengths in the a - b -plane increase significantly (Table 4.3, Figure 4.4), which is also reflected in an increase of the lattice parameter a (c remains constant). Consequently, it can be assumed that the nitrogen atoms are mainly located in the a - b -plane (on O/N2, O/N4, and O/N5 positions). This fits well with Pauling's 2nd rule predicting nitrogen on anion positions with high coordination numbers: O/N1 = 2, O/N2 = 4, O/N3 = 3, O/N4 = 4, O/N5 = 4, as it has also been generally described in the work by Fuertes. [52]

Table 4.3: Determined Ba/Ta-O/N bond lengths in $\text{Ba}_3\text{Ta}_5\text{O}_{14}\text{N}$ and $\text{Ba}_3\text{Ta}_5\text{O}_{15}$.

bonds	$\text{Ba}_3\text{Ta}_5\text{O}_{14}\text{N}$ bond lengths /Å	$\text{Ba}_3\text{Ta}_5\text{O}_{15}$ bond lengths /Å[6]	difference / Å
Ta1- O/N1	1.9834(2)	1.9835	- 0.0001
Ta1- O/N4	1.998(7)	1.9733	+ 0.025
Ta2- O/N3	1.9856(5)	1.9841	+ 0.0015
Ta2- O/N2	1.997(9)	1.9857	+ 0.011
Ta2- O/N4	1.940(9)	1.9271	+ 0.013
Ta2- O/N5	1.955(12)	2.0120	- 0.057
Ta2- O/N5	2.108(9)	2.0319	+ 0.076
Ba1-O/N5	2.782(8)	2.8045	- 0.023
Ba1-O/N3	2.792(9)	2.8260	- 0.034
Ba2-O/N2	2.788(6)	2.8031	- 0.015
Ba2-O/N4	2.866(5)	2.8730	- 0.007

Figure 4.4: $\text{Ta}(\text{O}/\text{N})_6$ octahedra in $\text{Ba}_3\text{Ta}_5\text{O}_{14}\text{N}$ with the determined bond lengths(Å).

4.4.2. Optical properties

The yellow colored material $\text{Ba}_3\text{Ta}_5\text{O}_{14}\text{N}$ was measured in diffuse reflectance geometry which is converted into Tauc plots in order to estimate the optical band gap. Although the exact band gap of $\text{Ba}_3\text{Ta}_5\text{O}_{15}$ is not known yet, all pristine barium tantalum(V) oxides offer wide band gaps in a range between 3.8 – 4.7 eV [50] which allow only light absorption in the UV region. For $\text{Ba}_3\text{Ta}_5\text{O}_{14}\text{N}$ Figure 4.5 indicates a successful decrease in the band gap to about 2.8 eV. Thus, the electronic structure could be specifically modified and allows now in principle a partial absorption of the visible light in the solar

spectrum, increasing the amount of useable solar light energy from about 4 % (for only UV light absorption) to about 10 %.

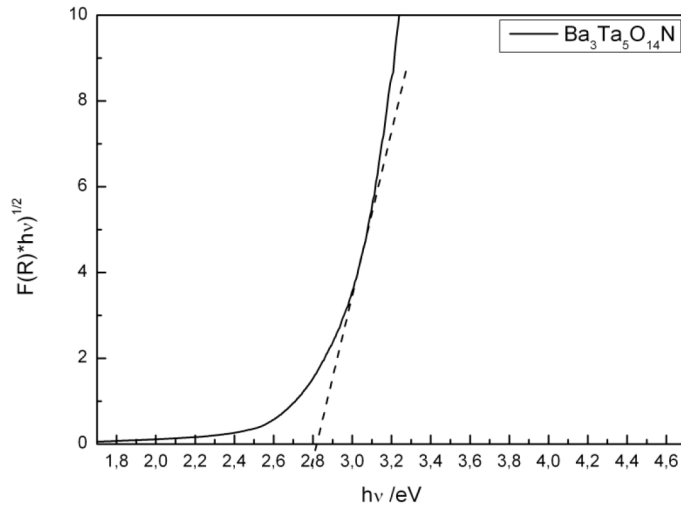


Figure 4.5: Tauc plot of $\text{Ba}_3\text{Ta}_5\text{O}_{14}\text{N}$ based on diffuse reflectance geometry.

4.4.3. Quantum-chemical calculations

As a preliminary step for the theoretical investigation of the electronic structure of $\text{Ba}_3\text{Ta}_5\text{O}_{14}\text{N}$ structure optimizations were performed with the PW1PW hybrid method. In these optimizations the lattice parameters were kept fixed at the experimental values determined in this study (see Table 4.1) and the positions of all atoms were relaxed. Five O/N configurations were considered where two nitrogen atoms were placed at sites O/N(1) to O/N(5) in the primitive cell, see Table 4.2. All other sites are occupied with oxygen. In case of Wyckoff positions 4h, 8i and 8j several arrangements of the two N atoms are possible. In this first step of the determination of N-site stability only one configuration was arbitrarily selected for each case. The relative stabilities shown in Table 4.4 are in line with the above considerations based on Pauling's 2nd rule. The most stable N site is O/N(2) with a four-fold coordination. The two-fold coordinated O/N(1) site is less stable. The energy differences between the five Wyckoff sites, 0.52-2.10 eV, are so large that under thermodynamic control only the 4h site should be occupied with nitrogen. For this site two other distributions of 2 N over 4 sites were considered, denoted as (2b) and (2c). Energetically they do not differ significantly (by less than 0.05 eV). Since zero point energy and vibrational contributions to the enthalpy were neglected, it is not possible to distinguish between structures (2), (2b) and (2c).

Table 4.4: Relative stability (eV) of different O/N configurations of $\text{Ba}_3\text{Ta}_5\text{O}_{14}\text{N}$; two nitrogen atoms are placed at particular lattice sites, and all other sites are occupied by oxygen. Comparison of two hybrid DFT functionals and basis sets, see text.

N on lattice site	PW1PW/std	HSE06/tzvp
O/N(1)	2.10	2.10
O/N(2)	0.00	0.00
(2b)	0.00	0.01
(2c)	0.05	0.05
O/N(3)	1.51	1.51
O/N(4)	0.70	0.71
O/N(5)	0.52	0.53

The optimized N-Ta and N-Ba distances are presented in Table 4.5. They are quite similar to the averaged values for O/N, see Table 4.3. After optimization, the configuration where N occupies two O/N(3) sites changes the coordination number from three to four (with a slightly larger N-Ba distance of 2.90 Å compare to the other configurations). In the most stable configuration the nitrogen coordination is rather symmetric with two identical N-Ta and N-Ba distances of 1.92 Å and 2.80 Å, respectively. Configurations with N on sites (3), (4), and (5) are less stable than with N on (2) because they also contain a relatively small N-O distance (in the range 2.6-2.7 Å) which leads to repulsive interactions. Trivalent nitrogen is unstable on the two-coordinated site in (1) as discussed above.

Table 4.5: Optimized nearest-neighbor distances around the N atoms (Å) obtained for five configurations. Results obtained with PW1PW/std.

N on lattice site	Distances to Ta	Distances to Ba
O/N(1)	1.98, 1.98	>3
O/N(2)	1.92, 1.92	2.80, 2.80
O/N(3)	2.00, 2.00	2.77, 2.90
O/N(4)	1.84, 2.01	2.82, 2.82
O/N(5)	1.94, 1.97	2.82, 2.82

In order to check the method and basis set dependence of the calculated electronic structure we compared the PW1PW/std results with the screened-exchange hybrid method HSE06, combined with extended pob basis sets. The HSE06/pob band structure calculations were performed for the structures optimized with PW1PW/std. It has to be mentioned that the relative stabilities of the O/N configurations obtained with the two theoretical approaches almost perfectly agree, see Table 4.4. The calculated direct and indirect band gaps are presented in Table 4.6.

Table 4.6: Calculated electronic band gaps of the considered O/N configurations (eV). Comparison of PW1PW/std and HSE06/tzvp.

N site	PW1PW/std		HSE06/tzvp	
	Direct	Indirect	Direct	Indirect
O/N(1)	1.68	1.61	1.47	1.39
O/N(2)	4.37	3.51	4.07	3.17
(2a)	4.39	3.53	4.07	3.17
(2b)	4.38	3.32	4.06	2.98
O/N(3)	2.24	2.20	1.92	1.51
O/N(4)	3.60	2.96	3.31	2.62
O/N(5)	3.71	3.10	3.34	2.74

Irrespective of the O/N distribution $\text{Ba}_3\text{Ta}_5\text{O}_{14}\text{N}$ has an indirect electronic band gap, which might also be the reason for the quite pronounced absorption onset in Figure 4.5. In the most stable configurations with N on the 4h site the difference between direct and indirect transition is rather pronounced, ~ 0.9 eV. Also the effect of the N position in the lattice on the calculated gap is large. The least stable configuration has the smallest band gap, 1.39 eV, and the most stable structures have the largest gaps, 2.98-3.17 eV. In general the band gaps obtained with the HSE06/tzvp method are smaller (by 0.2-0.4 eV) than those obtained with PW1PW/std. Since they are closer to the experimental values, only the HSE06 results will be discussed here. However, it should be kept in mind that due to excitonic effects optical gaps are generally smaller than electronic gaps. A quantitative determination of optical excitation energies would require much more sophisticated methods such as Green function techniques combined with Bethe-Salpeter equation (for a recent application see [53]). Unfortunately the present system is too large to be treated at this level with the present computer resources. Therefore it is not surprising that the calculated indirect band gaps for the most stable structures (2), (2b), (2c) are 0.2-0.4 eV larger than the measured optical gap of 2.8 eV (*vide supra*). Nevertheless the error is in the typical range for hybrid DFT methods. The calculated band gaps allow for a clear distinction between the possible O/N distributions, independent from the energy calculations. The reason for the significantly reduced band gap for structure (1) is shown in Figure 4.6.

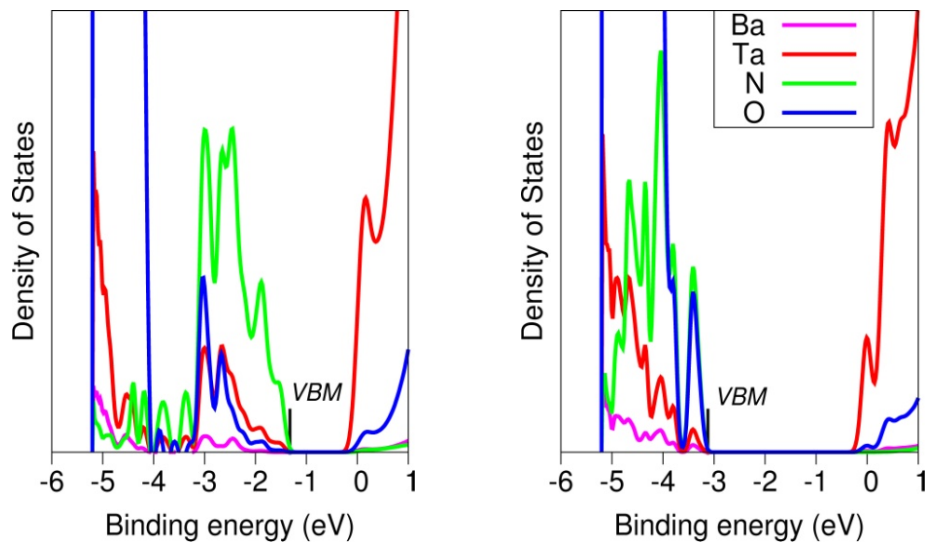


Figure 4.6: Projected density of states for configurations (1), left, and (2), right. For clarity the zero point of energy was shifted to the bottom of the conduction band. (VBM: valence band maximum)

The lone pairs of the two-fold coordinated nitrogen (structure (1), left side of Figure 4.6) form broad bands between -1.4 eV and -3.1 eV. This leads to the extremely small band gap. If nitrogen is four-fold coordinated (structure (2), right side of Figure 4.6) the sp^3 hybrid orbitals are lowered in energy due to bonding with Ta and Ba atoms. Consequently their bands are down shifted towards the oxygen valence band. The highest bands have contributions from both N 2sp and O 2sp orbitals. They are therefore less localized on nitrogen atoms than the highest bands in other oxide nitrides, e.g. Ta_3O_6N which is expected to lead to a slower recombination of electron-hole pairs after photo-excitation. For comparison we also calculated the undoped oxide $Ba_3Ta_5O_{15}$ with the same computational approach as described above. The lattice parameters and atom positions were taken from ref. [6]. We performed two sets of band structure calculations, with fixed atomic positions and after full relaxation where only the lattice parameters were kept to their measured values. No significant changes of the band positions were observed. As expected for a system containing partially reduced Ta ions, $Ba_3Ta_5O_{15}$ has a metallic character due to occupied Ta 5d orbitals at the Fermi energy which is located at the bottom of the CB. This is in accordance with the observed blue-black color. However, the fundamental band gap between the O 2p dominated VB and the CB is 3.92 eV, similar as reported above for stoichiometric oxides.

4.4.4. Photocatalysis

The resulted optimized material $\text{Ba}_3\text{Ta}_5\text{O}_{14}\text{N}$ has been used in photocatalytic test reactions for hydrogen formation. 300 mg of catalyst is suspended in 600 mL aqueous solution containing 50 mL methanol for aqueous photoreforming. The suspension was irradiated with a 500 W mid-pressure Hg lamp in an irradiation type reactor connected to a home-made closed gas system. Figure 4.7 shows the hydrogen evolution rates of $\text{Ba}_3\text{Ta}_5\text{O}_{14}\text{N}$ before and after reductive *in situ* photodeposition of 0.0125 wt.-% Rh which was determined in prior studies as an optimal co-catalyst loading for barium tantalate materials.[50] The hydrogen generation already in absence of any co-catalyst clearly points out that the nitrated form of $\text{Ba}_3\text{Ta}_5\text{O}_{15}$ exhibits active surface sites for H_2 generation. After deposition of the very small amount of Rh nanoparticles the evolution rate increases up to 115 $\mu\text{mol/h}$ of H_2 . Rh acts as a typical co-catalyst withdrawing electrons from the photocatalyst for efficient charge carrier separation and has the function of an active center for proton reduction and hydrogen generation. Thus, the total H_2 production could be improved and resulted in an about 20 % higher H_2 evolution rate. Compared to other photocatalytic systems, e.g. [33], the effect of the co-catalyst is relatively low confirming that the hydrogen evolution sites on $\text{Ba}_3\text{Ta}_5\text{O}_{14}\text{N}$ are already quite active. High activity without co-catalyst was also observed for nanocomposites of barium tantalates.[49]

Since in photocatalytic studies with other oxide nitrides, e.g. [31-33], different equipment and procedures were used and thus parameters, such as reactor design, irradiation source, quantity and kind of co-catalyst, all playing important roles for photocatalytic activities are different, it is to our opinion not helpful to attempt non-realistic comparisons of H_2 evolution rates.

In test reactions regarding hydrogen generation under simulated visible light in the presence of 2 M NaNO_2 solution as an optical filter no significant activity could be observed with the prepared $\text{Ba}_3\text{Ta}_5\text{O}_{14}\text{N}$. Since the photocatalytic tests are performed with an immersion lamp only fluid filters can be used. NaNO_2 completely blocks light with energies > 3.05 eV, thus the effective absorption window for $\text{Ba}_3\text{Ta}_5\text{O}_{14}\text{N}$ to induce photocatalytic activity is low. Therefore, barium tantalum oxide nitrides with stronger band gap shifts will be required. However, because also with UV light, the H_2 formation rate with $\text{Ba}_3\text{Ta}_5\text{O}_{14}\text{N}$ photocatalyst is lower than with $\text{Ba}_5\text{Ta}_4\text{O}_{15}$ or

$\text{Ba}_3\text{Ta}_5\text{O}_{15}$ containing nanocomposites [7], also the presence of defects in the lattice acting as unwanted recombination centers cannot be ruled out. Deeper investigations to decrease the probability of increased recombination of electron-hole pairs and to enhance the photocatalytic activity are still ongoing. Nevertheless the present results provide a proficient basis for a route to photoactive materials active under visible light.

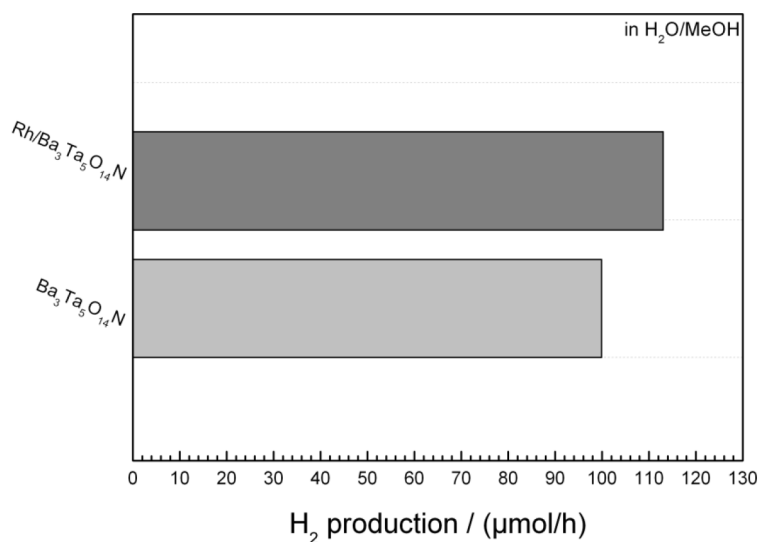


Figure 4.7: Photocatalytic hydrogen evolution rates of $\text{Ba}_3\text{Ta}_5\text{O}_{14}\text{N}$ before and after reductive *in situ* photodeposition of 0.0125 wt.-% Rh.

4.5. Conclusion

We were successful in synthesizing light yellow $\text{Ba}_3\text{Ta}_5\text{O}_{14}\text{N}$ (tantalum(V) only) with an optical band gap of ~ 2.8 eV as pure-phase material by an ammonolysis reaction. The oxide nitride crystallizes isostructurally to the known mixed-valence oxide $\text{Ba}_3\text{Ta}_4^{\text{V}}\text{Ta}^{\text{IV}}\text{O}_{15}$. Quantum chemical calculations at hybrid DFT level provide band gaps of 2.98-3.17 eV, close to the measured value. The effect of N/O distribution on the optical properties was calculated to be very pronounced. First measurements of the photocatalytic activity exhibited significant but not outstanding performance. In a next step, a further narrowing of the band gap using co-doping concepts seems to be promising. Keep in mind that an increase of the nitrogen content should result in a decrease of the band gap. One strategy may be the co-substitution $\text{Ba}^{2+}/\text{O}^{2-} \rightarrow \text{La}^{3+}/\text{N}^{3-}$: $\text{Ba}_3\text{Ta}_5\text{O}_{15} \rightarrow \text{Ba}_3\text{Ta}_5\text{O}_{14}\text{N} \rightarrow \text{LaBa}_2\text{Ta}_5\text{O}_{13}\text{N}_2 \rightarrow \text{La}_2\text{BaTa}_5\text{O}_{12}\text{N}_3 \rightarrow \text{La}_3\text{Ta}_5\text{O}_{11}\text{N}_4$.

Acknowledgment

The authors would like to thank M. Stöbe (TU Berlin) for performing XRF analyses. This work is supported by the Deutsche Forschungsgemeinschaft (DFG) within the priority program SPP 1613 (LE 781/13-2, BR 1768/9-1, WA 1116/28).

References

- [1] G. K. Layden, *Mat. Res. Bull.* **1968**, *3*, 349.
- [2] T. Siegrist, R. J. Cava, J. J. Krajewski, *Mat. Res. Bull.* **1997**, *32*, 881.
- [3] F. Galasso, L. Katz, *Acta Cryst* **1961**, *14*, 647.
- [4] C. D. Ling, M. Avdeev, V. V. Kharton, A. A. Yaremchenko, R. B. Macquart, M. Hoelzel, *Chem. Mater.* **2010**, *22*, 532.
- [5] A. Ritter, T. Lydssan, B. Harbrecht, *Z. Anorg. Allg. Chem.* **1998**, *624*, 1791.
- [6] C. R. Feger, R. P. Ziebarth, *Chem. Mater.* **1995**, *7*, 373.
- [7] R. Marschall, J. Soldat, G. W. Busser, M. Wark, *Photochem. Photobiol. Sci.* **2013**, *12*, 671.
- [8] R. Asahi, T. Morikawa, T. Ohwaki, K. Aoki, Y. Taga, *Science (New York, N.Y.)* **2001**, *293*, 269.
- [9] W. Zhao, W. Ma, C. Chen, J. Zhao, Z. Shuai, *J. Am. Chem. Soc.* **2004**, *126*, 4782.
- [10] S. In, A. Orlov, R. Berg, F. García, S. Pedrosa-Jimenez, M. S. Tikhov, D. S. Wright, R. M. Lambert, *J. Am. Chem. Soc.* **2007**, *129*, 13790.
- [11] G. Liu, C. Sun, L. Cheng, Y. Jin, H. Lu, L. Wang, S. C. Smith, G. Q. Lu, H.-M. Cheng, *J. Phys. Chem. C* **2009**, *113*, 12317.
- [12] Khan, Shahed U M, M. Al-Shahry, W. B. Ingler, *Science (New York, N.Y.)* **2002**, *297*, 2243.
- [13] S. Sakthivel, H. Kisch, *Angew. Chem. Int. Ed. Eng.* **2003**, *42*, 4908.
- [14] K. Nagaveni, M. S. Hegde, N. Ravishankar, G. N. Subbanna, G. Madras, *Langmuir* **2004**, *20*, 2900.
- [15] Y. Choi, T. Umebayashi, M. Yoshikawa, *Journal of Materials Science* **2004**, *39*, 1837.
- [16] S. K. Mohapatra, M. Misra, V. K. Mahajan, K. S. Raja, *J. Phys. Chem. C* **2007**, *111*, 8677.
- [17] J. C. Yu, Yu, Ho, Jiang, Zhang, *Chem. Mater.* **2002**, *14*, 3808.
- [18] Di Li, H. Haneda, S. Hishita, N. Ohashi, *Chem. Mater.* **2005**, *17*, 2596.
- [19] W. Ho, J. C. Yu, S. Lee, *Chem. Commun. (Camb.)* **2006**.
- [20] K. Maeda, Y. Shimodaira, B. Lee, K. Teramura, D. Lu, H. Kobayashi, K. Domen, *J. Phys. Chem. C* **2007**, *111*, 18264.
- [21] X. Zong, Z. Xing, H. Yu, Z. Chen, F. Tang, J. Zou, G. Q. Lu, L. Wang, *Chem. Commun. (Camb.)* **2011**, *47*, 11742.
- [22] J. L. Gole, J. D. Stout, C. Burda, Y. Lou, X. Chen, *J. Phys. Chem. B* **2004**, *108*, 1230.
- [23] I. N. Martyanov, S. Uma, S. Rodrigues, K. J. Klabunde, *Chem. Commun. (Camb.)* **2004**.
- [24] S. Livraghi, M. C. Paganini, E. Giamello, A. Selloni, C. Di Valentin, G. Pacchioni, *J. Am. Chem. Soc.* **2006**, *128*, 15666.
- [25] Y. Cong, J. Zhang, F. Chen, M. Anpo, *J. Phys. Chem. C* **2007**, *111*, 6976.

- [26] J. Fang, F. Wang, K. Qian, H. Bao, Z. Jiang, W. Huang, *J. Phys. Chem. C* **2008**, *112*, 18150.
- [27] T. Umebayashi, T. Yamaki, H. Itoh, K. Asai, *Appl. Phys. Lett.* **2002**, *81*, 454.
- [28] T. Umebayashi, T. Yamaki, S. Tanaka, K. Asai, *Chem. Lett.* **2003**, *32*, 330.
- [29] T. Ohno, M. Akiyoshi, T. Umebayashi, K. Asai, T. Mitsui, M. Matsumura, *Applied Catalysis A: General* **2004**, *265*, 115.
- [30] Y. Izumi, T. Itoi, S. Peng, K. Oka, Y. Shibata, *J. Phys. Chem. C* **2009**, *113*, 6706.
- [31] M. Higashi, K. Domen, R. Abe, *J. Am. Chem. Soc.* **2013**, *135*, 10238.
- [32] K. Maeda, D. Lu, K. Domen, *ACS Catal.* **2013**, *3*, 1026.
- [33] M. Yoshida, K. Maeda, D. Lu, J. Kubota, K. Domen, *J. Phys. Chem. C* **2013**, *117*, 14000.
- [34] R. Assabaa-Boultif, *thesis #912, the University of Rennes 1, France* **1993**, <https://books.google.de/books?id=28psOQAACAAJ>.
- [35] M. P. Pechini, *US Pat. No. 3.330.697* **1967**.
- [36] J. Rodriguez-Carvajal, *Physica B* **1993**, *55*, 192.
- [37] I. Bannat, K. Wessels, T. Oekermann, J. Rathousky, D. Bahnemann, M. Wark, *Chem. Mater.* **2009**, *21*, 1645.
- [38] L. Bi, J. Y. Feng, *J. Lumin.* **2006**, *121*, 95.
- [39] J. Tauc, *Mat. Res. Bull.* **1968**, *3*, 37.
- [40] Van Leeuwen, Robert A., C.-J. Hung, D. R. Kammler, J. A. Switzer, *J. Phys. Chem.* **1995**, *99*, 15247.
- [41] Y. Zhang, G. Li, Y. Wu, Y. Luo, L. Zhang, *J. Phys. Chem. B* **2005**, *109*, 5478.
- [42] R. Dovesi, R. Orlando, A. Erba, C. M. Zicovich-Wilson, B. Civalleri, S. Casassa, L. Maschio, M. Ferrabone, De La Pierre, Marco, P. D'Arco, Y. Noël, M. Causà, M. Rérat, B. Kirtman, *Int. J. Quantum Chem.* **2014**, *114*, 1287.
- [43] S. Nakhil, M.-W. Lumey, T. Bredow, R. Dronskowski, M. Lerch, *Z. Anorg. Allg. Chem.* **2010**, *636*, 1006.
- [44] T. Bredow, A. R. Gerson, *Phys. Rev. B* **2000**, *61*, 5194.
- [45] www.crystal.unito.it/basis-sets.php.
- [46] A. V. Krukau, O. A. Vydrov, A. F. Izmaylov, G. E. Scuseria, *J. Chem. Phys.* **2006**, *125*, 224106.
- [47] M. F. Peintinger, D. V. Oliveira, T. Bredow, *J. Comput. Chem.* **2013**, *34*, 451.
- [48] D. Andrae, U. Häußermann, M. Dolg, H. Stoll, H. Preuß, *Theoret. Chim. Acta* **1990**, *77*, 123.
- [49] M. Kaupp, Schleyer, P. v. R., H. Stoll, H. Preuss, *J. Chem. Phys.* **1991**, *94*, 1360.
- [50] J. Soldat, R. Marschall, M. Wark, *Chem. Sci.* **2014**, *5*, 3746.
- [51] R. D. Shannon, *Acta Cryst A* **1976**, *32*, 751.
- [52] A. Fuertes, *Inorg. Chem.* **2006**, *45*, 9640.
- [53] T. Lüdtkke, A. Schmidt, C. Göbel, A. Fischer, N. Becker, C. Reimann, T. Bredow, R. Dronskowski, M. Lerch, *Inorg. Chem.* **2014**, *53*, 11691.

5. Publication 2

From $\text{Ba}_3\text{Ta}_5\text{O}_{14}\text{N}$ to $\text{La Ba}_2\text{Ta}_5\text{O}_{13}\text{N}_2$: Decreasing the Optical Band Gap of a Photocatalysts

B. Anke, T. Bredow, M. Pilarski, M. Wark, M. Lerch

published

Journal of Solid State Chemistry 246 (2017) 75–80

doi: 10.1016/j.jssc.2016.11.001

<https://doi.org/10.1016/j.jssc.2016.11.001>

Contribution to publication:

B. Anke: Sample preparation, chemical analysis and crystal structure analysis, UV-Vis interpretation, and writing.

T. Bredow: Quantum-chemical calculations.

M. Pilarski: Measurements (photocatalysis), evaluation.

M. Wark: General discussion, proofreading.

M. Lerch: General advice and helpful comments, proofreading

Authors: *B. Anke*,¹ *T. Bredow*,² *M. Pilarski*,³ *M. Wark*,³ *M. Lerch**¹

¹Institut für Chemie, Technische Universität Berlin,
Straße des 17. Juni 135, 10623 Berlin

² Mulliken Center for Theoretical Chemistry, Institut für Physikalische und
Theoretische Chemie, Universität Bonn, Beringstr. 4, 53115 Bonn

³ Institut für Chemie, Carl von Ossietzky Universität Oldenburg,
Carl-von-Ossietzky-Str. 9-11, 26129 Oldenburg

*corresponding author

Keywords: barium tantalum oxide, oxide nitrides, synthesis, crystal structure,
quantum-chemical calculations, photocatalysis

5.1. Abstract

Yellow $\text{LaBa}_2\text{Ta}_5\text{O}_{13}\text{N}_2$ was successfully synthesized as phase-pure material crystallizing isostructurally to previously reported $\text{Ba}_3\text{Ta}_5\text{O}_{14}\text{N}$ and mixed-valence $\text{Ba}_3\text{Ta}^{\text{V}}_4\text{Ta}^{\text{IV}}\text{O}_{15}$. The electronic structure of $\text{LaBa}_2\text{Ta}_5\text{O}_{13}\text{N}_2$ was studied theoretically with the range-separated hybrid method HSE06. The most stable structure was obtained when lanthanum was placed on $2a$ and nitrogen on $4h$ sites confirming Pauling's second rule. By incorporating nitrogen, the measured band gap decreases from ~ 3.8 eV for the oxide via 2.74 eV for $\text{Ba}_3\text{Ta}_5\text{O}_{14}\text{N}$ to 2.63 eV for the new oxide nitride, giving rise to an absorption band well in the visible-light region. Calculated fundamental band gaps confirm the experimental trend. The atom-projected density of states has large contributions from N2p orbitals close to the valence band edge. These are responsible for the observed band gap reduction. Photocatalytic hydrogen formation was investigated and compared with that of $\text{Ba}_3\text{Ta}_5\text{O}_{14}\text{N}$ revealing significantly higher activity for $\text{LaBa}_2\text{Ta}_5\text{O}_{13}\text{N}_2$.

5.2. Introduction

Reductive photocatalytic splitting of water using sunlight has received a lot of attention because of its potential to convert solar energy into chemical energy. So far, most investigations have focused on transition metal oxide-based photocatalysts containing zirconium, titanium, niobium, or tantalum.[1–3] These materials show relatively good photocatalytic activity under UV-light and sufficient chemical stability. Unfortunately, the band gap energies of these oxides are too large to allow the efficient absorption of visible light. Even though non-oxide photocatalysts such as Ta_3N_5 or CdSe have smaller optical band gaps that match the spectral distribution of the sunlight, the biggest disadvantage of these materials is their instability under irradiation.[4,5] Respecting all these aspects, the development of stable photocatalysts with high activity under visible light ($\lambda > 400$ nm) is a very challenging and important subject of research for the efficient utilization of solar energy.

In contrast to the oxide semiconductors, transition metal oxide nitrides such as β -TaON, BaTaO_2N , and LaTaON_2 ,[6–9] exhibit narrower band gaps due to a mixing of N 2p

states with O 2p states.[10] Although these oxide nitrides have attracted great interest in the water splitting community, the number of nitrogen-containing photocatalysts with significant activity is limited. Consequently, the search of new compounds seems to be worth the efforts. Derived from the well-known mixed-valent oxide $\text{Ba}_3\text{Ta}^{\text{V}}_4\text{Ta}^{\text{IV}}\text{O}_{15}$, we recently reported an oxide nitride catalyst ($\text{Ba}_3\text{Ta}^{\text{V}}_5\text{O}_{14}\text{N}$) exhibiting an optical band gap of 2.74 eV. For a further narrowing of the band gap the amount of nitrogen has to be increased. As all tantalum in $\text{Ba}_3\text{Ta}^{\text{V}}_5\text{O}_{14}\text{N}$ is in the highest possible formal oxidation state, combined cation/anion substitution has to be taken into account. In the following, the results of our attempts in carrying out $\text{Ba}^{2+}/\text{O}^{2-} \rightarrow \text{La}^{3+}/\text{N}^{3-}$ co-substitution, leading to $\text{LaBa}_2\text{Ta}^{\text{V}}_5\text{O}_{13}\text{N}_2$, are presented.

5.3. Experimental Section

5.3.1. Synthesis

An amorphous quaternary La-Ba-Ta-O phase was synthesized via a sol-gel based Pechini route.[11] Citrate complexes of tantalum, lanthanum, and barium were prepared. For the lanthanum citrate solution, lanthanum chloride powder (Sigma Aldrich, 99.9 %) was dissolved in an ethanol/water mixture containing citric acid (Sigma Aldrich 99.5 %). The latter was used in a molar excess of 12 times the LaCl_3 . Barium and tantalum citrate solutions were prepared using barium chloride (Sigma Aldrich, 99.9 %) and tantalum(V) chloride powder (Sigma Aldrich, 99.999 %) by dissolving them in ethanol containing citric acid as well. All solutions were mixed in a molar ratio of 1:2:5 with ethylene glycol and polymerized at 200 °C in a batch furnace. After calcination at 400 °C an amorphous oxide was obtained. This precursor was treated with a mixture of NH_3 and O_2 at 875 °C for 24 h in a tube furnace with flow rates of $10 \text{ L}\cdot\text{h}^{-1}$ and $0.03 \text{ L}\cdot\text{h}^{-1}$ for ammonia and oxygen, respectively. After that treatment the sample was cooled down rapidly to ambient temperature (~ 30 min).

5.3.2. Chemical and structural characterization

The products were characterized by X-ray powder diffraction using a PANalytical X'Pert PRO diffractometer (Bragg-Brentano geometry, Cu-K α radiation). All structural refinements were performed with the program *FullProf* Suite Version 2009 by applying

a pseudo-Voigt function.[12] Nitrogen and oxygen contents were determined using the hot gas extraction method (LECO TC-300/EF-300). For calibration, ZrO₂ and steel (LECO calibration sample, N: 5000 ppm) were used as standard materials. The accuracy is ~ 2 % for the presented N/O content. X-ray fluorescence spectrometry (XRF) was performed using a PANalytical Axios spectrometer with an Rh-tube.

5.3.3. UV-vis spectroscopy

Diffuse reflectance spectra were collected with a Jasco V670 spectrometer using MgO as white standard. Absorbance spectra were calculated from the measured diffuse reflectance with the Kubelka-Munk function. The optical band gap was determined using the *Derivation of absorption spectrum fitting* (DASF) method of Souiri *et al.*, which is described in detail elsewhere. [13–16] The final equations for this method are:

$$\ln \left[\frac{A(\lambda)}{\lambda} \right] = \ln(D) + m \ln \left(\frac{1}{\lambda} - \frac{1}{\lambda_{bg}} \right) \quad (1)$$

and

$$\frac{d\{\ln[A(\lambda)/\lambda]\}}{d(1/\lambda)} = \frac{m}{\left(\frac{1}{\lambda} - \frac{1}{\lambda_{bg}}\right)} \quad (2)$$

$A(\lambda)$ is the absorbance calculated from the Kubelka-Munk function, the value of m denotes the nature (direct, indirect, forbidden) of the transition, D is a proportional constant, and λ_{bg} the wavelength corresponding to the band gap energy.

5.3.4. Quantum-chemical methods

The electronic structure of Ba₃Ta₅O₁₅, Ba₃Ta₅O₁₄N, and LaBa₂Ta₅O₁₃N₂ was calculated with the crystalline-orbital program CRYSTAL14 [17] applying the range-separated hybrid method HSE06.[18] This approach was found to provide best agreement between theory and experiment for the band gap of Ba₃Ta₅O₁₄N in a previous study.[19] The present calculations differ from those of Ref. [19] by slight variations in the atomic basis sets. The following basis sets were used: O and N were described with slightly modified pob-TZVP all-electron basis sets;[20] for the heavy elements (Ba, La, and Ta) effective core potentials and valence basis sets of the Stuttgart-Dresden group were employed.[21–23] The most diffuse shells had to be removed in order to obtain numerically stable results in the self-consistent field procedure. The dependence of the calculated band gaps from computational accuracy parameters was checked, and

converged Monkhorst-Pack grids ($8 \times 8 \times 8$) and integral truncation thresholds (7,7,7,14,42) were used. The lattice parameters of the three compounds were taken from this work, from Ref. [19], and from Ref. [24].

5.3.5. Photocatalysis

Photocatalytic hydrogen evolution tests were performed in a self-made semi-batch reactor with a total reactor volume of 600 mL. The photoreactor system, consisting of a double-walled inner lamp cooling part made out of fused silica and a double-walled reactor reservoir made of borosilicate glass, being connected to each other, was cooled by a cryostat (LAUDA) to a temperature of 10 °C. A 700 W Hg mid-pressure immersion lamp (UV-Consulting Peschl[®]; TQ 718), set to a power of 500 W, was utilized as irradiation source. Evolved gases were analyzed online with a multi component detection unit (XStream Emerson Process Management). Concentrations of produced hydrogen, oxygen, and carbon dioxide were determined via thermal conductivity, magnetic measurements, and infrared spectroscopy, respectively. A constant argon carrier gas flow of 50 NmL/min was adjusted by a mass flow controller (Bronkhorst) for a steady transport of produced gases from the photoreactor to the detection unit.[19]

300 mg of $\text{LaBa}_2\text{Ta}_5\text{O}_{13}\text{N}_2$ were suspended in a reaction solution containing 550 mL water and 50 mL methanol. Prior, $\text{LaBa}_2\text{Ta}_5\text{O}_{13}\text{N}_2$ was pretreated in the ultrasonic bath for 10 min at 30 °C in order to obtain complete dispersion of the photocatalyst material in the reaction solution. The photoreactor system was purged by an argon stream of 100 NmL/min for 30 min to remove all atmospheric contaminations from the tubings as well as from the photoreactor itself. A Rh co-catalyst loading of 0.0125 wt%, found as being optimum in previous studies with comparable photocatalysts [19,25,26] was in-situ deposited on the $\text{LaBa}_2\text{Ta}_5\text{O}_{13}\text{N}_2$ surface via reductive photodeposition by injecting a specific amount of a 1 mM precursor solution containing Na_3RhCl_6 (99.999 %, Aldrich) into the photocatalyst suspension. In order to simulate visible light irradiation a lamp cooling device consisting of borosilicate glass, which cuts off UV light emission from the used irradiation source, was used. In all experiments the suspension temperature was held at 13 °C.

5.4. Results and discussion

5.4.1. Chemical analysis and crystal structure

We successfully synthesized light yellow $\text{LaBa}_2\text{Ta}_5\text{O}_{13}\text{N}_2$ as phase-pure material: XRF analysis proved the La/Ba/Ta content of 11 wt% La, 21 wt% Ba, and 68 wt% Ta (expected: 10.5 wt% La, 20.8 wt% Ba, 68.6 wt% Ta). The nitrogen content of $\text{LaBa}_2\text{Ta}_5\text{O}_{13}\text{N}_2$ was determined by the hot gas extraction method (exp.: 1.8 wt%; theo.: 1.8 wt%).

The X-ray powder diagram with the results of the Rietveld refinement is depicted in Figure 5.1. The refined structural parameters of $\text{LaBa}_2\text{Ta}_5\text{O}_{13}\text{N}_2$ are presented in Tables 5.1 and 5.2, also in comparison to $\text{Ba}_3\text{Ta}_5\text{O}_{14}\text{N}$ and $\text{Ba}_3\text{Ta}_5\text{O}_{15}$. The unit cell with the connectivity of the coordination polyhedra is depicted in Figure 5.2. Further details of the crystal structure investigation may be obtained from the Fachinformationszentrum Karlsruhe, D-76344 Eggenstein-Leopoldshafen (Germany), on quoting the depository number CSD-431895.

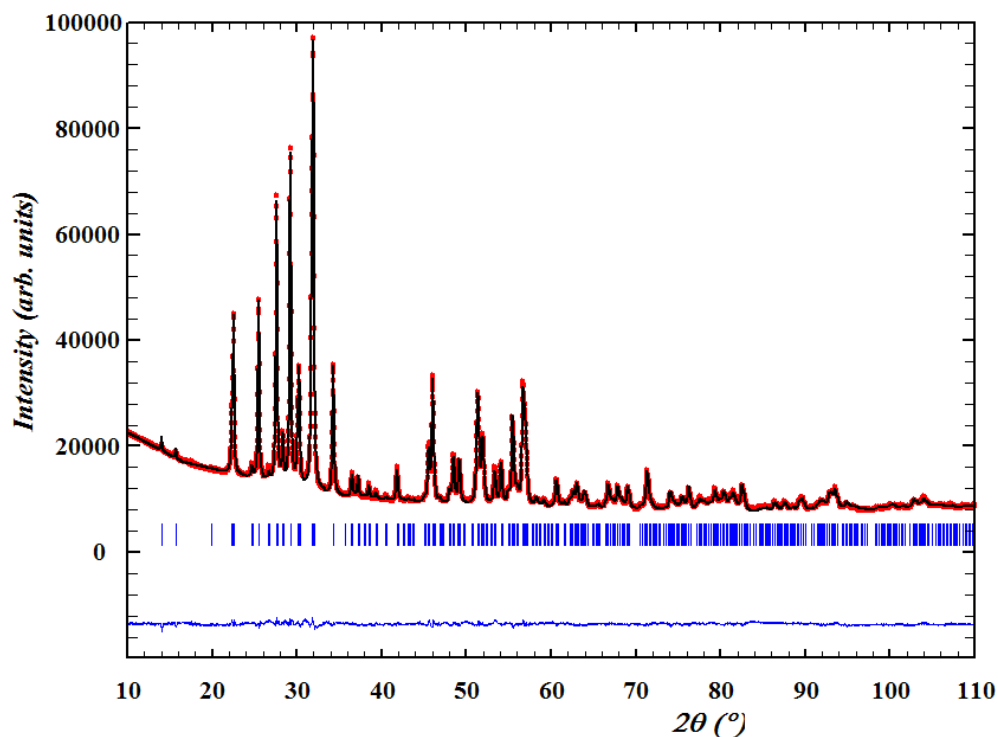
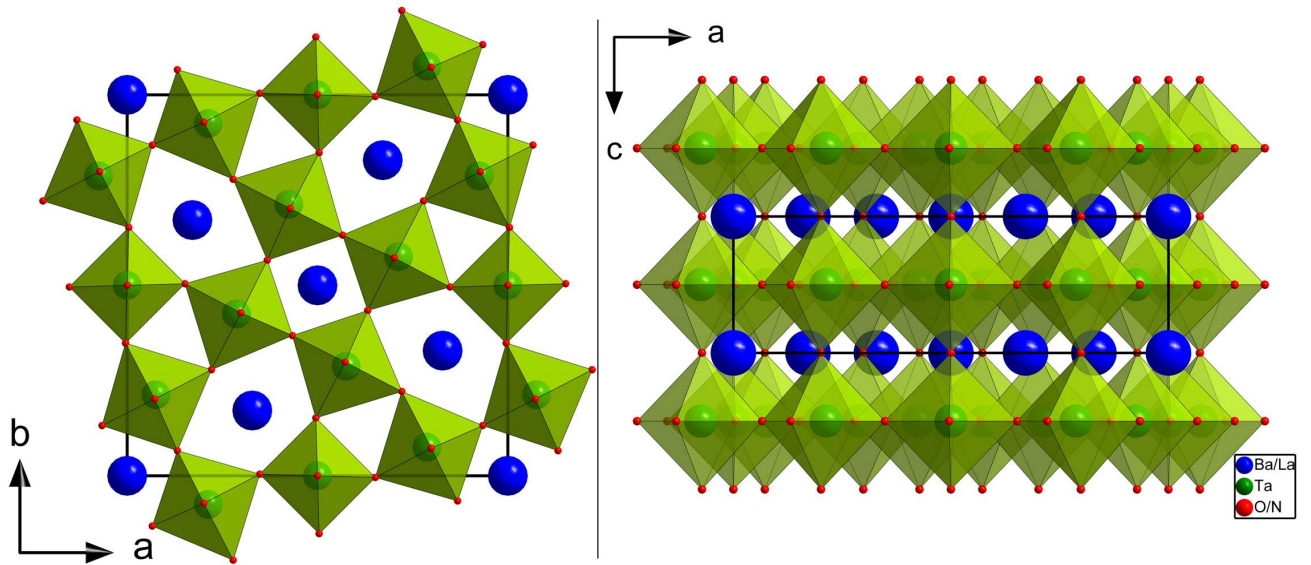


Figure 5.1: X-ray powder diffraction pattern of $\text{LaBa}_2\text{Ta}_5\text{O}_{13}\text{N}_2$ with the results of the Rietveld refinement.

Table 5.1: Refined structural parameters of $\text{LaBa}_2\text{Ta}_5\text{O}_{13}\text{N}_2$ in comparison to $\text{Ba}_3\text{Ta}_5\text{O}_{14}\text{N}$ and $\text{Ba}_3\text{Ta}_5\text{O}_{15}$.

Composition	$\text{LaBa}_2\text{Ta}_5\text{O}_{13}\text{N}_2$	$\text{Ba}_3\text{Ta}_5\text{O}_{14}\text{N}$ [11]	$\text{Ba}_3\text{Ta}_5\text{O}_{15}$ [24]
Measure	powder diffraction		single crystal
Crystal system	tetragonal		
Space group	$P4/mbm$		
Formular units	$Z=2$		
Lattice parameters	$a = 12.5852(5) \text{ \AA}$ $c = 3.9412(2) \text{ \AA}$	$a = 12.6461(9) \text{ \AA}$ $c = 3.9667(5) \text{ \AA}$	$a = 12.590(1) \text{ \AA}$ $c = 3.967(2) \text{ \AA}$
c/a ratio	3.193	3.188	3.174
Unit cell volume	$V = 624.24(4) \text{ \AA}^3$	$V = 634.38(9) \text{ \AA}^3$	$V = 628.8(4) \text{ \AA}^3$
Calc. density	8.269 g/cm^3	8.139 g/cm^3	8.2214 g/cm^3
R_{wp}	0.0137	0.0175	
R_{Bragg}	0.0235	0.0288	
R_{exp}	0.009	0.0076	
S	1.6	2.3	

Figure 5.2: Unit cell of $\text{LaBa}_2\text{Ta}_5\text{O}_{13}\text{N}_2$ with the connectivity of $\text{Ta}(\text{O}/\text{N})_6$ polyhedra.Table 5.2: Refined atomic parameters for $\text{LaBa}_2\text{Ta}_5\text{O}_{13}\text{N}_2$.

Atom	Wyckoff	x	y	z
Ba/La1	$2a$	0	0	0
Ba/La2	$4g$	0.17138(8)	0.67138(8)	0
Ta1	$2c$	0	$\frac{1}{2}$	$\frac{1}{2}$
Ta2	$8j$	0.07528(6)	0.21281(6)	$\frac{1}{2}$
O/N1	$2d$	0	$\frac{1}{2}$	0
O/N2	$4h$	0.2785(6)	0.7786(6)	$\frac{1}{2}$
O/N3	$8i$	0.0722(7)	0.2014(6)	0
O/N4	$8j$	0.3482(9)	0.0043(5)	$\frac{1}{2}$
O/N5	$8j$	0.1319(7)	0.0660(9)	$\frac{1}{2}$

In comparison to our previously published work on $\text{Ba}_3\text{Ta}_5\text{O}_{14}\text{N}$, [19] the cell volume decreased about 2 % to a value of 624.2 \AA^3 . This may be explained by higher attractive electrostatic forces of La^{3+} and due to its 25 pm smaller radius compared to Ba^{2+} (C.N.= 12). [27] It should be mentioned that the c/a ratios of $\text{LaBa}_2\text{Ta}_5\text{O}_{13}\text{N}_2$, $\text{Ba}_3\text{Ta}_5\text{O}_{14}\text{N}$, and $\text{Ba}_3\text{Ta}_5\text{O}_{15}$ decrease with increasing nitrogen content. This effect has been discussed in detail in our previous contribution on $\text{Ba}_3\text{Ta}_5\text{O}_{14}\text{N}$ and can be attributed to the special distribution of the nitrogen ions. [19]

Taking into consideration the ionic radii of the cations it is evident that Ba and La occupy Wyckoff positions $2a$ and $4g$, see Table 5.2. As they cannot be distinguished by conventional X-ray methods the refinement was carried out with a statistical distribution. However, in respect to Paulings 2nd rule [28] a short look at the coordination numbers of the atoms on cation positions $2a$ and $4g$ may be helpful. Using the concept of the effective coordination number (ECoN [29]) the following values can be calculated: $2a$: 12.00, $4g$: 9.28. Consequently, it can be assumed that lanthanum should prefer the $2a$ position. It should be mentioned that, as expected, a refinement with La completely on $2a$ and Ba solely on $4g$ did not lead to a significant decrease of the R-values. The same problem arises for O/N which is discussed in detail in our contribution on $\text{Ba}_3\text{Ta}_5\text{O}_{14}\text{N}$. [19] In addition, quantum-chemical calculations on the La/Ba and O/N distribution in $\text{LaBa}_2\text{Ta}_5\text{O}_{13}\text{N}_2$ are presented below.

5.4.2. Optical properties

Yellow-colored $\text{LaBa}_2\text{Ta}_5\text{O}_{13}\text{N}_2$ and light yellow $\text{Ba}_3\text{Ta}_5\text{O}_{14}\text{N}$ were measured in diffuse reflectance geometry. The results are plotted using the DASF method in order to estimate the optical band gap. As described in the experimental part, the discontinuity at $1/\lambda$ is $1/\lambda_{bg}$ (see Figure 5.3) which can be directly converted to the band gap E_{bg} with the help of Eq. 3:

$$E_{bg}^{DASF} = 1239.83/\lambda_{bg}. \quad (3)$$

The resulting band gap of $\text{LaBa}_2\text{Ta}_5\text{O}_{13}\text{N}_2$ is 2.63 eV. Although the exact value for $\text{Ba}_3\text{Ta}_5\text{O}_{15}$ is not known yet, all pristine barium tantalum oxides offer wide band gaps in a range between 3.8 – 4.7 eV [25] allowing only light absorption in the UV region. For the corresponding oxide nitrides $\text{Ba}_3\text{Ta}_5\text{O}_{14}\text{N}$ and $\text{LaBa}_2\text{Ta}_5\text{O}_{13}\text{N}_2$ the optical band gap

is reduced to 2.74 eV and 2.63 eV, respectively. Such a narrowing is the expected behavior for increasing the nitrogen content in oxide-based materials. [10]

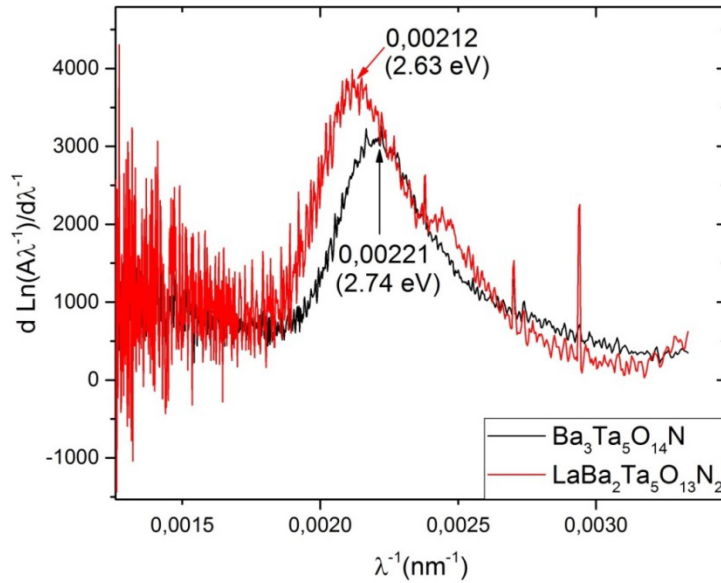


Figure 5.3: Plot of $d\{\ln(A/\lambda)\}/d(1/\lambda)$ versus $(1/\lambda)$ for $\text{Ba}_3\text{Ta}_5\text{O}_{14}\text{N}$ (black) and $\text{LaBa}_2\text{Ta}_5\text{O}_{13}\text{N}_2$ (red).

5.4.3. Quantum-chemical calculations

In the previous study on $\text{Ba}_3\text{Ta}_5\text{O}_{14}\text{N}$ [19] a strong dependence of the calculated fundamental band gap from the O/N distribution was found. The values ranged from 1.4 eV to 3.2 eV, with a monotonous decrease with decreasing stability. The most stable configuration (denoted as O/N(2)) contained both nitrogen atoms on $4h$ sites. All other distributions were less stable by more than 0.5 eV. It is therefore not likely that these will play an important role under ambient conditions unless they are kinetically stabilized during preparation. For this reason the computational study of $\text{LaBa}_2\text{Ta}_5\text{O}_{13}\text{N}_2$ focused on the O/N configuration where all $4h$ sites are occupied by N atoms. Test calculations with selected other O/N configurations confirmed that these have a much higher energy, with an energy difference comparable to $\text{Ba}_3\text{Ta}_5\text{O}_{14}\text{N}$. Also the Ba/La distribution was studied with HSE06. The theoretical results confirmed Pauling's second rule (*vide supra*). The configuration with both La atoms occupying the $2a$ site is by 1.3 eV more stable than a $2a/4g$ distribution. Therefore only the most stable anion and cation configuration were considered for band gap calculations. The optimized atom positions are given in Table 5.3. The deviations from the measured coordinates are not larger than 0.007, which could be considered as a reasonable agreement. However, while the calculated M-O distances agree with the measured

values within 0.05 Å, the Ta-N and Ba-N distances change from 2.02 Å to 1.93 Å and from 2.74 Å to 2.79 Å, respectively, during optimization. This change of the geometry leads to a significant increase of the calculated fundamental band gap from 2.64 eV to 3.16 eV (Table 5.4).

Table 5.3: Calculated atomic parameters of the $\text{LaBa}_2\text{Ta}_5\text{O}_{13}\text{N}_2$ phase and deviations from measured values in parentheses (c.f. Table 2). CRYSTAL-HSE06 results.

Atom	Wyckoff	x	y	z
La	$2a$	0	0	0
Ba	$4g$	0.1670(-0.0044)	0.6670(-0.0044)	0
Ta1	$2c$	0	$\frac{1}{2}$	$\frac{1}{2}$
Ta2	$8j$	0.0822(+0.0069)	0.2148(0.0020)	$\frac{1}{2}$
O1	$2d$	0	$\frac{1}{2}$	0
N2	$4h$	0.2782(-0.0004)	0.7782(-0.0004)	$\frac{1}{2}$
O3	$8i$	0.0651(-0.0071)	0.1988(-0.0026)	0
O4	$8j$	0.3433(-0.0049)	0.0087(+0.0049)	$\frac{1}{2}$
O5	$8j$	0.1301(-0.0018)	0.0672(+0.0012)	$\frac{1}{2}$

Table 5.4: Calculated fundamental direct (d) and indirect (id) band gaps (eV) for $\text{Ba}_3\text{Ta}_5\text{O}_{15}$, $\text{Ba}_3\text{Ta}_5\text{O}_{14}\text{N}$, and $\text{LaBa}_2\text{Ta}_5\text{O}_{13}\text{N}_2$. Only the results for the most stable La/Ba and O/N distributions are shown. CRYSTAL-HSE06 results.

Compound	id	d
$\text{Ba}_3\text{Ta}_5\text{O}_{15}$	3.74	5.23
$\text{Ba}_3\text{Ta}_5\text{O}_{14}\text{N}$	3.18	4.08
$\text{LaBa}_2\text{Ta}_5\text{O}_{13}\text{N}_2$	3.16 (2.64)*	3.99 (3.52)*

*atom positions taken from the XRD measurements of the present study

The calculation of optical gaps for solids can nowadays be achieved e.g. by the GW-BSE approach (see e.g. Ref. [30]). These methods are, however, computationally heavily demanding and could not be applied for the present systems. Instead we used a range-separated hybrid density functional to calculate the band structure of the solids. In our previous study [19] this method gave the best agreement with the measured optical gap for $\text{Ba}_3\text{Ta}_5\text{O}_{14}\text{N}$. Yet the calculated fundamental gaps overestimate the optical band gap since excitonic effects are not included. In the present case the overestimation is quite large, 0.4-0.5 eV. The with HSE06 calculated fundamental band gaps of the compounds $\text{Ba}_3\text{Ta}_5\text{O}_{15}$, $\text{Ba}_3\text{Ta}_5\text{O}_{14}\text{N}$, and $\text{LaBa}_2\text{Ta}_5\text{O}_{13}\text{N}_2$ are 3.74 eV, 3.18 eV, and 3.16 eV, respectively (Table 5.4). The latter value is reduced to 2.64 eV if the experimental atom positions from Table 5.2 are taken which is in striking agreement with the measured value of 2.63 eV. This raises the question if the overestimation is not

rather due to errors in the calculated structure than to neglected excitonic effects. Thus it may be recommendable to use experimental structure parameters wherever possible. But it has to be noted that such an approach was not possible for $\text{Ba}_3\text{Ta}_5\text{O}_{14}\text{N}$, where the partial occupation of $4h$ sites with N and O led to a lowering of the symmetry. For this system the optimization of atom positions in the quantum-chemical model calculation is better justified because the XRD measurement gives an average position for O and N.

The calculated band gaps in any case confirm the trends of the UV/vis spectra that nitrogen incorporation leads to a decrease of the band gap. The effect can be seen in the calculated atom-projected densities of states (Figure 5.4). The N2p orbitals have large contributions near the valence band maximum (VBM). Given the small N:O ratios of 1:14 and 2:13 in $\text{Ba}_3\text{Ta}_5\text{O}_{14}\text{N}$ and $\text{LaBa}_2\text{Ta}_5\text{O}_{13}\text{N}_2$, the relative N2p contribution at the VBM is much larger than the O2p contribution. The lower part of the conduction band is dominated by Ta5d orbitals, irrespective of the composition.

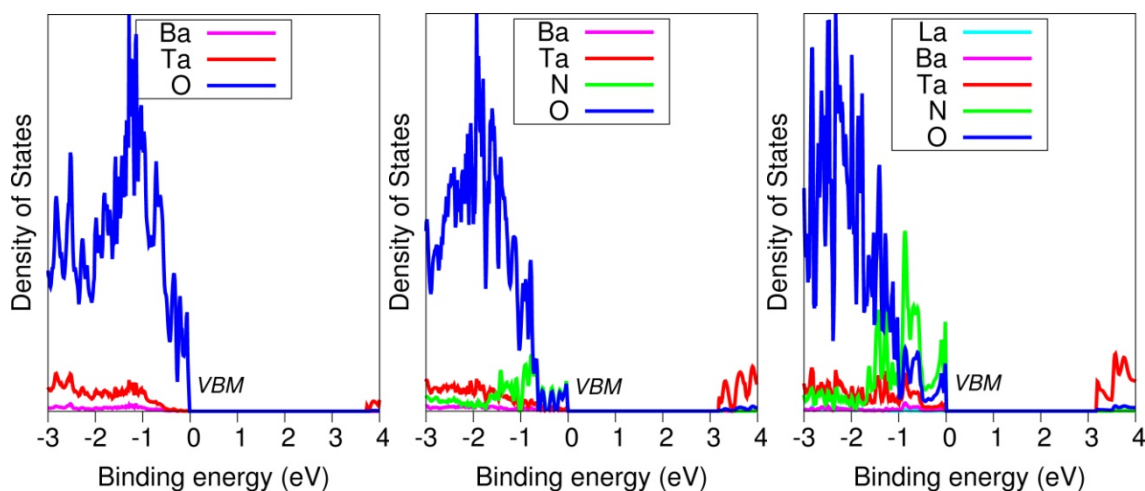


Figure 5.4: Atom-projected density of states for $\text{Ba}_3\text{Ta}_5\text{O}_{15}$ (left), $\text{Ba}_3\text{Ta}_5\text{O}_{14}\text{N}$ (center), and $\text{LaBa}_2\text{Ta}_5\text{O}_{13}\text{N}_2$ (right) as obtained with CRYSTAL-HSE06. The binding energy is given relative to the valence band maximum (VBM).

5.4.4. Photocatalysis

In absence of any co-catalyst $\text{LaBa}_2\text{Ta}_5\text{O}_{13}\text{N}_2$ provided a significantly higher H_2 evolution rate of $572 \mu\text{mol/h}$ compared to the prior tested $\text{Ba}_3\text{Ta}_5\text{O}_{14}\text{N}$ ($98 \mu\text{mol/h}$)[19] in photocatalytic methanol reforming, as shown in Figure 5.5. This proves that the material acts as an active photocatalyst and that the presence of more N enhances the activity. For co-catalyst deposition reductive *in situ* photodeposition of 0.0125 wt% of

Rh was executed on the $\text{LaBa}_2\text{Ta}_5\text{O}_{13}\text{N}_2$ surface. However, this photodeposition of Rh particles only led to a slight increase in the H_2 rate of approximately $654 \mu\text{mol/h}$. A corresponding small effect of the photocatalyst surface modification on the photocatalytic performance was also observed in case of $\text{Ba}_3\text{Ta}_5\text{O}_{14}\text{N}$. [19] This similar behavior of both photocatalysts leads to the assumption that the incorporation of La and the involved enhanced nitrogen incorporation do not lead to significant changes in the chemistry of their surface states. The present surface states, e.g. oxygen vacancies, determine the amount of reaction sites as well as the adsorption properties of the photocatalyst material. Rhodium nanoparticles are typically deposited at sites on the tantalate surface at which electrons are exposed and also hydrogen is formed. Typically, the rhodium attracts the electrons and thus enhances the charge carrier separation suppressing partly the unwanted electron-hole recombination in the photocatalyst. [25,26] However, for $\text{Ba}_3\text{Ta}_5\text{O}_{14}\text{N}$ as well as $\text{LaBa}_2\text{Ta}_5\text{O}_{13}\text{N}_2$ this charge separation seems not to be very attractive possibly because a high Schottky barrier is formed.

The activity increase of $\text{LaBa}_2\text{Ta}_5\text{O}_{13}\text{N}_2$ compared to $\text{Ba}_3\text{Ta}_5\text{O}_{14}\text{N}$ originates from changed bulk properties manifested in a decreased band gap and improved light absorption ability. Nevertheless, the improved photocatalytic activity of $\text{LaBa}_2\text{Ta}_5\text{O}_{13}\text{N}_2$ could only be observed under UV light irradiation. Activity investigations under simulated visible light conditions, realized by use of a lamp cooling device consisting of borosilicate glass and absorbing the UV emitted by the lamp, were not successful. The reduced band gap of $\text{LaBa}_2\text{Ta}_5\text{O}_{13}\text{N}_2$ compared to $\text{Ba}_3\text{Ta}_5\text{O}_{14}\text{N}$ should favor the visible light activity, but on the other hand the progressed nitrogen incorporation might increase the amount of crystal defects acting as trap states and increasing the recombination probability of electrons and holes. The bulk and surface recombination rates are so high that almost no electrons reach surface sites at which they can react with the water and methanol molecules.

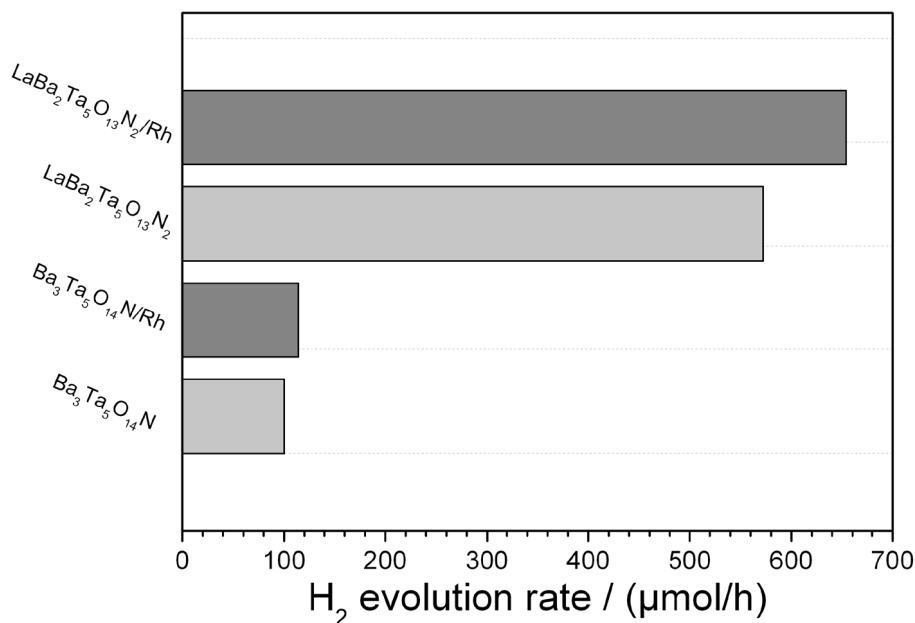


Figure 5.5: Photocatalytic H₂ evolution rates of Ba₃Ta₅O₁₄N and LaBa₂Ta₅O₁₃N₂ before and after *in-situ* photodeposition of 0.0125 wt% of Rh in H₂O/CH₃OH solution under Hg-lamp irradiation.

5.5. Conclusion

We were successfully synthesized a new oxide nitride with the composition LaBa₂Ta₅O₁₃N₂ as pure phase material exhibiting an optical band gap of 2.63 eV. Quantum chemical calculations provide a band gap of 2.64 eV, close to the measured value. This shows that N2p orbitals which are located close to the valence band maximum are responsible for the reduction of the band gap. The new phase showed a significantly higher H₂ evolution rate compared to prior tested Ba₃Ta₅O₁₄N. In the light of these results, further attempts in decreasing the optical band gap by additional co-substitution (LaBa₂Ta₅O₁₃N₂ → La₂BaTa₅O₁₂N₃ → La₃Ta₅O₁₁N₄) seem to be worth the efforts even if the challenge of preparing a phase-pure material increases with increasing nitrogen content.

Acknowledgment

The authors would like to thank M. Stöbe and N. Genz (TU Berlin) for performing XRF analyses and UV-vis spectroscopy. This work is supported by the Deutsche Forschungsgemeinschaft (DFG) within the priority program SPP 1613 (LE 781/13-2, BR 1768/9-1, WA 1116/28).

References

- [1] K. Domen, *J. Catal.* **1986**, *102*, 92.
- [2] H. Kato, K. Asakura, A. Kudo, *J. Am. Chem. Soc.* **2003**, *125*, 3082.
- [3] A. Kudo, *J. Catal.* **1988**, *111*, 67.
- [4] D. Yokoyama, H. Hashiguchi, K. Maeda, T. Minegishi, T. Takata, R. Abe, J. Kubota, K. Domen, *Thin Solid Films* **2011**, *519*, 2087.
- [5] L. Xi, J. Y. Lek, Y. N. Liang, C. Boothroyd, W. Zhou, Q. Yan, X. Hu, F. B. Y. Chiang, Y. M. Lam, *Nanotechnology* **2011**, *22*, 275706.
- [6] M. Higashi, Y. Yamanaka, O. Tomita, R. Abe, *APL Mater.* **2015**, *3*, 104418.
- [7] M. Higashi, K. Domen, R. Abe, *J. Am. Chem. Soc.* **2013**, *135*, 10238.
- [8] M. Hara, J. Nunoshige, T. Takata, J. N. Kondo, K. Domen, *Chem. Commun.* **2003**.
- [9] K. Ueda, H. Kato, M. Kobayashi, M. Hara, M. Kakihana, *J. Mater. Chem. A* **2013**, *1*, 3667.
- [10] K. Domen, M. Hara, J. N. Kondo, T. Takata, A. Kudo, H. Kobayashi, Y. Inoue, *Korean J. Chem. Eng.* **2001**, *18*, 862.
- [11] M. P. Pechini, *US Pat. No.3.330.697* **1967**.
- [12] J. Rodriguez-Carvajal, *Physica B* **1993**, *55*, 192.
- [13] D. Souri, K. Shomalian, *J. Non-Cryst. Solids* **2009**, *355*, 1597.
- [14] D. Souri, Z. E. Tahan, *Appl. Phys. B* **2015**, *119*, 273.
- [15] L. Escobar-Alarcón, A. Arrieta, E. Camps, S. Muhl, S. Rodil, E. Viguera-Santiago, *Appl. Surf. Sci.* **2007**, *254*, 412.
- [16] N. Ghobadi, M. Ganji, C. Luna, A. Arman, A. Ahmadpourian, *J Mater Sci: Mater Electron* **2016**, *27*, 2800.
- [17] R. Dovesi, R. Orlando, A. Erba, C. M. Zicovich-Wilson, B. Civalleri, S. Casassa, L. Maschio, M. Ferrabone, M. de La Pierre, P. D'Arco, Y. Noël, M. Causà, M. Rérat, B. Kirtman, *Int. J. Quantum Chem.* **2014**, *114*, 1287.
- [18] J. Heyd, G. E. Scuseria, M. Ernzerhof, *J. Chem. Phys.* **2006**, *124*, 219906.
- [19] B. Anke, T. Bredow, J. Soldat, M. Wark, M. Lerch, *J. Solid State Chem.* **2016**, *233*, 282.
- [20] M. F. Peintinger, D. V. Oliveira, T. Bredow, *J. Comput. Chem.* **2013**, *34*, 451.
- [21] D. Andrae, U. Haeussermann, M. Dolg, H. Stoll, H. Preuss, *Theoret. Chim. Acta* **1990**, *77*, 123.
- [22] M. Kaupp, P. v. R. Schleyer, H. Stoll, H. Preuss, *J. Chem. Phys.* **1991**, *94*, 1360.
- [23] J. Yang, M. Dolg, *Theor Chem Acc* **2005**, *113*, 212.
- [24] C. R. Feger, R. P. Ziebarth, *Chem. Mater.* **1995**, *7*, 373.
- [25] J. Soldat, R. Marschall, M. Wark, *Chem. Sci.* **2014**, *5*, 3746.
- [26] R. Marschall, J. Soldat, G. W. Busser, M. Wark, *Photochem. Photobiol. Sci.* **2013**, *12*, 671.
- [27] R. D. Shannon, *Acta Cryst A* **1976**, *32*, 751.
- [28] A. Fuertes, *Inorg. Chem.* **2006**, *45*, 9640.
- [29] R. Hoppe, *Angew. Chem.* **1970**, *82*, 7.
- [30] R. Starke, G. Kresse, *Phys. Rev. B* **2012**, *85*.

6. Publication 3

Improved photoelectrochemical performance of bismuth vanadate by partial O/F-substitution

B. Anke, M. Rohloff, M.G. Willinger, W. Hetaba, A. Fischer, M. Lerch

published

Solid State Sciences 63 (2017) 1–8

doi: 10.1016/j.solidstatesciences.2016.11.004

<https://doi.org/10.1016/j.solidstatesciences.2016.11.004>

Contribution to publication:

B. Anke: Sample preparation, chemical analysis and crystal structure analysis, UV-Vis interpretation, density determination, and writing.

M. Rohloff: Measurements (photocatalysis), evaluation.

M. G. Willinger: General discussion, proofreading.

W. Hetaba: Measurements (EDX / TEM)

A. Fischer: General discussion, proofreading.

M. Lerch: General advice and helpful comments, proofreading

Authors: B. Anke,^{a,1} M. Rohloff,^{a,b,1} M.G. Willinger,^c W. Hetaba,^{c,d}
A. Fischer,^{*b} M. Lerch^{*a}

^a Institut für Chemie, Technische Universität Berlin,
Straße des 17. Juni 135, 10623 Berlin

^b Institut für Anorganische Chemie, Albert-Ludwigs-Universität Freiburg,
Albertstraße 21, 79104 Freiburg

^c Department of Inorganic Chemistry, Fritz Haber Institute of the Max Planck Society,
Faradayweg 4-6, 14195 Berlin

^d Department of Heterogeneous Reactions, Max-Planck-Institute for Chemical Energy
Conversion, Stiftstraße 34-36, 45470 Mülheim an der Ruhr

¹ These authors contributed equally to the research

*corresponding authors

Keywords: BiVO₄; O/F-substitution; crystal structure; optical properties;
water oxidation; photoelectrochemical water splitting

6.1. Abstract

Fluorine-containing bismuth vanadate (F:BiVO₄) powder was synthesized using a new, clean, and simple solid-vapor reaction. Incorporation of fluorine mainly leads to the formation of cation vacancies. Electrodes were fabricated from the pre-synthesized powder samples by electrophoretic deposition onto fluorine-doped tin oxide coated glass slides and subsequent calcination. The photoelectrochemical performance concerning the water oxidation reaction was investigated and compared to pristine BiVO₄ revealing strongly enhanced photoelectrochemical behaviour for the F-containing BiVO₄.

6.2. Introduction

In the past years a lot of attention was paid to the semiconductor bismuth vanadate BiVO₄, because of its outstanding catalytic properties. Since Kudo *et al.*[1] discovered BiVO₄ to be a photoactive material it is not only used as brilliant, non-toxic yellow pigment[2,3] but also as catalyst for the photodegradation of organic pollutants.[4-7] Today, most attention is paid to the use of BiVO₄ as photoanode material for water splitting under visible-light irradiation.[8]

There are many parameters influencing the photoelectrochemical performance of semiconductors with respect to water splitting.[9] For instance, the crystal structure of a semiconductor material like BiVO₄ is a very important factor to be considered. At ambient pressure BiVO₄ exhibits three important polymorphs crystallizing either in the scheelite-type structure (monoclinic, tetragonal) or in the tetragonal zircon-type structure. Among these three polymorphs, the monoclinic phase shows the highest photoelectrochemical performance for water oxidation: a result which is ascribed to the smaller band gap of the monoclinic phase (2.4 eV) compared to the one of tetragonal zircon-type structure (3.1 eV).[10]

Another way to influence the photoelectrochemical behaviour of a semiconductor is to change its electronic structure by, for example, partial cation substitution. Molybdenum and tungsten were found to be suitable cationic dopants improving the photoelectrochemical properties due to enhancement of the amount of free charge carriers within the BiVO₄ material.[11-17] Besides cationic doping, also anion

substitution, especially with fluorine, seems to lead to a decrease of the optical band gap resulting in an increase of photoelectrochemical performance.[4,18] However such materials have not been studied in detail so far.

One possible route to fluorine incorporation into oxides involves polyvinylidene fluoride (PVDF) as fluoride source and was reported by Slater.[19] Following Slater's method, the reactants must be mixed, which in terms of photo(electro-)catalytic performance might represent a big disadvantage because of potential carbon contamination of the final product. With this in mind, we developed a new process for the synthesis of F-containing BiVO_4 ($\text{F}:\text{BiVO}_4$) based on a solid-vapor reaction with separated reactants at ambient pressure and in inert gas atmosphere. Using electrophoretic deposition and taking advantage of the low-temperature sintering of BiVO_4 , the as-synthesized powders could be processed to $\text{F}:\text{BiVO}_4$ photoanodes, with highly improved PEC performance when compared to their pristine counterparts (*vide infra*).

6.3. Experimental Section

6.3.1. Synthesis

BiVO_4 was synthesized in an aqueous medium at room temperature under ambient pressure. 7.29 g Bi_2O_3 (99.9 % Aldrich) and 3.81 g NaVO_3 (98 % AlfaAesar) were dissolved in concentrated HNO_3 . After mixing these solutions, NaOH was added until the pH value reached basic conditions (pH = 12). The solution was stirred for 4 h. The resultant yellow precipitate was washed with distilled water several times to remove impurities and unreacted precursor materials, filtered, and dried at 60 °C for 12 h.

F-containing BiVO_4 was prepared by a solid-vapor reaction using an indirect gas flow apparatus (see **Figure 6.1**). Loose powder of pure BiVO_4 was loaded in a small corundum boat, which in turn was placed inside a larger corundum boat containing varying amounts of PVDF. This arrangement advantageously prevents contact between the reagents in either solid or liquid form. The nested boats were then placed inside a corundum tube with one closed end and then placed in a horizontal tube furnace with a low nitrogen gas flow of 5 l/h. The temperature was set to 380 °C for 24 hours and after

a final heating step in air at 450 °C for 30 minutes an orange powder was obtained. Thermogravimetric and mass spectroscopy studies revealed that the PVDF decomposition only emits HF under inert gas. Before electrode preparation the pristine BiVO_4 was also tempered at 450 °C to imitate the final heating step of F-containing BiVO_4 .

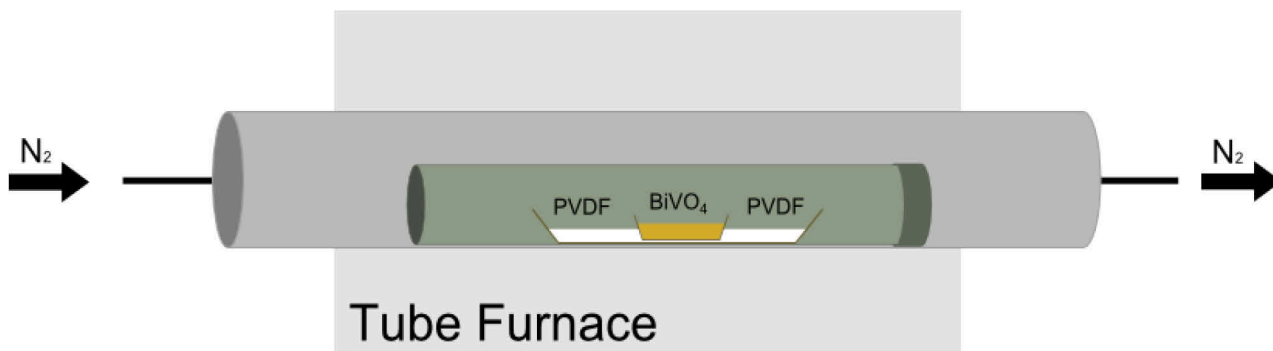


Figure 6.1: Sketch of fluorination apparatus. The inner corundum boat contains the sample to be fluorinated and the outer boat is filled with PVDF.

6.3.2. Chemical and structural characterization

The products were characterized by X-ray powder diffraction using a PANalytical X'Pert PRO diffractometer (Bragg-Brentano geometry, $\text{Cu-K}\alpha$ radiation). All structural refinements were performed with the program *FullProf Suite Version 2009* by applying a pseudo-Voigt function.[20] The oxygen content was determined by hot gas extraction method (LECO TC-300/EF-300). For calibration, ZrO_2 was used as standard material. The accuracy is $\sim 2\%$ of the presented O content. For ICP-OES investigations, 5 mg BiVO_4 powder was dissolved in 10 ml water containing 3.5 vol% HCl. Measurements were carried out using a Varian ICP-OES 715 ES with radial plasma torch. For SEM investigations of fabricated electrodes, a Hitachi SU8030 operated at an acceleration voltage of 10 kV was used. Experimental density values of the samples were measured using a Quantachrome helium multipycnometer, where the pressure change of helium in a calibrated volume is measured to calculate the sample volume. Helium penetrates into smallest pores and crevices and permits to approach the real volume of the sample. Transmission electron microscopy (TEM) and energy dispersive X-ray (EDX) analysis were performed using a FEI Talos F200X equipped with a SuperX EDX system, incorporating four Bruker silicon drift detectors (SDD).

6.3.3. UV–vis spectroscopy

Diffuse reflectance spectra were collected with a Jasco V670 spectrometer using MgO as white standard. Absorbance spectra were calculated from the measured diffuse

reflectance with the Kubelka-Munk function: $(R) = \frac{(1-R)^2}{2R} = \epsilon c \frac{1}{s}$,

where R is the reflectance, ϵ is the absorption coefficient, c the concentration of absorbing species, and s the scattering coefficient. The optical band gap was determined using the modified Tauc equation, $[F(R)hv]^{\frac{1}{n}} = A(hv - E_g)$, with $F(R)$ the Kubelka-Munk function, hv the photon energy, E_g the optical band gap, and A a proportionality constant.[21,22] The value of the exponent n denotes the nature of the transition. A direct allowed transition is present in BiVO_4 : $n = \frac{1}{2}$.[23,24]

6.3.4. Electrode Fabrication

An electrophoretic deposition method (EPD) based on a procedure Domen *et al.* reported was used to fabricate electrodes for photoelectrochemical investigations.[25] In a first step, the pristine as well as the F-containing powder was treated for 15 min in a mixer mill (Retsch GmbH MM301) to provide a comparable particle size distribution (verified by SEM-investigations). 80 mg of the respective BiVO_4 powder was dispersed in 50 ml iodine-containing acetone (2 mg I_2 /ml acetone) by extended ultrasonification (27 kHz) at room temperature. Two fluorine-doped tin oxide coated glass slides (FTO) were immersed parallel in the dispersion with 1.0 cm of distance. Particles were deposited by application of a potential of 10 V for 5 min. This procedure was repeated twice in total. After electrophoretic deposition, the as-prepared electrodes were calcined at 450 °C for 30 min under air. Additionally, electrodes were also calcined at 550 °C for 30 min under air to improve PEC performance by enhanced sintering of the electrode particles (see SI).

In order to ensure that the fluorine content of the material did not change during the described procedures, hot gas extraction measurements were carried out after the milling step, as well as after the heat treatment steps at 450 °C and 550 °C for 30 minutes, respectively. The determined oxygen contents are the same (18.2 wt%) for all samples; a result which is a clear indication for the good thermal stability of the fluorine-containing material.

6.3.5. Electrochemical Investigations

Photoelectrochemical (PEC) measurements were carried out in a 3-electrode-setup consisting of the BiVO₄- working electrode, a Pt-wire counter electrode, and a reversible hydrogen reference electrode. The potential of the working electrode was controlled by a potentiostat (Biologic SP-150). Electrodes were illuminated by a 150 W Xe-lamp at a spectral range of 400-700 nm. The light intensity at the electrode surface was adjusted to 100 mW/cm² using a Si-diode light meter. If not stated otherwise, backside illumination (i.e. illumination via the FTO-coated glass side of the BiVO₄ photoanode) was used.

A photo-assisted electrodeposition method based on the procedure reported by Durrant *et al.* was used to deposit a cobalt phosphate based water oxidation catalyst (CoPi) onto the F:BiVO₄ electrode surface.[26] The working electrode was immersed in 0.1 M potassium phosphate buffer at pH 7.3 containing 0.5 mM cobalt nitrate and a constant potential of 1.2 V vs. RHE was applied under illumination. To ensure a comparable amount of deposited CoPi for all samples, the deposition was stopped after a charge of 130 mC was flown.

All j-V-measurements were conducted in a 0.1 M potassium phosphate (KPi) buffer at pH 7.3 using a scan rate of 20 mV/s. For chronoamperometric measurements of the photocurrent transients a potential of 1.23 V vs. RHE was applied and blue light (440 nm) at an intensity of 1 mW/cm² was used. Staircase potentiometric-electrochemical impedance spectroscopy (PEIS, Mott-Schottky Analysis) was carried out in 0.5 M KPi buffer at pH 7.3 scanning from anodic to cathodic potentials and using a sinusoidal modulation of 10 mV at frequencies of 500 Hz and 1 kHz.[27] An area of 0.5 cm² of each electrode was used for measurements.

6.4. Results and discussion

6.4.1. Chemical analysis and crystal structure

We successfully synthesized orange-colored F:BiVO₄ as phase-pure material. ICP-OES analysis showed a Bi:V ratio of 0.999:1. Quantitative chemical analysis by hot gas extraction was used to measure the amount of oxygen. In the case of pristine BiVO₄ the

experimental value of 19.7 wt% is identical with the theoretical one. As an expected result of fluorine incorporation, a slightly lower value (18.2 wt%) was obtained for F:BiVO₄.

Figure 6.2 (left) depicts a bright-field transmission electron microscopy (TEM) overview image of the fluorine-containing sample while on the right side a high-resolution TEM (HRTEM) image can be seen. From the right micrograph, the crystalline structure of the particles is evident. Fast-Fourier-transformation (FFT) of this region shows the spatial frequencies due to the lattice fringes, which can be assigned to the monoclinic BiVO₄ structure.

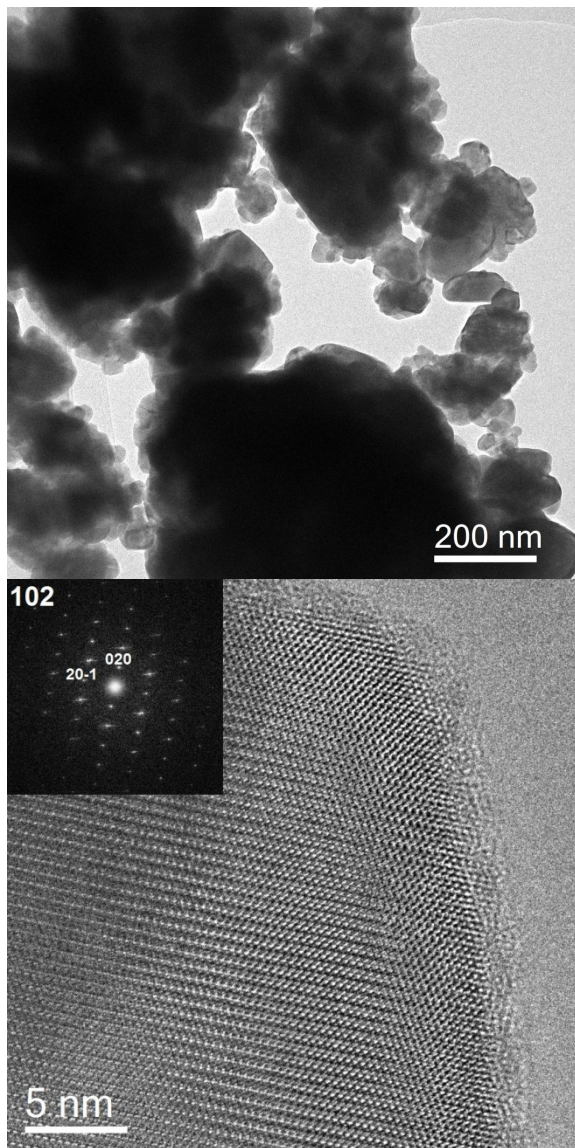


Figure 6.2: Bright field TEM image of F:BiVO₄ (left) and high resolution TEM image of one of the particles (right). The inlay shows the corresponding FFT. Spots due to the (020) and (20-1) lattice planes or the [102] oriented particle are labelled.

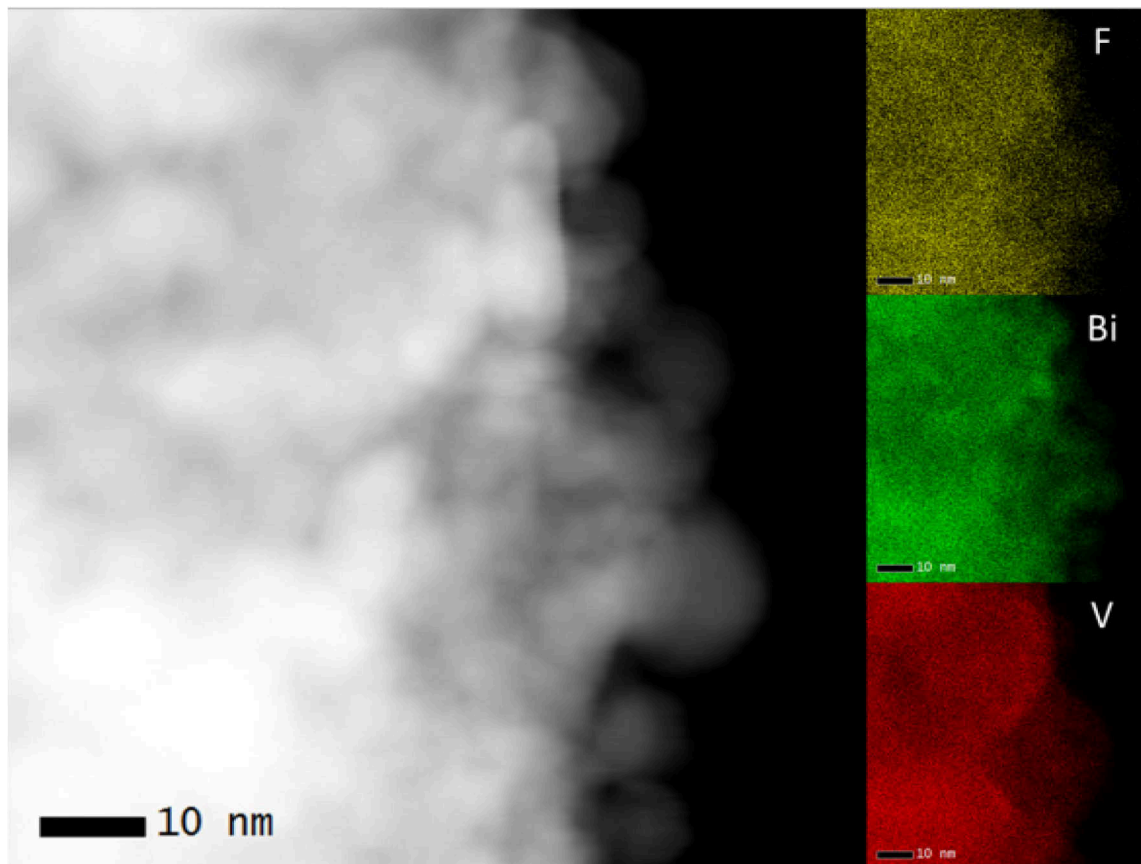


Figure 6.3: High angle annular dark field image of F:BiVO₄ (left). EDX maps of F(yellow), Bi (green) and V(red) (right from top to bottom).

Figure 6.3 presents a high angle annular dark field (HAADF) overview image with the corresponding EDX maps of F (yellow), Bi (green) and V (red), revealing a homogeneous distribution of these elements in the material. The oxygen content could not be abstracted by EDX. Due to the limited energy resolution of the EDX detector (~126 eV) the oxygen K (around 530 eV) and vanadium L (around 518 eV) ionization edges overlap to a single peak and cannot be distinguished. The vanadium content was quantified using the vanadium K-edge. Elemental quantification by EDX performed in the SEM and TEM at different magnifications confirmed a homogeneous distribution of fluorine in the material. According to the quantification, the samples contain equal amounts of Bi and V.

The structural refinements of BiVO₄ and F:BiVO₄ were started from the coordinates reported for the clinobisvanite structure of monoclinic BiVO₄ (space group *I2/b* (No. 15), JCPDS 14-0688).[28] The results clearly demonstrate that fluorine incorporation

does not change the structure type. Further details of the crystal structure investigation(s) may be obtained from the Fachinformationszentrum Karlsruhe, D-76344 Eggenstein-Leopoldshafen (Germany), on quoting the depository number CSD-431572. **Figure 6.4** depicts the X-ray powder diffraction patterns of pristine (left) and F containing (right) BiVO_4 along with the results of the Rietveld refinements. Final structural parameters are listed in **Table 6.1**.

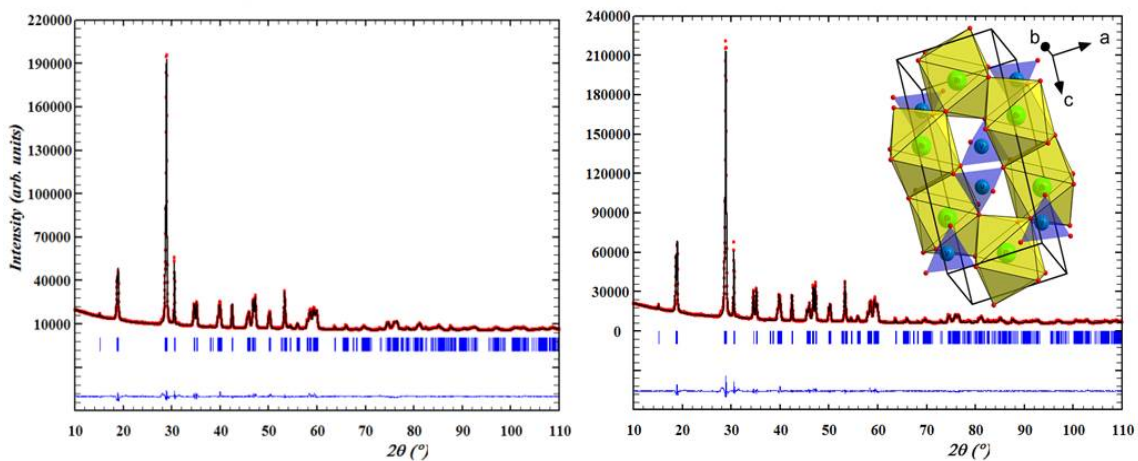


Figure 6.4: X-ray powder diffraction patterns of BiVO_4 (left) and F:BiVO_4 (right) with the results of the Rietveld refinements. Inset: Unit cell of F:BiVO_4 and polyhedral representation of the crystal structure. $\text{Bi}(\text{O},\text{F})_8$ polyhedra are drawn in yellow, $\text{V}(\text{O},\text{F})_4$ tetrahedra are shown in blue.

Table 6.1: Refined structural parameters of BiVO_4 in comparison to F:BiVO_4 .

Composition	BiVO_4	F:BiVO_4
Crystal system	monoclinic	
Space group	$I2/b$ (No. 15)	
Formular units	$Z = 4$	
Lattice parameters	$a = 5.1787(5) \text{ \AA}$	$a = 5.1863(4) \text{ \AA}$
	$b = 5.1042(5) \text{ \AA}$	$b = 5.1003(4) \text{ \AA}$
	$c = 11.6953(11) \text{ \AA}$	$c = 11.6998(8) \text{ \AA}$
	$\gamma = 90.260(2)^\circ$	$\gamma = 90.3082(12)^\circ$
Unit cell volume	$V = 309.16(5) \text{ \AA}^3$	$V = 309.47(5) \text{ \AA}^3$
Calc. density	6.962 g/cm^3	See discussion of the defect models below
R_{wp}	0.0300	0.0358
R_{Bragg}	0.0301	0.0421
R_{exp}	0.0101	0.0097
S	2.97	3.69

Table 6.2: Structural parameters for BiVO₄ and F:BiVO₄.

BiVO ₄	Wyckoff	<i>x</i>	<i>y</i>	<i>z</i>	B _{iso}	occ.
Bi	4 <i>e</i>	0	¼	0.63277(10)	0.9	0.480(2)
V	4 <i>e</i>	0	¼	0.1297(4)	0.6	0.507(2)
O1	8 <i>f</i>	0.1349(18)	0.4906(15)	0.2061(8)	1.2	1
O2	8 <i>f</i>	0.2680(13)	0.3729(18)	0.4477(8)	1.2	1
F:BiVO ₄	Wyckoff	<i>x</i>	<i>y</i>	<i>z</i>	B _{iso}	occ.
Bi	4 <i>e</i>	0	¼	0.63283(10)	0.9	0.465(3)
V	4 <i>e</i>	0	¼	0.1302(4)	0.6	0.461(3)
O1	8 <i>f</i>	0.1444(18)	0.4969(14)	0.2082(8)	1.2	1
O2	8 <i>f</i>	0.2733(51)	0.3765(18)	0.4438(7)	1.2	1

The Debye-Waller factors were not refined and set identically for both phases. Whereas the *z* parameters for both materials are comparable, it should be noted that *x* and *y* show small but significant deviations. The resulting bond lengths for BiVO₄ and F:BiVO₄ are given in the SI. The values can be described as more or less identical with no systematic trend. The refined site occupation factors are most interesting. For pristine bismuth vanadate a small but significant underoccupation for bismuth and an overoccupation for vanadium are observed. In contrast, severe underoccupations for both cations were the result of the refinement of the F-containing material. This gives us a clear hint to the correct defect model for fluorine incorporation into BiVO₄, which will be discussed below. In addition, it should be stated that, unfortunately, the elements oxygen and fluorine cannot be distinguished using X-ray or even neutron diffraction methods. Because both anion positions are coordinated by three cations, Paulings second rule cannot be used to predict a preferred position for fluorine, as it has also been generally described in the work by Fuentes.[29]

For a deeper understanding of the fluorine-containing material a closer look at possible mechanisms of fluorine incorporation is helpful. In principle, there are three different sensible defect models according to which fluorine incorporation can take place: a) formation of cation vacancies; b) fluorine on interstitial sites, and c) partial reduction of vanadium. For the following explanations we use the notation of Kröger and Vink.[30]

a) Formation of cation (vanadium and bismuth) vacancies is described by



Taking into consideration the experimentally determined oxygen content of 18.2 wt%, a chemical formula of Bi_{0.94}V_{0.94}O_{3.54}F_{0.46} can be calculated. The corresponding

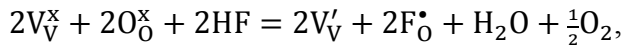
theoretical density (taken the volume from the Rietveld refinement) would account for 6.66 g/cm³.

b) Fluorine incorporation on interstitial sites is described by



leading to a chemical formula of BiVO_{3.75}F_{0.50} and a theoretical density of 7.07 g/cm³.

c) Partial reduction of vanadium from formal valence state V to IV can be described using the following equation:



resulting in a chemical formula of BiV_{0.30}^VV_{0.70}^{IV}O_{3.70}F_{0.30} and a theoretical density of 6.97 g/cm³.

In order to identify the correct defect model following considerations need to be discussed:

- The strong underoccupation of the cation positions, as determined from the Rietveld refinement, clearly points to the presence of cation vacancies (model a). In addition, the calculated chemical composition of Bi_{0.94}V_{0.94}O_{3.54}F_{0.46} is in good agreement with the composition coming from the refined site occupation factors (Bi_{0.93}V_{0.92}(O,F)₄).
- The experimentally determined density of 6.68(2) g/cm³ also clearly points to the presence of cation vacancies (expected value 6.66 g/cm³, note that for the other models the density is larger compared to that of fluorine-free BiVO₄ with a value of 6.96 g/cm³).
- The occupation of anion interstitials by fluorine (model b, BiV(O,F)_{4.25}) seems to be not very reasonable from a crystal chemistry point of view. Such a large amount of interstitial ions should strongly decrease the stability of the crystal structure.
- Due to the fact that the samples are very beam sensitive, estimations of the oxidation state on the basis of electron energy-loss spectrometry were not possible. Nevertheless, taking into account the refined cation occupation factors, the measured density, and the

observed orange color (the color of such a large amount of reduced vanadium – see calculated chemical formula – is expected to be black), model c, the reduction of vanadium, can be ruled out.

Taking into consideration the previous results, there are strong indications for the presence of cation vacancies as majority defect in fluorine-containing bismuth vanadate. From now on, we mean $\text{Bi}_{0.94}\text{V}_{0.94}\text{O}_{3.54}\text{F}_{0.46}$ when discussing F:BiVO₄.

6.4.2. Optical properties

Optical absorbance of a semiconductor plays an important role for the photoelectrochemical behavior.[31] Orange-colored F:BiVO₄ and yellow-colored BiVO₄ were measured in diffuse reflectance geometry. The results were converted to Tauc plots in order to estimate the optical band gap by extrapolating tangents to the x-axis as shown in **Figure 6.5**. For F:BiVO₄ the optical band gap is reduced to 2.38 eV in comparison to the measured pristine BiVO₄ with a band gap of 2.45 eV. This band gap reduction, also found in the contributions of Jiang *et al.*[4] and Li *et al.*,[18] is beneficial in terms of light absorption (shift of the absorption edge from 500 to 520 nm upon fluorine incorporation).

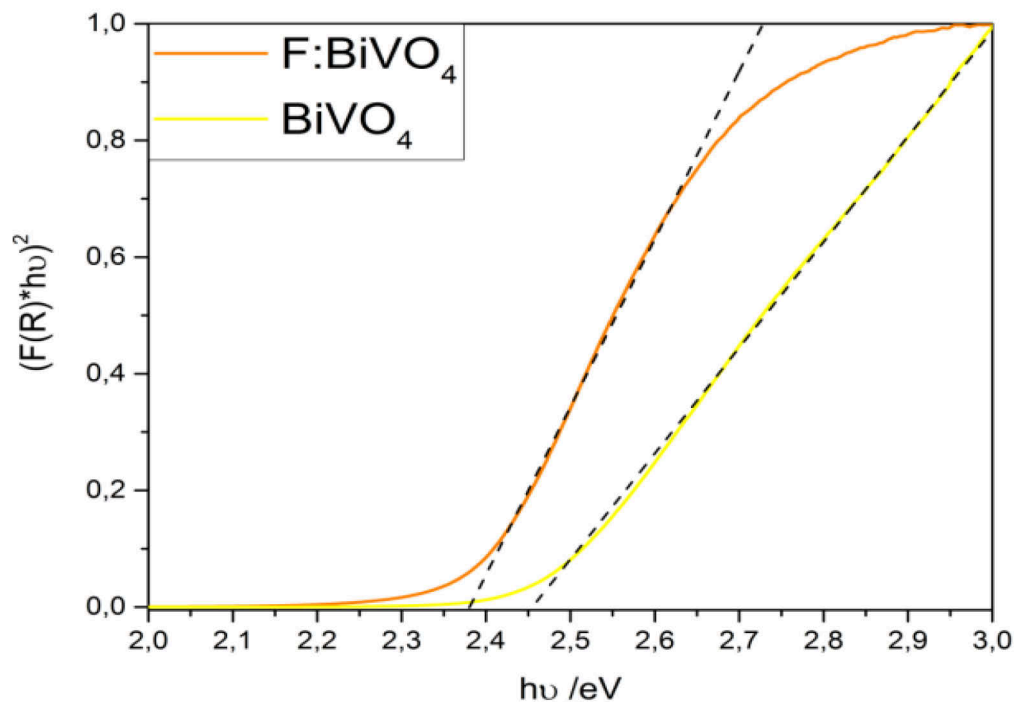


Figure 6.5: Tauc plot for BiVO₄ and F:BiVO₄ based on diffuse reflectance spectrometry.

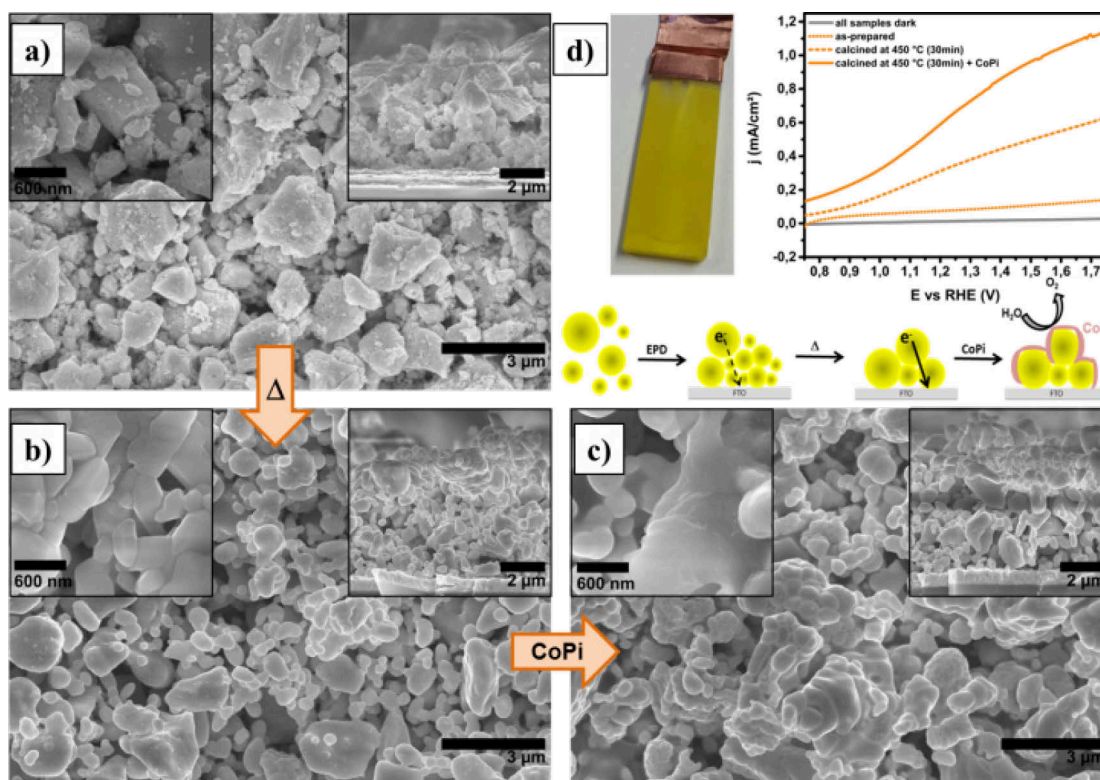


Figure 6.6: Illustration of electrode fabrication process: SEM top-view and cross-sectional images of a) as-prepared electrodes, b) calcined electrodes (450°C under air), c) calcined electrodes with deposited CoPi co-catalyst layer, d) Picture of an F:BiVO₄ electrode and j-V-curves: as-prepared F:BiVO₄, calcined F:BiVO₄ and F:BiVO₄ with a deposited CoPi layer (0.1 M KPi buffer, pH 7.3, 20 mV/s).

6.4.3. Electrochemical investigations

To investigate the photoelectrochemical properties, photoanodes were fabricated out of the pre-synthesized powders by electrophoretic deposition on FTO-coated glass slides. To achieve a good interparticle percolation within the deposited F:BiVO₄ films, a calcination step at higher temperature was performed after deposition. The respective electrode fabrication steps were thereby followed by scanning electron microscopy (top-view and cross-section) (**Figure 6.6**, see SI for SEM data of the respective samples calcined at 550 °C). As-prepared electrodes consist of a loosely packed particle layer of ~5 μm thickness which homogeneously spreads over the entire FTO substrate as shown in **Figure 6.6a**. Calcination under air (at 450 °C and 550 °C) causes sintering of the deposited particles to a more dense layer of F:BiVO₄ (**Figure 6.6b**), creating a continuously connected particle network. As shown in **Figure 6.6c** after co-catalyst deposition the sintered particles are covered by a thin layer of CoPi (see SI for

corresponding EDX spectra). Sintering of the particles improves ohmic contact within the film and is therefore beneficial for the overall electric conductivity and photoelectrochemical behavior, respectively. As shown in **Figure 6.6d** the photocurrent for the as-prepared F:BiVO₄ electrode is rather low (ca. 0.05 mA/cm² at 1.23 V vs. RHE) but can significantly be enhanced (x 6) by calcination of the electrode at 450 °C for 30 minutes (0.3 mA/cm² at 1.23 V vs. RHE). Increasing the calcination temperature to 550 °C further improved the PEC performance, leading to a further increase (x 2) of the photocurrents at 1.23 V vs RHE (0.6 mA/cm²). Additional deposition of a layer of CoPi on the respective photoanodes improves in both cases (450 °C and 550 °C) the PEC performance by improving the water oxidation kinetics, reaching photocurrents as high as 0.64 mA/cm² and 1.23 mA/cm² at 1.23 V vs. RHE for the 450 °C and 550 °C treated electrodes respectively.

The effect of fluorine doping on the performance of BiVO₄ concerning photoelectrochemical water oxidation was investigated by comparing the performance of F:BiVO₄ with pristine BiVO₄ photoanodes prepared under the same conditions and with comparable amounts of deposited powder (3.5 mg per electrode).

Figure 6.7a and b display the j-V-curves of both BiVO₄ and F:BiVO₄ electrodes calcined at 450 °C and 550 °C prior and after CoPi deposition. In all cases, a significant increase in photocurrent is observed for the F-containing electrodes; effect which most probably relates to the improved light-absorption of the system (see UV-Vis data, vide supra). Note: In all cases the water oxidation photocurrents are low compared to the highest reported photocurrent values for BiVO₄ photoanodes (about 4 mA/cm² at 1.23 V vs RHE)[32-34] but are fully in line with photocurrents achieved for EPD-processed BiVO₄-electrodes (about 0.6 mA/cm²).[35,36]

In order to understand the improvement of the photoelectrochemical performance, photocurrent transient measurements (**Figure 6.7c and d**) were carried out for both materials and both calcination temperatures. When the light was switched on, the pristine BiVO₄ electrode (450 °C) showed a photocurrent overshoot followed by a fast decrease of the photocurrent. In contrast, the photocurrent decay observed for F:BiVO₄ was far less pronounced; indication for a decreased recombination rate within the F-modified system. The main limiting factor for BiVO₄ as anode material for water splitting was elucidated in previous reports to be its poor bulk electronic

conductivity.[37] Despite possible negative effects on charge carrier mobility and diffusion length, doping allows in general increasing the charge carrier density and therefore allows enhancement of the overall photoresponse. Consistently, F-containing BiVO₄ showed a by far less pronounced decrease of photocurrent after the light was switched on (i.e. a slower recombination of light-induced charge carrier) leading to a better photoresponse and higher photocurrents of the F-modified system.

To further clarify the origin of improved photoelectrochemical performance of F:BiVO₄ Mott-Schottky-type potentiostatic electrochemical impedance spectroscopy measurements for both materials were performed. This method relies on measuring the capacitance of the space charge region C_{SC} at the semiconductor electrolyte interface. According to the Mott-Schottky equation the flat band potential E_{FB} and the carrier concentration N can be calculated by the linear region of the plot of $1/C_{SC}^2$ versus applied potential E as indicated in the following equation:

$$\frac{1}{C_{SC}^2} = \frac{2}{\epsilon_0 \epsilon_r A^2 e N} \left(E - E_{FB} - \frac{k_b T}{e} \right).$$

ϵ_r thereby stands for the relative permittivity of the semiconductor, ϵ_0 the permittivity in vacuum, A the surface area of the electrode, e the charge of an electron, k_b the Boltzmann constant and T the temperature.

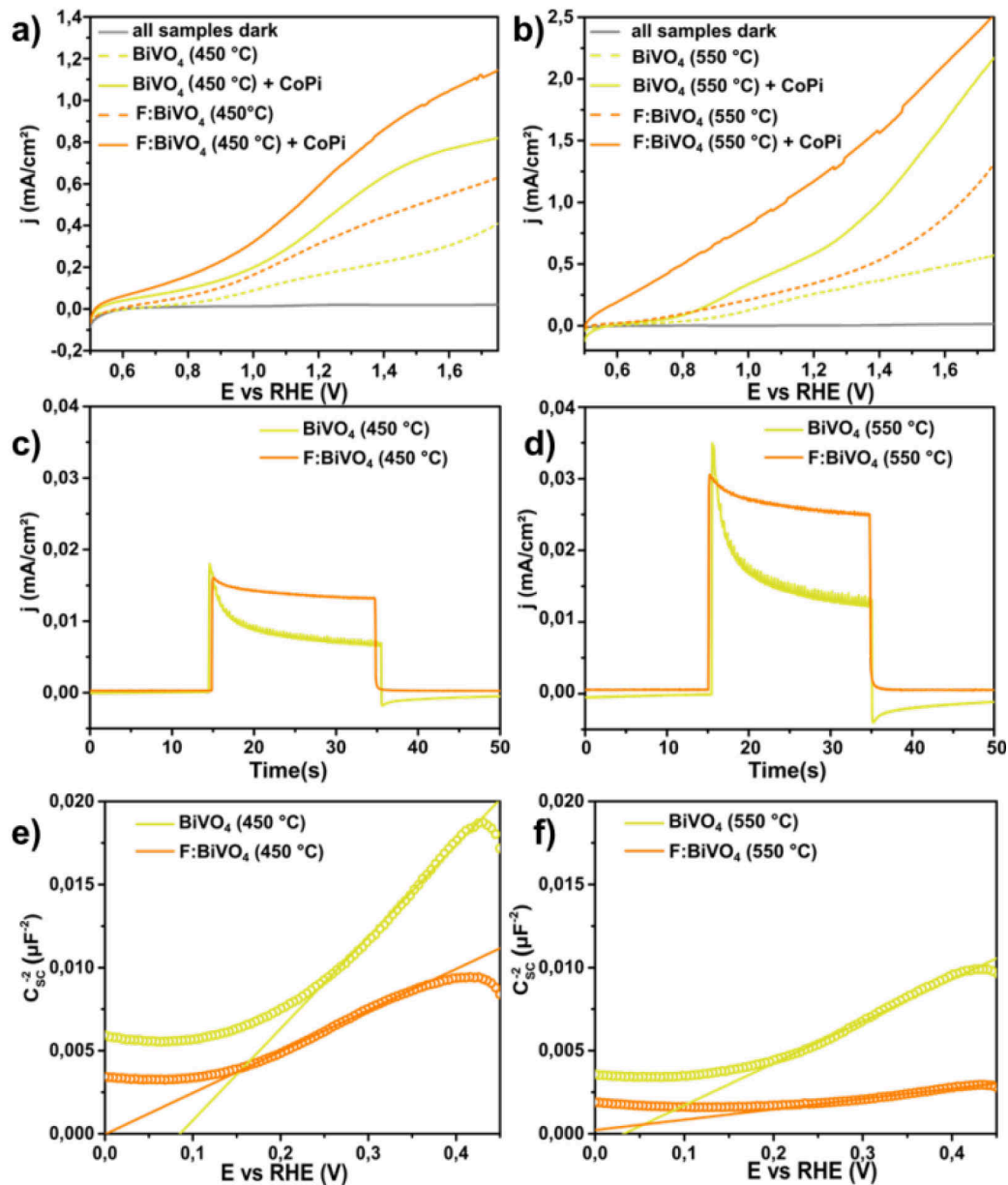


Figure 6.7: Electrochemical investigations of BiVO₄ and F:BiVO₄ electrodes calcined at 450 °C and 550 °C: a and b) j-V-curves, c and d) phototransient measurements, light on/off at $E = 1.23$ V and e and f) Mott-Schottky-Plots of BiVO₄ and F:BiVO₄ at 1 kHz.

Due to the particulate morphology of the electrodes, it was uncertain whether Mott-Schottky analysis would provide convincing results. However as illustrated in **Figure 6.7e and f** the obtained values for E_{FB} are in line with previously published E_{FB} values for BiVO₄.^[7,12,34,38] For the pristine BiVO₄ flatband potentials of 0.06 V vs. RHE for the 450 °C sample and of 0.03 V vs. RHE for the 550 °C sample were obtained. The E_{FB} of F:BiVO₄ was determined to be slightly more negative at -0.03 V vs. RHE for electrodes calcined at 450 °C and at -0.06 V for the 550 °C sample. Our results show a negative shift of the flat band potential of about 0.1 V for F:BiVO₄ for both calcination temperatures. Furthermore, a comparison of the slopes of the linear ranges of the Mott-

Schottky plots reveals a much smaller slope for F:BiVO₄ and hence - taken the surface area of the electrode as constant into account, as a result of comparable particle sizes, identical amount of deposited powder and same electrolyte exposed electrode area of 0.5 cm² (see SI) - a higher carrier concentration. As such, these findings are in good agreement with our results on the light-induced water oxidation properties of pristine and F-containing BiVO₄.

6.5. Conclusion

In here a simple route to phase pure fluorine modified BiVO₄ is reported (F:BiVO₄). Incorporation of fluorine into BiVO₄ results in the formation of cation vacancies leading to the formation of Bi_{0.94}V_{0.94}O_{3.54}F_{0.46}. Investigations of the photoelectrochemical behavior show that F-incorporation significantly improves the performance of BiVO₄ photoanodes for PEC water oxidation. Mott-Schottky analysis and photocurrent transient measurements further indicate a favorable displacement of the flat-band potential and an increase of charge carrier density as well as a substantial suppression of charge-carrier recombination in the fluorine modified system, respectively: improvements, which results in higher PEC performance. As such, fluorine incorporation into BiVO₄ turns out to be an effective way to optimize its performance for PEC water oxidation and might be in general a promising strategy to further tune the photo(electro-)catalytic activity of other oxide based photoactive materials.

Acknowledgments

The authors would like to thank S. Kühn (TU Berlin) for performing UV/Vis measurements and A. Müller-Klauke (TU Berlin) for performing ICP-OES investigations. The authors would like to thank the ZELMI (TU Berlin) and in particular Ulrich Gernert for access to and support with SEM measurements. This work is supported by the Deutsche Forschungsgemeinschaft (DFG) within the priority program SPP 1613 (LE 781/13-2, FI 1885/1-2) as well as by the DFG cluster of Excellence UniCat.

References

- [1] A. Kudo, K. Ueda, H. Kato, I. Mikami, *Catal. Lett.* **1998**, *53*, 229.
- [2] M. Gotić, S. Musić, M. Ivanda, M. Šoufek, S. Popović, *J. Mol. Struct.* **2005**, *744-747*, 535.
- [3] M. C. Neves, M. Lehocky, R. Soares, L. Lapcik, T. Trindade, *Dyes Pigm.* **2003**, *59*, 181.
- [4] M. J. Nalbandian, M. Zhang, J. Sanchez, Y.-H. Choa, D. M. Cwiertny, N. V. Myung, *J. Mol. Catal. A: Chem.* **2015**, *404-405*, 18.
- [5] M. Zhou, J. Bao, W. Bi, Y. Zeng, R. Zhu, M. Tao, Y. Xie, *ChemSusChem* **2012**, *5*, 1420.
- [6] H. Jiang, H. Dai, J. Deng, Y. Liu, L. Zhang, K. Ji, *Solid State Sci.* **2013**, *17*, 21.
- [7] C. Karunakaran, S. Kalaivani, *Mater. Sci. Semicond. Process.* **2014**, *27*, 352.
- [8] Y. Park, K. J. McDonald, K.-S. Choi, *Chem. Soc. Rev.* **2013**, *42*, 2321.
- [9] M. G. Walter, E. L. Warren, J. R. McKone, S. W. Boettcher, Q. Mi, E. A. Santori, N. S. Lewis, *Chem. Rev.* **2010**, *110*, 6446.
- [10] S. Tokunaga, H. Kato, A. Kudo, *Chem. Mater.* **2001**, *13*, 4624.
- [11] S. K. Pilli, T. E. Furtak, L. D. Brown, T. G. Deutsch, J. A. Turner, A. M. Herring, *Energy Environ. Sci.* **2011**, *4*, 5028.
- [12] W. Yao, H. Iwai, J. Ye, *Dalton Trans.* **2008**.
- [13] F. F. Abdi, N. Firet, R. van de Krol, *ChemCatChem* **2013**, *5*, 490.
- [14] H. W. Jeong, T. H. Jeon, J. S. Jang, W. Choi, H. Park, *J. Phys. Chem. C* **2013**, *117*, 9104.
- [15] K. P. S. Parmar, H. J. Kang, A. Bist, P. Dua, J. S. Jang, J. S. Lee, *ChemSusChem* **2012**, *5*, 1926.
- [16] H. S. Park, K. E. Kweon, H. Ye, E. Paek, G. S. Hwang, A. J. Bard, *J. Phys. Chem. C* **2011**, *115*, 17870.
- [17] S. P. Berglund, A. J. E. Rettie, S. Hoang, C. B. Mullins, *Phys. Chem. Chem. Phys.* **2012**, *14*, 7065.
- [18] J.-Q. Li, Z.-Y. Guo, H. Liu, J. Du, Z.-F. Zhu, *J. Alloys Comp.* **2013**, *581*, 40.
- [19] P. R. Slater, *J. Fluor. Chem.* **2002**, *117*, 43.
- [20] J. Rodriguez-Carvajal, *Physica B* **1993**, *55*, 192.
- [21] Y. Izumi, T. Itoi, S. Peng, K. Oka, Y. Shibata, *J. Phys. Chem. C* **2009**, *113*, 6706.
- [22] J. Tauc, *Mat. Res. Bull.* **1968**, *3*, 37.
- [23] M. W. Stoltzfus, P. M. Woodward, R. Seshadri, J.-H. Klepeis, B. Bursten, *Inorg. Chem.* **2007**, *46*, 3839.
- [24] A. Walsh, Y. Yan, M. N. Huda, M. M. Al-Jassim, S.-H. Wei, *Chem. Mater.* **2009**, *21*, 547.
- [25] R. Abe, M. Higashi, K. Domen, *Journal of the American Chemical Society* **2010**, *132*, 11828.
- [26] Y. Ma, F. Le Formal, A. Kafizas, S. R. Pendlebury, J. R. Durrant, *J. Mater. Chem. A* **2015**, *3*, 20649.
- [27] Z. Chen, H. N. Dinh, E. Miller, *Photoelectrochemical Water Splitting*, Springer New York, New York, NY **2013**.
- [28] A. W. Sleight, H.-y. Chen, A. Ferretti, D. E. Cox, *Mat. Res. Bull.* **1979**, *14*, 1571.
- [29] A. Fuertes, *Inorganic chemistry* **2006**, *45*, 9640.
- [30] F. A. Kröger, H. J. Vink, in *Sammelwerk kröger-vink*, Vol. 3, Elsevier **1956**, p. 307.
- [31] K. Lai, Y. Zhu, J. Lu, Y. Dai, B. Huang, *Solid State Sci.* **2013**, *24*, 79.
- [32] F. F. Abdi, L. Han, A. H. M. Smets, M. Zeman, B. Dam, R. van de Krol, *Nat. Commun.* **2013**, *4*, 2195.

- [33] M. Zhong, T. Hisatomi, Y. Kuang, J. Zhao, M. Liu, A. Iwase, Q. Jia, H. Nishiyama, T. Minegishi, M. Nakabayashi, N. Shibata, R. Niishiro, C. Katayama, H. Shibano, M. Katayama, A. Kudo, T. Yamada, K. Domen, *J. Am. Chem. Soc.* **2015**, *137*, 5053.
- [34] T. W. Kim, K.-S. Choi, *Science (New York, N.Y.)* **2014**, *343*, 990.
- [35] W. J. Jo, J.-W. Jang, K.-j. Kong, H. J. Kang, J. Y. Kim, H. Jun, K. P. S. Parmar, J. S. Lee, *Angew. Chem. Int. Ed. Engl.* **2012**, *51*, 3147.
- [36] D. Wang, R. Li, J. Zhu, J. Shi, J. Han, X. Zong, C. Li, *J. Phys. Chem. C* **2012**, *116*, 5082.
- [37] F. F. Abdi, T. J. Savenije, M. M. May, B. Dam, R. van de Krol, *J. Phys. Chem. Lett.* **2013**, *4*, 2752.
- [38] A. J. E. Rettie, H. C. Lee, L. G. Marshall, J.-F. Lin, C. Capan, J. Lindemuth, J. S. McCloy, J. Zhou, A. J. Bard, C. B. Mullins, *J. Am. Chem. Soc.* **2013**, *135*, 11389.

7. Conclusion and Outlook

7.1. Conclusion

The main objective of this study was to show the feasibility of performing targeted changes in the anion lattice without changing the crystal structure. On the one hand, special emphasis has been examined for the oxygen nitrogen substitution, followed by co-substitution (Papers 1 and 2). A further important point was the oxygen fluorine substitution in the photocatalyst bismuth vanadate, which is known from the literature (Paper 3).

In order to investigate both aspects of the project precisely, first of all, the development of pure phase materials were the key issue. In the preparation of all the compounds presented, the anion substitution by solid-vapor reaction was the medium of choice in order to convert the precursor oxides to the corresponding oxide nitrides and oxide fluorides.

For the accurate determination of the crystal structure, the products were characterized by X-ray powder diffraction and refined according to the Rietveld method. The exact composition of the compounds was determined by hot gas extraction and X-ray fluorescence analysis. The optical band gaps of the compounds were determined on the basis of UV/Vis reflection spectra. Information on the band gap energies of the synthesized compounds was obtained via the Tauc deposition method or the DASF method. Finally, the oxygen/hydrogen evolution reaction was used to check the photocatalytic activity.

In the following, the essential results on the investigated compounds are summarized. For this, as well as in the work, it is divided to tetragonal tungsten bronze structures and bismuth vanadate.

7.1.1. $\text{Ba}_{3-x}\text{La}_x\text{Ta}_5\text{O}_{14-x}\text{N}_{1+x}$

This work shows the successful syntheses of light yellow – yellow powders with the general composition $\text{Ba}_{3-x}\text{La}_x\text{Ta}_5\text{O}_{14-x}\text{N}_{1+x}$ ($x=0; 1$) which crystallize isostructurally to the literature-known mixed-valence oxide $\text{Ba}_3\text{Ta}_4^{\text{V}}\text{Ta}^{\text{IV}}\text{O}_{15}$. Quantum-chemical calculations at hybrid DFT level were made and exhibited band gaps close to the measured value. The effect of N/O distribution on the optical properties was calculated to be very pronounced. Comparing $\text{Ba}_3\text{Ta}_5\text{O}_{14}\text{N}$ to $\text{LaBa}_2\text{Ta}_5\text{O}_{13}\text{N}_2$, it was shown that the increase in the nitrogen content not only leads to a decrease of the optical band gap but also to significantly higher H_2 evolution rate.

7.1.2. F:BiVO₄

In this work also a simple, new, and promising route to phase-pure fluorine-modified BiVO₄ is reported and discussed (F:BiVO₄). The exact chemical composition was determined by combining ICP-OES, Rietveld refinements, and the investigation of the defect structure, leading to the presence of cation vacancies. Fluorine incorporation not only reduced the optical band gap (according to the DASF method) but also the performance of bismuth vanadate photoanodes for PEC water oxidation is significantly enhanced. Photocurrent transient measurements and Mott-Schottky analysis further demonstrated a favorable displacement of the flat-band potential and an increase of charge carrier density as well as a substantial suppression of charge-carrier recombination in the fluorine modified system, respectively: improvements, which result in higher PEC performances.

7.2. Outlook

In the light of these results, there are two main points that should be considered in the near future. On the one hand further attempts in decreasing the optical band gap by additional co-substitution ($\text{LaBa}_2\text{Ta}_5\text{O}_{13}\text{N}_2 \rightarrow \text{La}_2\text{BaTa}_5\text{O}_{12}\text{N}_3 \rightarrow \text{La}_3\text{Ta}_5\text{O}_{11}\text{N}_4$) seem to be worth the efforts even if the challenge of preparing a phase-pure material increases with increasing nitrogen content.

On the other hand, fluorine incorporation into BiVO_4 turns out to be an effective way to optimize its performance for PEC water oxidation and might be in general a promising strategy to further tune the photo(electro-)catalytic activity of other oxide-based photoactive materials, for example, cation-doped BiVO_4 systems (e.g. molybdenum) or even oxide nitrides such as TaON.

Despite these new findings, which have been systematically gained in this thesis, the goal of a rational design of materials remains a major challenge. Exploratory research is therefore of indispensable need in terms of the complex relationships in the system of photocatalytic water splitting. This will strengthen future efforts in the field of preparative solid state chemistry and will lead to a continuous further development of synthetic and characterization methods. In addition, the close interdisciplinary cooperation between solid state chemistry, surface chemistry, and catalysis, as has already been demonstrated in the present study, will increasingly improve the achievement of important advances in the field of photocatalytic water splitting.

Appendices

A Additional information, Supplementary material

A.1. Abbreviations

DASF	derivation of absorption spectrum fitting
DFT	density functional theory
EDX	energy dispersive X-ray analysis
EG	ethylene glycol
FWHM	full width at half maximum
HAADF	high angle annular dark field
ICP-OES	inductively coupled plasma optical emission spectrometry
PEC	photoelectrochemical
PVDF	polyvinylidene fluoride
SEM	scanning electron microscope
TEM	transmission electron microscopy
TTB	tetragonal tungsten bronze
XRD	X-ray diffraction
XRF	X-ray fluorescence spectrometry

A.2. Chemicals

Sum Formula	Purity	Producer
LaCl ₃	99.9 %	Sigma Aldrich
C ₆ H ₈ O ₇ (citric acid)	99.5 %	Sigma Aldrich
TaCl ₅	99.9999 %	Sigma Aldrich
BaCl ₂	99.9 %	Sigma Aldrich
Bi ₂ O ₃	99.9 %	Sigma Aldrich
NaVO ₃	98 %	AlfaAesar
C ₂ H ₅ OH (ethanol)	99.99 %	AlfaAesar
C ₂ H ₆ O ₂ (EG)	99 %	AlfaAesar
NH ₃	99.98 %	Air Liquide
O ₂	99.998 %	Air Liquide
-(C ₂ H ₂ F ₂) _n - (PVDF)	99 %	Apollo Scientific

B List of publications

1. B. Anke, M. Rohloff, M.G. Willinger, W. Hetaba, A. Fischer, M. Lerch; “Improved photoelectrochemical performance of bismuth vanadate by partial O/F-substitution”, *Solid State Sci.* **2017**, 63, 1–8.
2. B. Anke, T. Bredow, M. Pilarski, M. Wark, M. Lerch; “From $\text{Ba}_3\text{Ta}_5\text{O}_{14}\text{N}$ to $\text{LaBa}_2\text{Ta}_5\text{O}_{13}\text{N}_2$: Decreasing the optical band gap of a photocatalyst”, *J. Solid State Chem.* **2017**, 246, 75–80.
3. B. Anke, T. Bredow, J. Soldat, M. Wark, M. Lerch; “Synthesis, crystal structure, and photocatalytical properties of $\text{Ba}_3\text{Ta}_5\text{O}_{14}\text{N}$ ”, *J. Solid State Chem.* **2016**, 233, 282–288.
4. B. Anke, T. Bredow, M. Lerch; “Gezielte Beeinflussung der optischen Bandlücke von $\text{Ba}_3\text{Ta}_5\text{O}_{15}$ ”, *Z. Anorg. Allg. Chem.* **2016**, 642, 1033.
5. B. Anke, M. Rohloff, A. Fischer, M. Lerch; “Verbesserung der photokatalytischen Eigenschaften von BiVO_4 durch partielle O/F-Substitution”, *Z. Anorg. Allg. Chem.* **2016**, 642, 1033.
6. B. Anke, M. Rohloff, A. Fischer, M. Lerch; “Decreasing the Optical Band Gap in Photocatalysts: From $\text{Ba}_3\text{Ta}_5\text{O}_{14}\text{N}$ to $\text{LaBa}_2\text{Ta}_5\text{O}_{13}\text{N}_2$ ”, *24th Annual Conf. of the Ger. Cryst. Soc.* **2016**, materials: synthesis and structure P020.
7. B. Anke, S. Hund, C. Lorent, O. Janka, T. Block, R. Pöttgen, M. Lerch; “Synthesis, Crystal Structure, and Magnetic Properties of Pyrochlore-Type $\text{Eu}_2\text{Ta}_2(\text{O,N})_{7+\delta}$ ”, *Z. Anorg. Allg. Chem.* **2017**, DOI: 10.1002/zaac.201700024.
8. M. Rohloff, B. Anke, S. Zhang, U. Gernert, C. Scheu, A. Thomas, M. Lerch, A. Fischer; “Mo-doped BiVO_4 Thin Films – High Photocatalytic Activity Achieved by Tailored Structure and Morphology”, **in preparation**.
9. M. Rohloff, B. Anke, M. Lerch, A. Fischer; “Enhancement of photoelectrochemical performance by anion substitution in $\text{Mo}:\text{BiVO}_4$ thin film electrodes”, **in preparation**.

-
10. A. Ulpe, B. Anke, S. Berendts, M. Lerch, T. Bredow; “F-doping of BiVO₄: defect structures, phase stability and electronic properties from first principles”, **in preparation.**

C List of conference contributions

- 09/2016 19. Vortragstagung Fachgruppe Festkörperchemie und Materialforschung, Innsbruck, Austria – 2 *Posters*
- 09/2016 DFG SPP1613 Solar H₂ Project Meeting, Berlin, Germany – *Poster* and *Lecture*
- 03/2016 24th Annual Meeting of the German Crystallographic Society (DGK), Stuttgart, Germany – *Poster*
- 03/2015 International Conference SolarFuel15 (DFG SPP1613), Mallorca, Spain – *Poster*
- 10/2014 Bunsen Colloquium 2014: Lithium in Solids: Structure and Dynamics, Hannover, Germany – *Poster*
- 09/2014 18. Vortragstagung Fachgruppe Festkörperchemie und Materialforschung, Dresden, Germany

D Awards

- 1. Posterpreis auf 19. Vortragstagung der Fachgruppe Festkörperchemie und Materialforschung
Verleihung: 20. September 2016, Disziplin: Festkörperchemie und Materialforschung, Stifter: Gesellschaft Deutscher Chemiker e. V. (GDCh)

List of Tables

Table 2.1: Localization of various ions in the different crystallographic sites. ^[24]	6
Table 3.1: Synthesis conditions for the new compounds $\text{Ba}_3\text{Ta}_5\text{O}_{14}\text{N}$ and $\text{LaBa}_2\text{Ta}_5\text{O}_{13}\text{N}_2$	17
Table 4.1: Refined structural parameters of $\text{Ba}_3\text{Ta}_5\text{O}_{14}\text{N}$ in comparison to $\text{Ba}_3\text{Ta}_5\text{O}_{15}$	38
Table 4.2: Atomic positional parameters and isotropic Debye-Waller factors for $\text{Ba}_3\text{Ta}_5\text{O}_{14}\text{N}$	39
Table 4.3: Determined Ba/Ta-O/N bond lengths in $\text{Ba}_3\text{Ta}_5\text{O}_{14}\text{N}$ and $\text{Ba}_3\text{Ta}_5\text{O}_{15}$	42
Table 4.4: Relative stability (eV) of different O/N configurations of $\text{Ba}_3\text{Ta}_5\text{O}_{14}\text{N}$; two nitrogen atoms are placed at particular lattice sites, and all other sites are occupied by oxygen. Comparison of two hybrid DFT functionals and basis sets, see text.	44
Table 4.5: Optimized nearest-neighbor distances around the N atoms (Å) obtained for five configurations. Results obtained with PW1PW/std.	44
Table 4.6: Calculated electronic band gaps of the considered O/N configurations (eV). Comparison of PW1PW/std and HSE06/tzvp.	45
Table 5.1: Refined structural parameters of $\text{LaBa}_2\text{Ta}_5\text{O}_{13}\text{N}_2$ in comparison to $\text{Ba}_3\text{Ta}_5\text{O}_{14}\text{N}$ and $\text{Ba}_3\text{Ta}_5\text{O}_{15}$	59
Table 5.2: Refined atomic parameters for $\text{LaBa}_2\text{Ta}_5\text{O}_{13}\text{N}_2$	59
Table 5.3: Calculated atomic parameters of the $\text{LaBa}_2\text{Ta}_5\text{O}_{13}\text{N}_2$ phase and deviations from measured values in parentheses (c.f. Table 2). CRYSTAL-HSE06 results.	62
Table 5.4: Calculated fundamental direct (d) and indirect (id) band gaps (eV) for $\text{Ba}_3\text{Ta}_5\text{O}_{15}$, $\text{Ba}_3\text{Ta}_5\text{O}_{14}\text{N}$, and $\text{LaBa}_2\text{Ta}_5\text{O}_{13}\text{N}_2$. Only the results for the most stable La/Ba and O/N distributions are shown. CRYSTAL-HSE06 results.	62
Table 6.1: Refined structural parameters of BiVO_4 in comparison to F: BiVO_4	77
Table 6.2: Structural parameters for BiVO_4 and F: BiVO_4	78

List of Figures

Figure 1.1: For the first time, the atmospheric CO ₂ concentration at Mauna Loa stayed above the symbolic milestone of 400 ppm for the full year in 2016, including September's seasonal low. Source: UC San Diego (https://scripps.ucsd.edu/programs/keelingcurve/).	1
Figure 2.1: Band edge alignment of undoped and N-doped KTaO ₃	5
Figure 2.2: Schematic projection of the TTB crystalline network (A ₂ BC ₂ M ₅ X ₁₅) along the c axis (A, B, and C correspond to cationic sites with 15, 12, and 9 coordination numbers, respectively).	7
Figure 2.3: V-O ₄ tetrahedra and Bi-O ₈ polyhedra in monoclinic scheelite BiVO ₄ with the determined bond lengths (Å).	8
Figure 2.4: Phase transition in BiVO ₄	9
Figure 2.5: Temperature dependence of a normalized order parameter for BiVO ₄	10
Figure 2.6: Schematic band structures of tetragonal zircon-type BiVO ₄ and monoclinic scheelite BiVO ₄ proposed by Kudo <i>et al.</i> ^[39]	11
Figure 3.1: Flow chart for preparing amorphous powder precursors by the Pechini method.	
Figure 3.2: left: gas flow controller for NH ₃ , O ₂ and N ₂ ; mid: tube furnace from Gero Typ SR-A 60-300/12; right: reaction space under the rapid gas supply.	
Figure 3.3: Sketch of fluorination apparatus. The inner corundum boat contains the sample to be fluorinated and the outer boat is filled with PVDF.	20
Figure 4.1: X-ray powder diffraction pattern of Ba ₃ Ta ₅ O ₁₄ N with the results of the Rietveld refinement.	38
Figure 4.2: Unit cell of Ba ₃ Ta ₅ O ₁₄ N and polyhedral representation of the crystal structure. Ta(O/N) ₆ octahedra are drawn in green; Ba atoms are represented by black balls.	40
Figure 4.3: Ba-O/N polyhedra in Ba ₃ Ta ₅ O ₁₄ N with the determined bond lengths (Å). ..	41
Figure 4.4: Ta(O/N) ₆ octahedra in Ba ₃ Ta ₅ O ₁₄ N with the determined bond lengths(Å). ..	42
Figure 4.5: Tauc plot of Ba ₃ Ta ₅ O ₁₄ N based on diffuse reflectance geometry.	43
Figure 4.6: Projected density of states for configurations (1), left, and (2), right. For clarity the zero point of energy was shifted to the bottom of the conduction band. (VBM: valence band maximum).	
Figure 4.7: Photocatalytic hydrogen evolution rates of Ba ₃ Ta ₅ O ₁₄ N before and after reductive <i>in situ</i> photodeposition of 0.0125 wt.-% Rh.	48
Figure 5.1: X-ray powder diffraction pattern of LaBa ₂ Ta ₅ O ₁₃ N ₂ with the results of the Rietveld refinement.	58
Figure 5.2: Unit cell of LaBa ₂ Ta ₅ O ₁₃ N ₂ with the connectivity of Ta(O/N) ₆ polyhedra. ..	59
Figure 5.3: Plot of $d\{\ln(A/\lambda)\}/d(1/\lambda)$ versus $(1/\lambda)$ for Ba ₃ Ta ₅ O ₁₄ N (black) and LaBa ₂ Ta ₅ O ₁₃ N ₂ (red).	61

- Figure 5.4: Atom-projected density of states for $\text{Ba}_3\text{Ta}_5\text{O}_{15}$ (left), $\text{Ba}_3\text{Ta}_5\text{O}_{14}\text{N}$ (center), and $\text{LaBa}_2\text{Ta}_5\text{O}_{13}\text{N}_2$ (right) as obtained with CRYSTAL-HSE06. The binding energy is given relative to the valence band maximum (VBM). 63
- Figure 5.5: Photocatalytic H_2 evolution rates of $\text{Ba}_3\text{Ta}_5\text{O}_{14}\text{N}$ and $\text{LaBa}_2\text{Ta}_5\text{O}_{13}\text{N}_2$ before and after *in-situ* photodeposition of 0.0125 wt% of Rh in $\text{H}_2\text{O}/\text{CH}_3\text{OH}$ solution under Hg-lamp irradiation. 65
- Figure 6.1: Sketch of fluorination apparatus. The inner corundum boat contains the sample to be fluorinated and the outer boat is filled with PVDF. 72
- Figure 6.2: Bright field TEM image of F:BiVO₄ (left) and high resolution TEM image of one of the particles (right). The inlay shows the corresponding FFT. Spots due to the (020) and (20-1) lattice planes or the [102] oriented particle are labelled. . 75
- Figure 6.3: High angle annular dark field image of F:BiVO₄ (left). EDX maps of F(yellow), Bi (green) and V(red) (right from top to bottom). 76
- Figure 6.4: X-ray powder diffraction patterns of BiVO₄ (left) and F:BiVO₄ (right) with the results of the Rietveld refinements. Inset: Unit cell of F:BiVO₄ and polyhedral representation of the crystal structure. Bi(O,F)₈ polyhedra are drawn in yellow, V(O,F)₄ tetrahedra are shown in blue. 77
- Figure 6.5: Tauc plot for BiVO₄ and F:BiVO₄ based on diffuse reflectance spectrometry. 80
- Figure 6.6: Illustration of electrode fabrication process: SEM top-view and cross-sectional images of a) as-prepared electrodes, b) calcined electrodes (450 °C under air), c) calcined electrodes with deposited CoPi co-catalyst layer, d) Picture of an F:BiVO₄ electrode and j-V-curves: as-prepared F:BiVO₄, calcined F:BiVO₄ and F:BiVO₄ with a deposited CoPi layer (0.1 M KPi buffer, pH 7.3, 20 mV/s). 81
- Figure 6.7: Electrochemical investigations of BiVO₄ and F:BiVO₄ electrodes calcined at 450 °C and 550 °C: a and b) j-V-curves, c and d) phototransient measurements, light on/off at E = 1.23 V and e and f) Mott-Schottky-Plots of BiVO₄ and F:BiVO₄ at 1 kHz. 84